HIGH-TEMPERATURE CORROSION OF ALUMINUM ALLOYS: OXIDE-ALLOY INTERACTIONS AND SULFUR INTERFACE CHEMISTRY

Swarnagowri Addepalli, B.S., M.S.

Dissertation Prepared for the Degree of

DOCTOR OF PHILOSOPHY

UNIVERSITY OF NORTH TEXAS

December 2000

TO BE APPROVED:

Jeffry A. Kelber, Major Professor
William E. Acree, Jr., Committee Member
Oliver M. R. Chyan, Committee Member
Michael G. Richmond, Committee Member
David E. Golden, Committee Member
Ruthanne D. Thomas, Chair of the Department of Chemistry
C. Neal Tate, Dean of the Robert B. Toulouse School of Graduate Studies

Addepalli, Swarnagowri, High-temperature corrosion of aluminum alloys: Oxide-alloy interactions and sulfur interface chemistry. Doctor of Philosophy (Analytical Chemistry), December 2000, 159 pp., 2 tables, 44 illustrations, reference list, 136 titles.

The spallation of aluminum, chromium, and iron oxide scales is a chronic problem that critically impacts technological applications like aerospace, power plant operation, catalysis, petrochemical industry, and the fabrication of composite materials. The presence of interfacial impurities, mainly sulfur, has been reported to accelerate spallation, thereby promoting the high-temperature corrosion of metals and alloys. The precise mechanism for sulfur-induced destruction of oxides, however, is ambiguous. The objective of the present research is to elucidate the microscopic mechanism for the high-temperature corrosion of aluminum alloys in the presence of sulfur. Auger electron spectroscopy (AES), low energy electron diffraction (LEED), and scanning tunneling microscopy (STM) studies were conducted under ultrahigh vacuum (UHV) conditions on oxidized sulfur-free and sulfur-modified Al/Fe and $Ni_3Al(111)$.

Evaporative deposition of aluminum onto a sulfur-covered iron surface results in the insertion of aluminum between the sulfur adlayer and the substrate, producing an Fe-Al-S interface. Aluminum oxidation at 300 K is retarded in the presence of sulfur. Oxide destabilization, and the formation of metallic aluminum are observed at temperatures > 600 K when sulfur is located at the Al_2O_3-Fe interface, while the sulfur-free interface is stable up to 900 K. In contrast, the thermal stability (up to at least 1100 K) of the Al_2O_3 formed on an $Ni_3Al(111)$ surface is unaffected by sulfur. Sulfur remains at the oxide-$Ni_3Al(111)$ interface after oxidation at 300 K. During annealing, aluminum segregation

to the γ-Al_2O_3-$Ni_3Al(111)$ interface occurs, coincident with the removal of sulfur from the interfacial region. A comparison of the results observed for the Al_2O_3/Fe and Al_2O_3/Ni_3Al systems indicates that the high-temperature stability of Al_2O_3 films on aluminum alloys is connected with the concentration of aluminum in the alloy.

ACKNOWLEDGMENTS

The author wishes to express her gratitude to Prof. Jeff Kelber for his guidance. The author would also like to acknowledge the U. S. Department of Energy (Office of Basic Energy Sciences) for providing financial support for this research. Finally, the author would like to thank her family and friends for their constant encouragement and support.

TABLE OF CONTENTS

LIST OF TABLES

LIST OF ILLUSTRATIONS

CHAPTER 1

INTRODUCTION

Aluminum alloys are frequently used in technological applications such as electric power generation, aerospace and the petrochemical industry, due to their ability to selectively form thermodynamically stable, high-temperature corrosion-resistant aluminum oxide scales (1). The protective aluminum oxide scale is, however, destroyed in the presence of sulfur during thermal cycling (2-4). Sulfur has also been directly implicated in intergranular embrittlement (5,6) in alloys. Experimental studies have consistently demonstrated that the accumulation of sulfur at an oxide-alloy interface remarkably hastens the high-temperature corrosion of the material (3,7,8). Conversely, desulfurization using pretreatments such as polishing (9), or annealing in a hydrogen ambient (3,4) improves oxide adherence to the substrate. The detrimental effects of sulfur on oxide stability have also been reported in the case of chromium oxide- (10) and iron oxide- (11-14) forming systems. The mechanism by which sulfur induces destabilization of protective oxide scales, however, is still a matter of considerable controversy (7-9,11-18).

The goal of the present research is to gain fundamental insight into the interplay between sulfur interface chemistry and alumina-substrate interactions in the case of aluminum-containing alloys. Experiments carried out to understand the role of sulfur in the destabilization of ultrathin aluminum oxide films include:

(1) Oxidation of aluminum deposited onto clean and sulfur-contaminated iron surfaces, followed by a study of the thermal stabilities of the ultrathin aluminum oxide films formed in both cases.

(2) Investigation of the growth rate, morphology and thermal stability of the oxide prepared on a $Ni_3Al(111)$ surface, both in the presence and absence of adsorbed sulfur.

The experiments outlined above were conducted in ultrahigh vacuum (UHV), so that surfaces with controllable compositions could be routinely prepared. Surface analytical techniques such as Auger electron spectroscopy (AES), low energy electron diffraction (LEED), and scanning tunneling microscopy (STM) were used to characterize the surfaces.

This dissertation is divided into six chapters. The current chapter provides background information on the fundamental concepts of the oxidation of metals and alloys, and sulfur-induced corrosion of metals and alloys, in Sections 1.1 and 1.2 respectively. The experimental methodology, model surface materials, and the various surface analytical methods employed in this research are reviewed in Section 1.3. In Chapter 2, the interactions at the Al-Fe(111) interface in the presence of sulfur, namely, the effects of sulfur on the room-temperature oxidation of aluminum are presented. Chapter 3 is a description of the results obtained for the sulfur-induced destabilization of ultrathin aluminum oxide films prepared on an Fe(poly) substrate. Chapter 4 discusses the formation of a well-ordered γ'-Al_2O_3 film on a $Ni_3Al(111)$ surface at elevated temperatures, and the structural characterization of the γ'-Al_2O_3-$Ni_3Al(111)$ interface. The results for the formation of a sulfur adlayer on a $Ni_3Al(111)$ surface are given in

Chapter 5. The interactions at the Al_2O_3-S-Ni_3Al(111) interface at elevated temperatures are described in Chapter 6.

1.1. Fundamental Concepts of the Oxidation of Metals and Alloys

Although oxidation generally refers to the extraction of electrons from an element, it is also used to designate the chemical reaction between a metal (M) and oxygen (O_2) or water vapor (H_2O) or carbon dioxide (CO_2) in the absence of an aqueous phase (19). A freshly abraded metal surface is instantaneously covered by a thin film of its oxide that protects it from further oxidation in air. This protective 'skin' develops on the surface through a series of steps as illustrated in Fig. 1.1 (20).

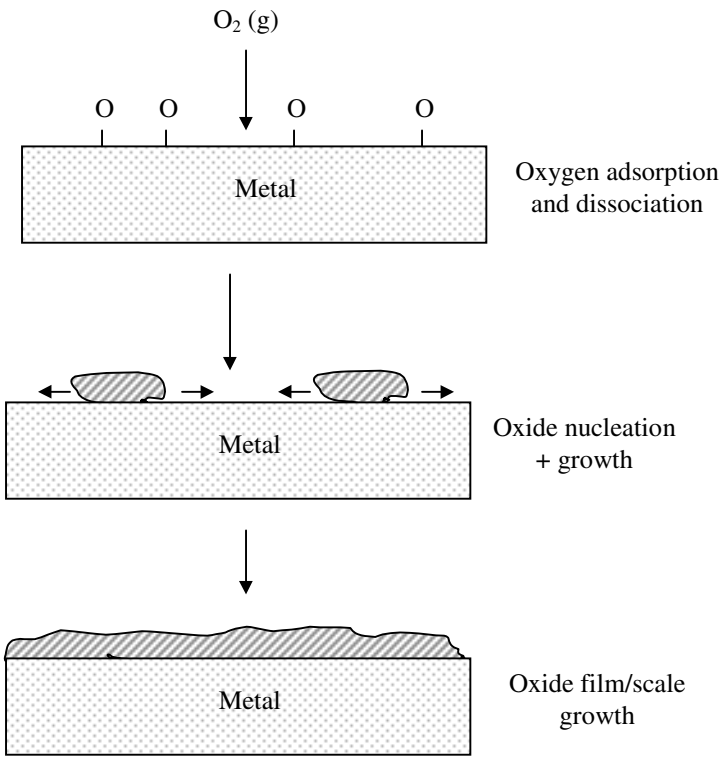

Fig. 1.1. Various steps involved in film/scale formation during metal oxidation.

Initially, the molecules of the oxidant (O_2 in Fig. 1.1) are physically adsorbed, i.e., relatively loosely bound on the bare metal surface. The energy of the physisorption process is low, typically of the order of 20-25 kJ mol^{-1} (21). The molecules then dissociate into atoms that become strongly attached to the surface by chemisorption which involves a higher energy change (~ 600 kJ mol^{-1}) (21). This is followed by a general chemical reaction to form small oxide nuclei on the surface (19):

$$x\,M + \tfrac{1}{2}(y\,O_2) \rightarrow M_xO_y \qquad (1\text{-}1)$$

The above reaction actually consists of two spatially isolated electrochemical processes (19,20):

(1) oxidation of metal atoms at the scale-metal interface:

$$M \rightarrow M^{y+} + y\,e^- \qquad (1\text{-}2a)$$

(2) oxidant reduction at the scale-gas interface by the electrons liberated in (1-2a):

$$\tfrac{1}{2}\,O_2 + 2\,e^- \rightarrow O^{2-} \qquad (1\text{-}2b)$$

The oxide nuclei thus formed continue to grow laterally until they coalesce and form a continuous oxide film M_xO_y (Fig. 1.1) that may cover the underlying metal surface, and protect, or 'passivate' the metal from further oxidation/corrosion. This passivating characteristic of the oxide prohibits further access of the reactants, i.e., O_2 and the metal surface to one another. The physical and chemical properties of this oxide film are therefore of paramount importance in deciding the rate of oxidation and the lifetime of the equipment exposed to high-temperature oxidizing environments. For example, the formation of a porous, non-protective oxide with defects such as cavities or microcracks is undesirable, since this would lead to sustained oxidation until the metal is entirely

consumed. Factors that would inhibit the growth of a protective oxide film, such as the inclusion of corrosive impurities, are also of prime interest, for the same reason.

Thermodynamically, the growth of an oxide is governed by the standard free-energy change ΔG° of the reaction (1-1), which must be negative for oxidation to proceed spontaneously as shown, with all the reactants and products in their standard states (20,21). For (1-1), the equilibrium constant K, derived from the law of mass action, is given by (20,21):

$$K = \frac{[M_x O_y]}{[M]^x [O_2]^{y/2}} \tag{1-3}$$

In Eq. (1-3), the quantities in square brackets correspond to the active masses of the reacting species and the products in the reaction (1-1). The active masses of the solid metal and the oxide are equal to unity by convention, and the active mass of O_2 is equal to its partial pressure (p_{O_2}) under equilibrium conditions. Therefore, ΔG° can be calculated from the equilibrium constant of the reaction according to (21):

$$\Delta G^\circ = -RT \ln K_p = -RT \ln \frac{1}{p_{O_2}} \tag{1-4}$$

where R is the gas constant, T is the absolute temperature, and K_p is the equilibrium constant of the reaction. For a given oxidation reaction, the free-energy change ΔG is given by Eq. (1-5):

$$\Delta G = \Delta G^\circ - RT \ln p'_{O_2} \tag{1-5}$$

where p'_{O_2} represents the initial partial pressure of O_2. According to Eq. (1-5), the spontaneity of a reaction depends upon the reaction conditions selected, namely, the

temperature and the partial pressure of O_2. Thus, by controlling these two parameters, one can, in principle, drive the reaction in the desired direction.

In corrosion studies, the thermodynamic stability of the oxide, which is related to its standard free energy of formation (ΔG_f°), is also an important parameter. The standard free energy of oxide formation is estimated from the standard enthalpy of the reaction (ΔH_f°), and the standard change in entropy (ΔS_f°) using Eq. (1-6):

$$\Delta G_f^\circ = \Delta H_f^\circ - T\,(\Delta S_f^\circ) \qquad (1\text{-}6)$$

When a *solid* metal M is combined with a *gas* (O_2) to produce a stable *solid* oxide, M_xO_y, the disorder of the system, as measured by the change in entropy, is reduced. The negative entropy change is attributable to the formation of the solid oxide (solid + gas $\rightarrow$ solid) with a more regular arrangement of oxygen atoms than that previously existing in the gaseous state. A plot of ΔG_f° versus T would therefore be linear, with a positive slope. This is true for all metal oxide systems (21). At temperatures above the melting point of the metal, the slope would increase, since the reaction (liquid metal + gaseous O_2 $\rightarrow$ solid oxide) involves a higher entropy change than at temperatures below the melting point. A compilation of the plots (ΔG_f° versus T) for the oxidation reactions of different metals in the standard state (the 'Ellingham diagram') can be used to determine the relative thermodynamic stabilities of the oxides in question (20). In the Ellingham diagram, the more negative the standard free energy of formation, the more thermodynamically stable the oxide. The standard free-energy change ΔG° for the formation of most metal oxides is negative, i.e., oxides are thermodynamically more

stable than metals in oxygen atmospheres (21). This explains why most metals are naturally found as their corresponding oxides.

Although free-energy considerations indicate the extent of feasibility of a given reaction and/or the formation of the most stable reaction product, they cannot predict the final outcome of a reaction. Since the free-energy changes for the formation of most metal oxides are negative, one would expect all of the metal to be converted into its most stable oxide when exposed to an O_2 atmosphere. In reality, however, this does not occur. Oxide growth ceases quickly after a certain thickness (< 100 nm) is reached, because the product (M_xO_y) acts as a diffusion barrier between the substrate and the surrounding environment, and restricts further access of one reactant to the other (21). Thus, oxidation involves thermodynamic as well as kinetic parameters.

Oxidation kinetics is generally described with reference to the mathematical relationship that represents the variation in oxide thickness, *d*, with time, *t*. At relatively lower temperatures (< 700 K), and for the formation of thinner oxide films (< 100 nm), these relationships are logarithmic, i.e., the rate of growth of the film or the increase in film thickness shows an inverse dependence with time, according to the equation (20-22)

$$d = K_1 \log t \qquad (1\text{-}7)$$

where K_1 is the rate constant. In oxidation processes obeying logarithmic rate laws, the initially high oxide growth rate falls off quickly after a certain limiting thickness (typically 100 nm) is attained, unless sufficient thermal energy is supplied to the system to promote further film growth by ionic diffusion through the film under the influence of a concentration gradient (21). At higher temperatures, however, parabolic growth

kinetics [Eq. (1-8)] prevails, and the films formed by oxidation at higher temperatures are considerably thicker (20,21):

$$d^2 = K_2 t \tag{1-8}$$

In the above equation, K_2 is the parabolic rate constant, which increases exponentially with increase in temperature. Oxide growth under these conditions is extremely fast, as the thickness increases as d^2 with time, and involves diffusion of ions via point defects (21).

Irrespective of its growth kinetics, thickness, thermodynamic stability, or chemical inertness, an oxide cannot protect the underlying metal substrate if it does not remain adherent under thermal cycling conditions, i.e., periodic heating and cooling. Pilling and Bedworth proposed that the ratio of the oxide volume to that of the metal could be used as a predictor for oxide protectiveness (19,20). The ideal Pilling-Bedworth ratio would be close to one. A volume ratio less than one produces insufficient oxide to cover the metal, and is therefore indicative of a non-protective scale. Similarly, a volume ratio very much greater than one induces large compressive stresses in the oxide, which would buckle the film, and destroy its adherence.

1.1.1. Corrosion Resistance of Alloys

Pure metals are ordinarily of very little practical importance, because some of their properties (poor resistance to corrosion, low melting point, poor mechanical strength) are inappropriate for technological applications. Alloying of one metal with other elements imparts the desired combination of properties such as superior corrosion resistance, higher melting point, and greater mechanical strength, and so on to the material. A typical example where alloying yields systems with better properties is the

formation of aluminum containing alloys. While aluminum metal forms a thermodynamically stable oxide scale (Al_2O_3), its melting point is too low [~ 933 K (23)] for high-temperature corrosion-resistant applications. Alloying of aluminum with various metals such as iron, nickel and titanium (the so-called 'aluminides') yields materials with melting points in excess of 1573 K (1), and also affords better high-temperature corrosion resistance to these materials (21). Other alloying elements that could be used to improve the resistance of various metals to atmospheric corrosion are silicon (24), beryllium (24), and chromium.

The development of corrosion resistance in alloys (e.g., AB) is based upon the incorporation of an element (B) that would be preferentially oxidized to form a protective external oxide scale (BO). As mentioned above, the element B could be either aluminum, silicon, beryllium, or chromium. A protective external oxide is formed if (24): [1] the oxide of the solute B is thermodynamically more stable than the lowest oxide of the base metal A, and, [2] the concentration of B is sufficiently high to promote the formation of the oxide as an external layer. The limiting mole fraction of B (N_B) above which only BO will form can be calculated using Eq. (1-9), if one assumes ideal conditions, and ignores possible nucleation effects (21):

$$\Delta G_{f,BO}^{\circ} - \Delta G_{f,AO}^{\circ} = RT \ln\left[\frac{N_B}{1-N_B}\right] \qquad (1\text{-}9)$$

where $\Delta G_{f,BO}^{\circ}$ and $\Delta G_{f,AO}^{\circ}$ are the standard free energies for the formation of the oxides BO and AO, respectively. Under conditions where only B is oxidized, the concentration of B at the oxide-alloy interface is mainly dependent upon (21): [1] the ratio of the oxidation rate constant to the alloy interdiffusion coefficient, [2] the ratio of

concentration of B in the oxide to that in the bulk alloy, and [3] the Pilling-Bedworth ratio of the oxide. With time, the alloy composition near the alloy-oxide interface will gradually change, unless B atoms diffuse from the bulk of the alloy to the interface as rapidly as they are removed into the growing oxide (21). Thus the kinetics of oxide growth, and the kinetics of diffusion of the alloying elements determine whether depletion of B occurs to ultimately lead to an A-enriched zone adjacent to the oxide-substrate interface (21). The composition of the alloy immediately beneath the oxide scale would in turn drastically affect the long-term stability of the oxide. When N_B becomes lower than the threshold value, one can expect the formation of BO as an internal oxide or a mixture of both AO and BO, instead of a protective external scale of BO.

The long-term stability of the protective oxide is also drastically affected by the presence of impurities like sulfur. The detrimental effects of sulfur on alloy performance are reviewed in Section 1.2 below.

1.2. Sulfur-Induced Corrosion of Metals and Alloys

It is well known that all oxidation-resistant alloys, even those that form alumina and chromia scales, undergo very rapid, often catastrophic degradation in the presence of sulfur (2). Sulfur can be incorporated into the metal or alloy from different sources (Fig. 1.2). Sulfur is indigenously present as an impurity in many metals and alloys (5). Sulfur could also be introduced into the alloy from the surrounding environment, if sulfur-containing species such as H_2S, or SO_2 are abundant (2). H_2S is a major gaseous contaminant in hydrogenous reducing gases such as gasified coal, hydrolyzed refuse, or

processed petroleum (19). SO_2 is present in various concentration levels up to several percent in oxidizing gases such as fossil fuel combustion products (automotive exhaust, incinerator gases, and process effluent gases) (19). In such chemically hostile atmospheres, alloys are destroyed by sulfide corrosion (2,16). Even when dense, adherent scales are preformed on the alloy surfaces before exposure to sulfidizing

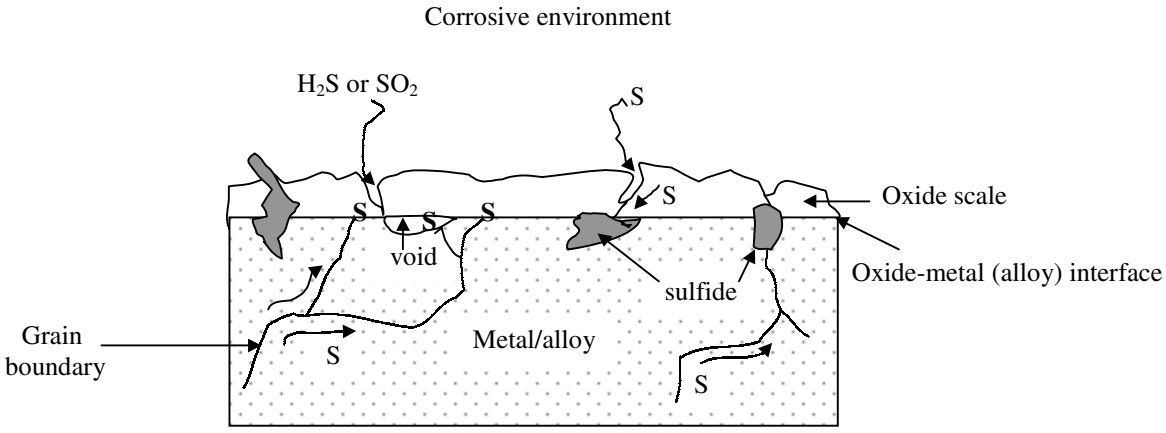

Fig. 1.2. Sources for the incorporation of sulfur at the metal(alloy)-oxide interface.

atmospheres, scale breakdown is observed, although the onset of scale breakaway is delayed (2,10). The attack by sulfur atoms or molecules is initiated at flaws or fissures or other sites of fracture in the oxide scales (Fig. 1.2) (16,19,25). These atoms then slowly penetrate the oxide scale, reaching the oxide-alloy interface where rapidly growing sulfides begin to form (2). The formation of eutectics could also lead to speedy corrosion of the materials, due to intergranular penetration by the liquid sulfide products (2).

In multicomponent atmospheres containing both sulfur-containing species and O_2, oxygen and sulfur compete for reaction with the elements present in the alloy (20).

Sulfidation rates are considerably higher than oxidation rates (2). Therefore the product formed under these circumstances is a heterogeneous mixture of sulfides and oxides. Transition metal sulfides are thermodynamically less stable, melt generally at lower temperatures, have greater defect densities, and exhibit higher deviations from stoichiometry than the corresponding oxides (2). Moreover, they are porous, and much less protective than oxides (20), allowing greater mass transport through the defects.

While it is known that sulfur accelerates the corrosion of metals and alloys, the exact mechanism for sulfur-induced destruction of oxides is still a topic of considerable debate (7-9,11-18). One reason for this is that sulfur segregation from the bulk can lead to oxide scale spallation even in sulfur-free environments. Rapid spallation of the oxide scale exposes the underlying metal surface to the surrounding atmosphere. As a consequence, more and more metal is consumed during thermal cycling, eventually leading to catastrophic corrosion. Several mechanisms have been proposed for the disintegration of oxides in the presence of sulfur. Some researchers (4,9,17) have suggested that sulfur accumulates at metal-oxide interfaces at elevated temperatures and weakens the metal-oxide bonds. These conclusions were based on the observation that removal of sulfur from the metal or alloy by annealing in H_2 (3,4), or periodic surface polishing (9) improved scale adhesion. Grabke and coworkers (15), however, investigated this hypothesis in the case of Fe-Cr and Ni-Al alloys using scanning Auger microscopy (SAM) and scanning electron microscopy (SEM), and reported that sulfur segregation occurs to voids beneath oxide scales. These authors (15) concluded that sulfur facilitates interfacial void formation by reducing the free energy of the exposed metal/alloy in the voids, and induces scale-substrate separation upon annealing by

increasing the number of voids at the oxide-alloy interface. Other researchers (8) used an *in situ* indentation method, and observed sulfur enrichment at interfacial voids as well as at intact oxide-metal interfaces, and reported that scale-substrate separation did not precede sulfur segregation. Transmission electron microscopy (TEM) and scanning transmission electron microscopy (STEM) studies of oxidized chromium samples (18) also confirmed sulfur segregation to intact oxide-metal interfaces.

In all the reports highlighted above, scale-substrate separation, or spallation was ascribed primarily to mechanical reasons such as stresses induced in the scale during growth or thermal cycling. The possibility of the existence of a chemical component to sulfur-induced scale-substrate separation was often deliberately ruled out on the basis of thermodynamic considerations (23). Experimental studies carried out on Fe/S/Fe-oxide systems (11-14) under ultrahigh vacuum conditions, however, demonstrated that dewetting of ultrathin iron oxide films is initiated by a chemical reaction between the sulfur atoms and the iron oxide. Coincident with the Fe-O bond breakage, the formation of SO_2 (11,12) was observed, contrary to thermodynamic predictions based on bulk bond dissociation enthalpies. The sulfur-induced Fe-O bond scissioning is due to the fact that Fe-S bonds at surfaces and interfaces are considerably more covalent than their bulk analogs (26). Hence, bulk bond dissociation energies are not necessarily applicable to surface and interfacial reactions. Work function measurements (27) have demonstrated that surface and interfacial Ni-S bonds are also essentially covalent, and therefore, exhibit enhanced reactivity. In the case of alumina-forming alloys, owing to the high thermodynamic stability of Al_2O_3 (28), one might not expect oxide destabilization to occur by a mechanism in which the oxide is chemically reduced by sulfur. The covalent

characteristics of metal-sulfur bonds (26,27), however, might lead to unusual interfacial chemistry even in the case of alumina-forming systems. Studies investigating sulfur interface chemistry in the case of alumina-forming metals and alloys have not been reported in the literature to date.

1.3. Experimental Methodology

The experimental strategy consisted of sulfidizing an atomically clean metal or alloy surface either by reaction with H_2S, or by thermal segregation of sulfur from the bulk. Following sulfidation, the sample was oxidized and annealed, and the AES, LEED and STM results obtained were compared with those recorded in case of the sulfur-free surface.

The clean surface of a non-noble metal is normally highly reactive towards particles impinging upon it from the gaseous phase. Since the focus of the present study is to investigate the effects of impurities such as sulfur on the thermal stability of oxides formed on aluminum-containing alloys, it is desirable to begin an experiment with a sample with a definite surface composition, then alter its composition in a controlled manner by deliberately introducing monolayer and submonolayer concentrations of adsorbates, and examine surface reactivity as a function of adsorbate coverage. By definition, the surface concentration of atoms is of the order of 10^{15} cm^{-2} (29). At an ambient gas pressure of 10^{-6} Torr, the number of molecules required for the build-up of a monolayer is offered to a surface in one second, if one assumes that every molecule that strikes the surface becomes adsorbed [i.e., sticking coefficient (s) = 1]. This implies that in order to maintain an atomically clean surface [surface concentration of impurities

lower than the detection limit of analytical techniques currently available (1% of a monolayer) (30)] for at least an hour, working pressures ≤ 10^{-10} Torr [so-called 'ultrahigh vacuum' (UHV) conditions] must be regularly attained. All the experimental work presented in this dissertation was performed under ultrahigh vacuum conditions. Pressures in the ultrahigh vacuum regime are maintained by the use of turbomolecular, and ion- and titanium-sublimation pumps. The following sections briefly describe the model surfaces used in this research, and the various surface-analytical methods employed for surface characterization.

1.3.1. Model Surfaces

Both polycrystalline (aggregate of several single-crystal planes), and single-crystal samples were employed in the present study. The polycrystalline sample was made up of iron, and single-crystal samples were those of iron and Ni_3Al, with (111) surface orientation. While polycrystalline specimens are widely used in most technological applications, they cannot be characterized on an atomic-scale with the real-space imaging techniques used in the present study (*vide infra*), due to their structural complexity. On the other hand, although single-crystals are generally not used in 'real-world' applications, they are amenable to structural characterization with a wide variety of analytical tools. Moreover, since many chemical reactions are highly site-specific and orientation-dependent, the knowledge of the reactivity of each single-crystal surface of a metal or alloy would substantially enhance the understanding of the behavior of the more complex polycrystalline systems.

Iron crystallizes in a body-centered cubic (bcc) lattice up to 1189 K, while Ni_3Al crystallizes in a face-centered cubic (fcc) lattice. The various low Miller-index surfaces

of bcc and fcc crystals are shown in Fig. 1.3 (31). From Fig. 1.3, it is clear that Fe(111) has the most open surface structure, while in the case of Ni_3Al, the atoms are most densely packed in the (111) surface.

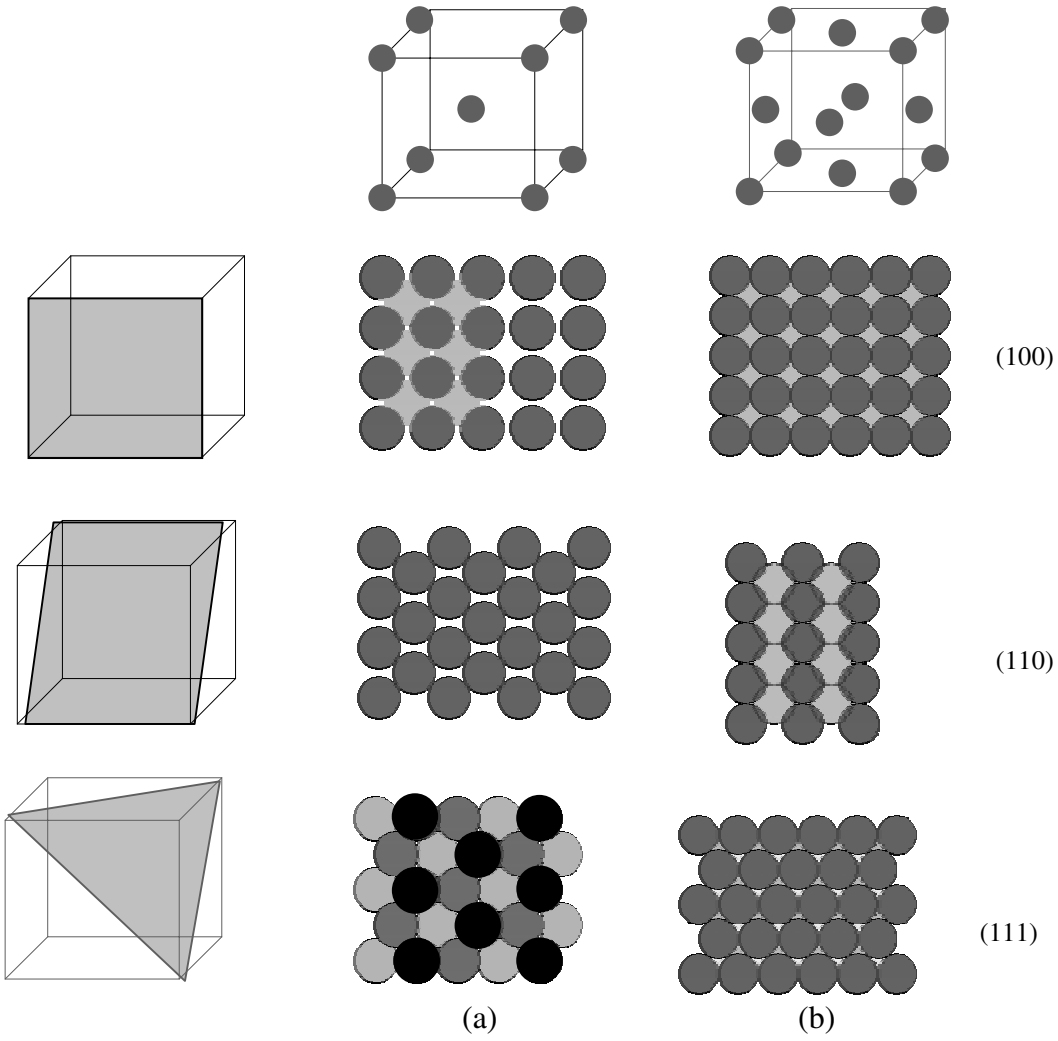

Fig. 1.3. Atomic arrangement in the low Miller index surfaces of (a) bcc and (b) fcc crystals.

1.3.2. Auger Electron Spectroscopy (AES)

The Auger emission process (Fig. 1.4) involves three electrons (32,33). When bombarded with an electron beam, an atom is ionized by expulsion of an electron from its

core shell (K), if the energy of the incident beam is greater than the electron binding energy. The ionized atom reverts back to its electronic ground state by a de-excitation process in which the core vacancy is filled by an outer electron (L_1). The difference in energies between the two energy levels (K and L_1) is transmitted in a radiationless process to a third electron (L_3) or the Auger electron, which then leaves the atom with a characteristic kinetic energy (Fig. 1.4). Auger electrons are classified according to the energy levels in the atom that are involved in their production. Thus, the process described in Fig. 1.4 depicts the loss of a KLL, or, more specifically, a KL_1L_3 electron, the kinetic energy (*K.E.*) of which is given by Eq. (1-10):

$$K.\,E. = E_K - E_{L_1} - E_{L_3} \tag{1-10}$$

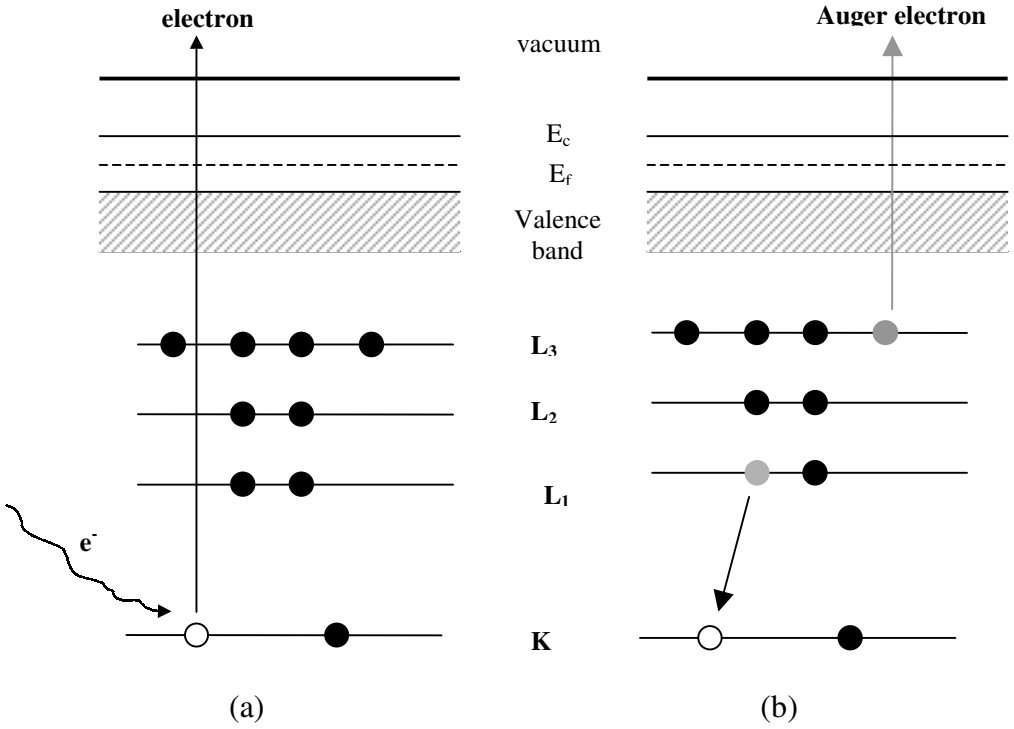

Fig. 1.4. Schematic of the Auger process: (a) removal of a core electron; and (b) Auger electron emission.

The experimental apparatus for AES (Fig. 1.5) (33) consists of an electron gun that produces an electron beam with an energy typically in the range from 2 keV to 3 keV as the excitation source. The electron gun is mounted inside a cylindrical mirror analyzer (CMA) as illustrated in Fig. 1.5. When the sample is irradiated with the electron beam from the source, electrons emitted from the sample pass through an aperture, and then are guided through the exit aperture on the CMA to the electron multiplier (detector). Auger spectra are plots of the signal intensity versus the Auger electron energy. Because Auger

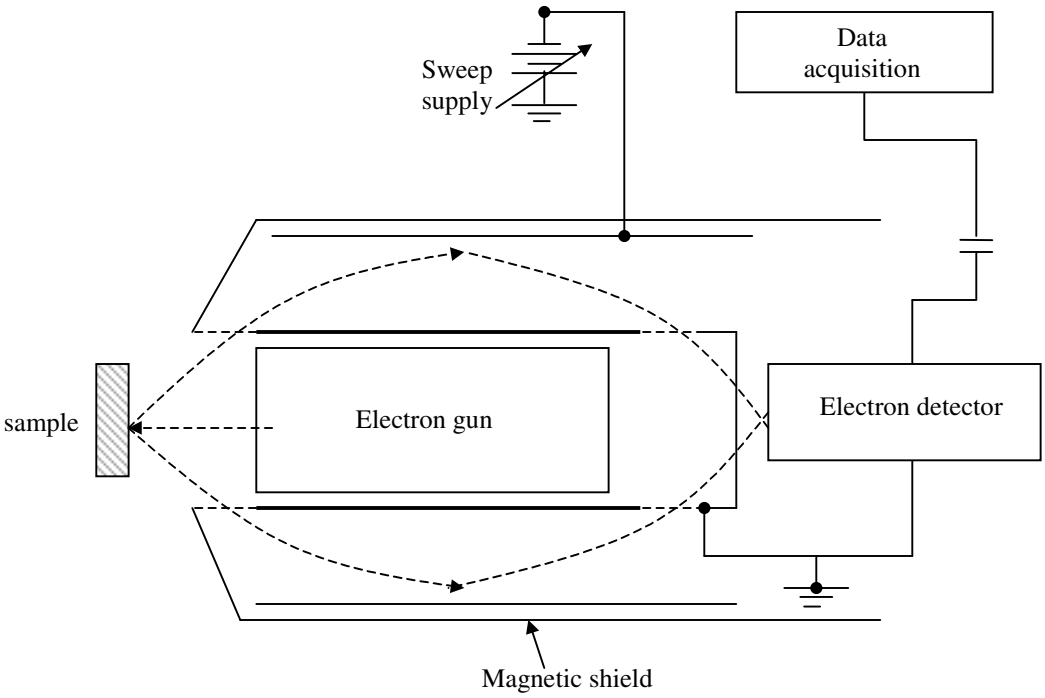

Fig. 1.5. Experimental apparatus used in Auger electron spectroscopy.

electron transitions generally appear as small features superimposed on a rather large continuous background of secondary electrons (Fig. 1.6), the energy distribution function

N(E) is electronically differentiated into dN(E)/dE in order to facilitate easy identification and analysis of the Auger transitions. Since each element has its own unique set of binding energies, Auger electron spectroscopy can be used to ascertain the elemental composition of a given sample surface. The peak-to-peak height (pph) intensity in the derivatized Auger spectrum (Fig. 1.6b) is proportional to the surface concentration of the element. In addition, chemical shifts or variations in peak shapes or fine structures due to the presence of non-metallic adsorbates (carbon, sulfur, oxygen) can be sometimes detected to obtain information pertaining to the chemical environment of the atoms in the surface (32).

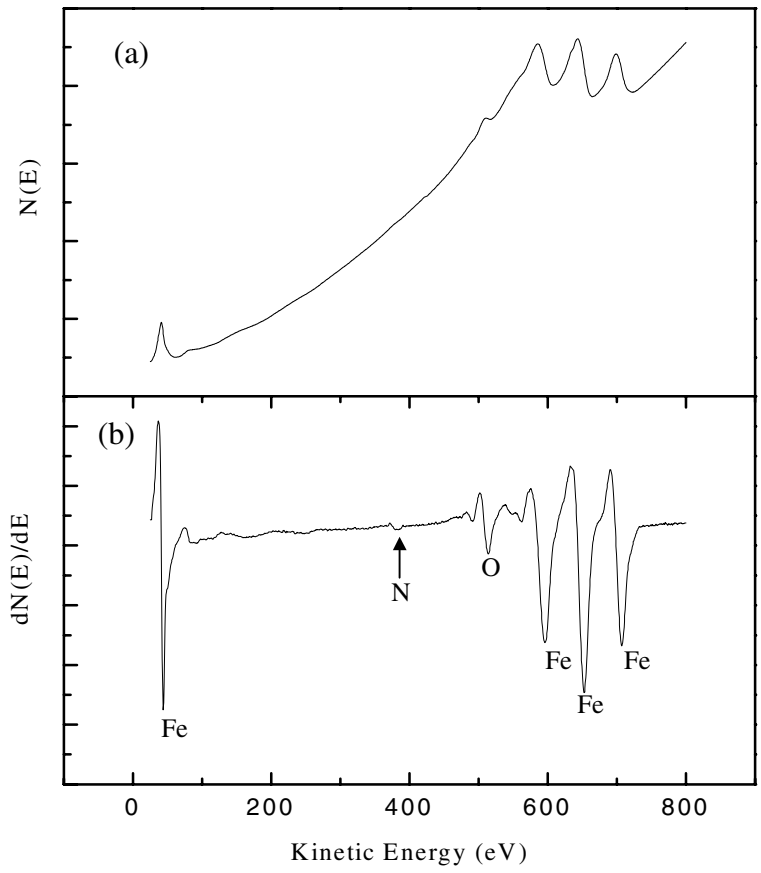

Fig. 1.6. Auger spectra from a contaminated iron sample in the (a) undifferentiated, and (b) differentiated modes.

1.3.3. Low Energy Electron Diffraction (LEED)

Low energy electron diffraction (LEED) is a technique based on the wave-particle duality of electrons, by which an electron beam can be regarded as a group of particles, and also as a series of waves incident upon the target material (sample) (31). The wavelength (λ) of the incident electron beam is derived from the de Broglie relationship (29):

$$\lambda = \sqrt{\frac{150}{E(eV)}} \qquad (1\text{-}11)$$

From Eq. (1-11), it can be estimated that in order to satisfy the atomic diffraction condition (λ must be smaller than or comparable to interatomic spacings), electrons with energies of the order of 10-200 eV must be used in LEED experiments. These low-energy electron waves are scattered by regions of high electron density, i.e., the surface atoms, to generate new wavelets that will interfere with one other, either constructively or destructively. The condition for constructive interference is that the distance between the wave fronts from the adjacent atoms ('path difference') must be an integral multiple of the wavelength of the incident electron beam (Fig. 1.7a) (33). If we assume a one-dimensional array of scattering centers with a nearest-neighbor separation *a* (Fig. 1.7a), then the condition for constructive interference is expressed mathematically as (33):

$$\text{Path difference (pd)} = a \sin\theta = n\lambda \qquad (1\text{-}12)$$

Depending upon the *a* and λ, there may be several angles θ for which constructive interference can occur. Thus, there will be an imaginary 'cone' around the axis of the row of atoms, where constructive interference is feasible, and where the probability of finding the electrons is finite (Fig. 1.7b). This situation can be extended to a single-

crystal surface that consists of a two-dimensional periodic array of atoms with primitive interatomic spacings *a* and *b*. Here, two sets of diffraction conditions must be satisfied

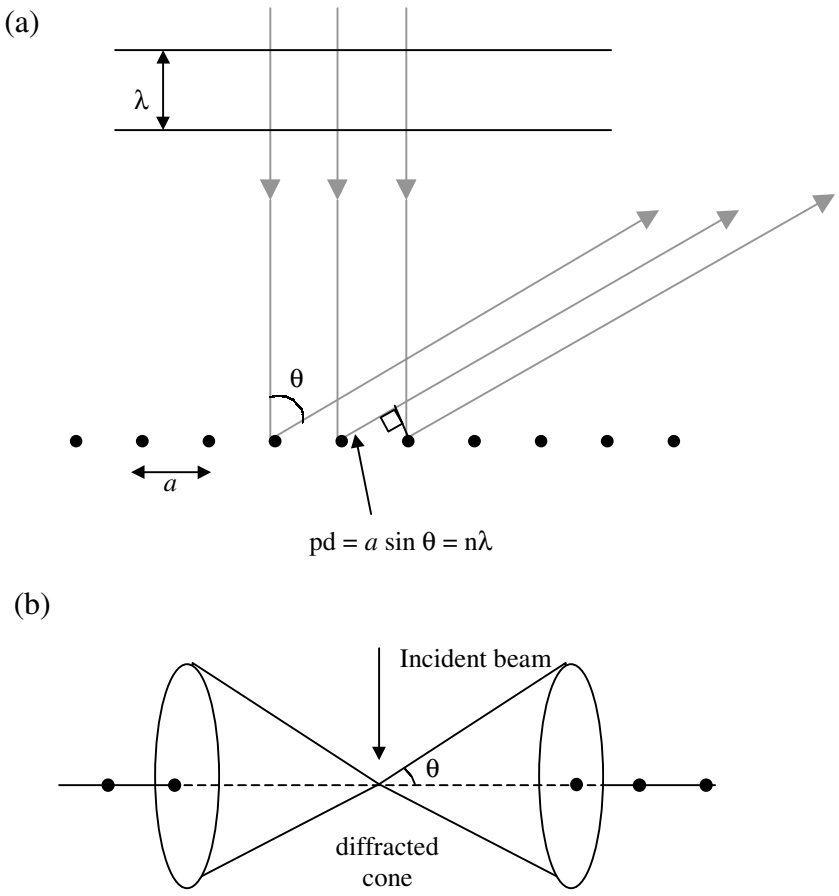

Fig. 1.7. (a) Diffraction of a wave from a one-dimensional array of scattering centers, (b) cone of constructive interference.

simultaneously, one for each lattice spacing: $n_a\lambda_a = a \sin \theta_a$, and $n_b\lambda_b = b \sin \theta_b$. Each set generates its own 'cone'. Because both conditions must be met concurrently, electron density is maximum only at the places where these cones intersect. As the intersection of two cones with a common origin and nonparallel axes is a set of lines, it can be seen that when an electron is diffracted from a periodic two-dimensional arrangement of atoms in a single-crystal surface, it can only be scattered along a set of lines or beams dispersed

from the surface (32,33). If these diffraction beams are intercepted by means of a detection device such as a fluorescent screen, the resulting diffraction spots can be observed visually.

In a typical LEED experiment, a collimated monoenergetic beam of electrons is directed at the surface of a single-crystal (Fig. 1.8), where a small fraction of the incoming electrons is elastically backscattered (34). The inelastically scattered electrons are filtered out by a set of hemispherical retarding grids, while the elastically scattered (diffracted) electrons are post-accelerated onto a fluorescent screen (detector) by a

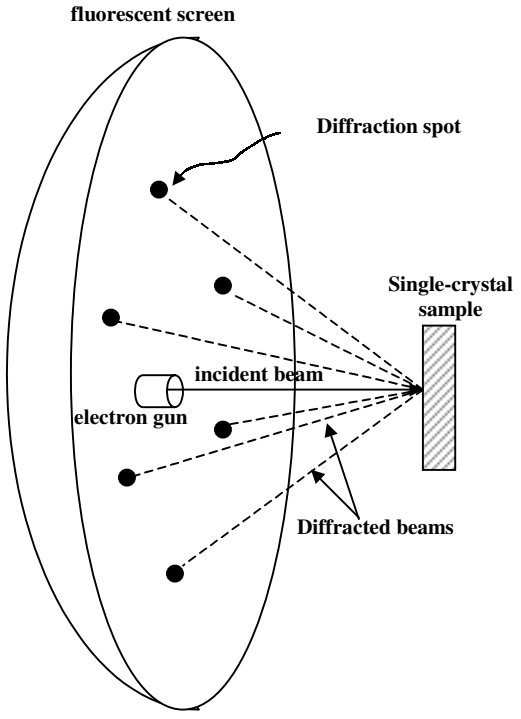

Fig. 1.8. Experimental set-up for LEED. The retarding grids are not shown in the figure.

positive potential (34). The diffraction pattern observed on the fluorescent screen (Fig. 1.8) reflects the ordered arrangement of atoms in the surface of the single-crystal sample.

These spots are indexed as (n_a, n_b), where n_a and n_b are the integral number of wavelengths in the *a* and *b* directions in the surface, respectively. Since even low levels of surface impurities can significantly alter the surface structure, the crystal and the detection system are maintained in ultrahigh vacuum.

Commensurate, two-dimensional surface structures are generally categorized according to the Wood's notation, the general form of which is given by (m×n)*R*α° (35). Here, the numbers m and n correspond to two independent 'stretch factors' of the basic unit-cell of the clean substrate in the two different surface directions (35), i.e., these are the numbers by which the basic substrate unit-cell must be multiplied to derive the overlayer unit-cell. α represents the angle by which the unit-cell of the overlayer is rotated from that of the substrate. It is important to note that while one can interpret the size, symmetry and rotational alignment of an adsorbate unit-cell using the qualitative LEED method (31) described above, it is not possible to definitively allocate nuclear positions from diffraction patterns alone in the case of some adsorbate-induced surface structures. With the use of quantitative LEED measurements, however, the intensities of the various diffraction spots can be monitored as a function of the energy of the incident electron beam to produce I-V curves, which can be compared with theoretical models to establish atomic positions in the surface (29,31).

1.3.4. Scanning Tunneling Microscopy (STM) and Spectroscopy (STS)

The operation of a scanning tunneling microscope is based on the principle that when an atomically sharp metal tip (typically made from tungsten or Pt-Ir) is brought into close proximity (≈ 3-5 Å) to a conducting or a semiconducting surface, the wave functions of the tip and the sample overlap (36,37), decaying exponentially into the gap

(Fig. 1.9) (36). If a sufficient bias voltage (denoted by V or U_{gap}) is applied to the sample, electrons tunnel quantum mechanically from the filled states in the tip into the empty states in the sample through the gap, or vice versa, depending upon the polarity of the applied voltage (36,37), as illustrated in Fig. 1.9.

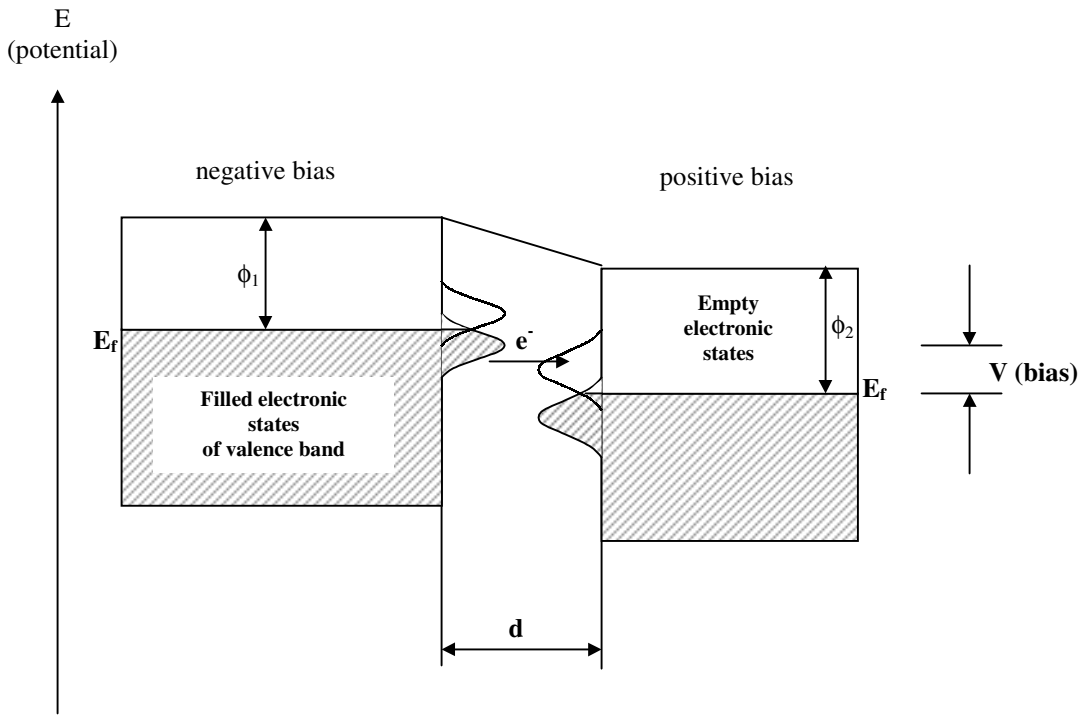

Fig. 1.9. Schematic representation of quantum mechanical tunneling of electrons between two metallic electrodes separated by a gap. V is the applied voltage, and E_f is the energy of the Fermi level.

The net flow of electrons across the gap, called the tunneling current (I_t), is extremely sensitive to tip-sample separation (d), and, at low voltage and temperature, I_t is given by the following equation (38):

$$I_t \propto e^{-2\kappa d} \tag{1-13}$$

where the decay constant for the wave functions in the barrier (κ) is given by $\kappa = \frac{\sqrt{2m\phi}}{\hbar}$,

in which ϕ is the local barrier height or the effective local work function, and $\hbar = \frac{h}{2\pi}$ (38). Since the tunneling current (I_t) changes exponentially with tip-sample distance [Eq. (1-13)], corrugations or depressions in the sample surface will produce variations in the current as the tip is scanned across the surface, that is, the tunneling current tends to increase (decrease) when the tip-sample distance decreases (increases). This exceptional sensitivity enables STMs to image sample surfaces with sub-angstrom precision vertically, and atomic resolution laterally.

In a scanning tunneling microscope (Fig. 1.10), the movement of the tip or the

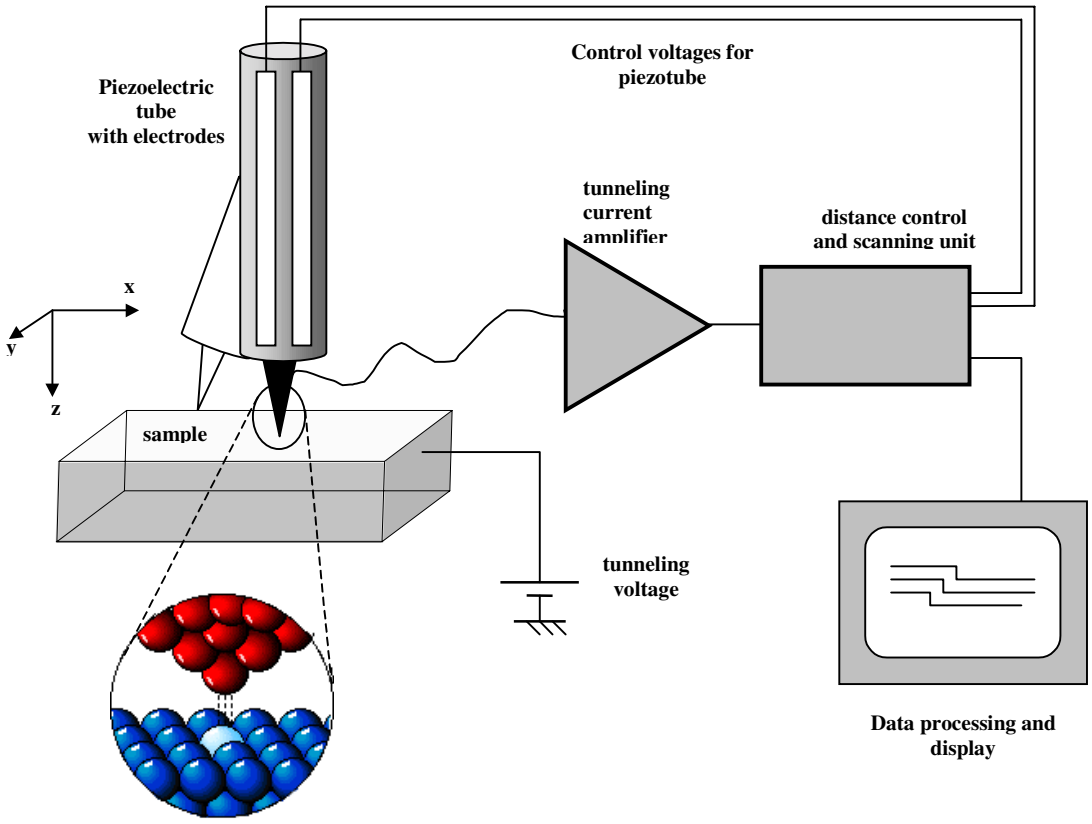

Fig. 1.10. Schematic of a scanning tunneling microscope.

sample is effectively controlled by the use of a piezoelectric material that expands in atomic dimensions. By raster-scanning the tip over the sample, and applying a preset constant value (*I*) for the current (normally in the range from 0.1 to 5 nA) in a feedback circuit ('constant-current' imaging), the vertical displacements of the tip can be mapped as it follows the contour of density of states at the surface in order to generate a 'topographic image' of the surface (Fig. 1.10).

In addition to imaging a sample surface, an STM is used to obtain chemical information about a given surface, in the scanning tunneling spectroscopy (STS) mode (Fig. 1.11).

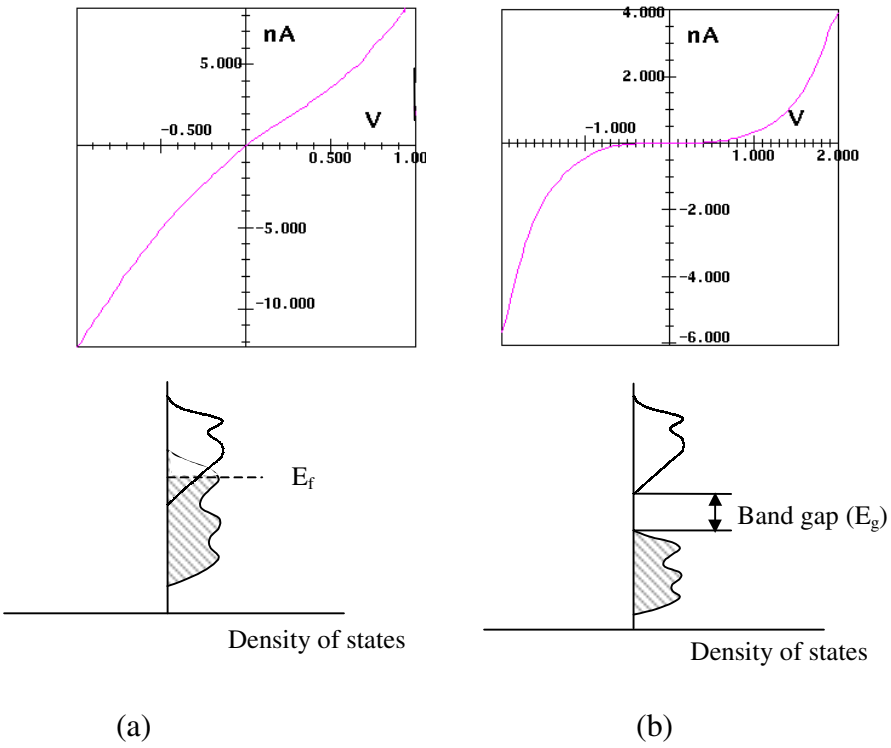

Fig. 1.11. Typical current imaging tunneling spectroscopy (CITS) curves for a (a) conducting and (b) semiconducting surface.

Different kinds of STS are currently employed for this purpose (39). In the present research, STS measurements involved ramping the voltage (V) over an area of interest and recording the tunneling current (I) simultaneously, while maintaining a constant tip-sample distance. The current vs. voltage (I-V) curves obtained are characteristic of the electronic structure at a specific site in the surface. From the shape of the I-V curves, it is possible to ascertain whether the region of interest is metallic or semiconducting (Fig. 1.11). This method is termed current imaging tunneling spectroscopy (CITS) (39).

1.4. Chapter References

(1) Meier, G. H. *Mater. Corr.* **1996**, *47*, 595.

(2) Mrowec, S. *Oxid. Met.* **1995**, *44*, 177.

(3) Smialek, J. L. *Metall. Trans. A* **1991**, *22*, 739.

(4) Lees, D. G. *Oxid. Met.* **1987**, *27*, 75.

(5) Oudar, J. *Mater. Sci. Eng.* **1980**, *42*, 101.

(6) Seah, M. P. in *Practical Surface Analysis: Auger and X-ray Photoelectron Spectroscopy*; 2 ed.; Briggs, D. and Seah, M. P., Eds.; Wiley: New York, 1990; Vol. 1, p 311.

(7) Stott, F. H. *Rep. Prog. Phys.* **1987**, *50*, 861.

(8) Hou, P. Y.; Stringer, J. *Oxid. Met.* **1992**, *38*, 323.

(9) Smialek, J. L. *Metall. Trans. A* **1987**, *18*, 164.

(10) Baxter, D. J.; Natesan, K. *Oxid. Met.* **1989**, *31*, 305.

(11) Cabibil, H.; Kelber, J. A. *Surf. Sci.* **1995**, *329*, 101.

(12) Cabibil, H.; Kelber, J. A. *Surf. Sci.* **1997**, *373*, 257.

(13) Kelber, J. A.; Addepalli, S. G.; Lin, J.-S.; Cabibil, H. in *High Temperature Corrosion and Materials Chemistry*; Hou, P. Y., McNallan, M. J., Oltra, R., Opila, E. J. and Shores, D. A., Eds.; The Electrochemical Society, Inc.: San Diego, CA, 1998; Vol. 98-99, p 190.

(14) Lin, J.-S.; Ekstrom, B.; Addepalli, S. G.; Cabibil, H.; Kelber, J. A. *Langmuir* **1998**, *14*, 4843.

(15) Grabke, H. J.; Wiemer, D.; Viefhaus, H. *Appl. Surf. Sci.* **1991**, *47*, 243.

(16) Lobnig, R. E.; Grabke, H. J. *Corros. Sci.* **1990**, *30*, 1045.

(17) Smeggil, J. G.; Funkenbusch, A. W.; Bornstein, N. S. *Metall. Trans. A* **1986**, *17*, 923.

(18) Fox, P.; Lees, D. G.; Lorimer, G. W. *Oxid. Met.* **1991**, *36*, 491.

(19) Fontana, M. G. *Corrosion Engineering*; 3 ed.; McGraw-Hill, Inc.: New York, 1986.

(20) Jones, D. A. *Principles and Prevention of Corrosion*; Macmillan Publishing Company: New York, 1991.

(21) Scully, J. C. *The Fundamentals of Corrosion*; 3 ed.; Pergamon Press: New York, 1990.

(22) Birks, N.; Meier, G. H. *Introduction to High Temperature Oxidation of Metals*; 1 ed.; Edward Arnold Publishers Ltd.: London, 1983.

(23) Lide, D. R. *CRC Handbook of Chemistry and Physics*; 74 ed.; CRC Press: Boca Raton, 1994, p 4/36.

(24) Meier, G. H.; Pettit, F. S. *Mater. Sci. Technol.* **1992**, *8*, 331.

(25) Shores, D. A. *The Electrochemical Society Interface* **1997**, *6*, 42.

(26) Panzner, G.; Egert, B. *Surf. Sci.* **1984**, *144*, 651.

(27) Hardegree, E. L.; Ho, P.; White, J. M. *Surf. Sci.* **1986**, *165*, 488.

(28) Lide, D. R. *CRC Handbook of Chemistry and Physics*; 74 ed.; CRC Press: Boca Raton, 1994, p 9/123.

(29) Somorjai, G. A. *Introduction of Surface Chemistry and Catalysis*; John Wiley & Sons, Inc.: New York, 1994.

(30) Somorjai, G. A. *MRS Bull.* **1998**, *23*, 11.

(31) Nix, R. M. *An Introduction to Surface Chemistry*: http://www.chem.qmw.ac.uk/surfaces/scc/sccinfo.htm, 1997.

(32) Ertl, G.; Küppers, J. *Low Energy Electrons and Surface Chemistry*; Verlag Chemie: Weinheim, 1974; Vol. 4.

(33) Feldman, L. C.; Mayer, J. W. *Fundamentals of Surface and Thin Film Analysis*; P T R Prentice Hall: Englewood Cliffs, 1986.

(34) Ohtani, H.; Kao, C.-T.; Van Hove, M. A.; Somorjai, G. A. *Prog. Surf. Sci.* **1986**, *23*, 155.

(35) Van Hove, M. A. *Heterogeneous Chemistry Reviews* **1995**, *21*, 81.

(36) Besenbacher, F. *Rep. Prog. Phys.* **1996**, *59*, 1737.

(37) Lieber, C. M. in *Chemical and Engineering News*; 1994, p 28.

(38) Tersoff, J.; Lang, N. D. in *Scanning Tunneling Microscopy*; Stroscio, J. A. and Kaiser, W. J., Eds.; Academic Press, Inc.: New York, 1993; Vol. 27, p 1.

(39) Wiesendanger, R. *Scanning Probe Microscopy and Spectroscopy: Methods and Applications*; Cambridge University Press: Cambridge, 1994.

CHAPTER 2

INTERACTIONS AT THE ALUMINUM-SULFUR-IRON INTERFACE: SULFUR INHIBITION OF ALUMINUM OXIDATION

2.1. Introduction

Sulfur is a pervasive bulk impurity in many nickel, iron and chromium alloys. The segregation of sulfur to grain boundaries is associated with grain boundary embrittlement (1) and oxide scale spallation (2,3). Binary and ternary alloys containing aluminum are frequently used in aggressive, high-temperature corrosive environments because such alloys form corrosion-resistant aluminum oxide scales (4). Sulfur has been shown (3,5-7) to segregate from the metal bulk to the metal-oxide interface, sharply degrading the thermal stability of the interface, as witnessed by the spalling of the oxide upon cooling. The effects of sulfur are also observed in chromia- and ferrous oxide-forming systems (8-12). Because of the technological importance of alumina-forming alloys, the interactions of sulfur at alumina-metal interfaces are of particular interest, as well as of relevance to a broader understanding of the properties of composite materials.

Experimental studies (3,5) have shown that spallation of alumina scales during cyclic oxidation is directly tied to the presence of sulfur at the metal-alumina interface. Experimental studies of polycrystalline alloy/alumina (3,5,6) and single-crystal alumina/Ni(poly) surfaces (7) have demonstrated that sulfur will segregate to an existing alumina-metal interface. Prevention of interfacial sulfur segregation, either by removing sulfur from the bulk prior to interface formation (3), or by the introduction of yttrium,

zirconium or certain other "reactive elements" (2,13-15) enhances the thermal stability of the alumina overlayer. Both experimental (3,5) and theoretical studies (16) indicate that sulfur-induced spallation of oxide overlayers is connected with the disruption of interfacial chemical bonding. The exact mechanism by which this occurs is still the subject of considerable debate (3,6,8,9,11,13-16).

In an effort to elucidate complex interfacial chemical interactions, some studies have been carried out on model interfaces (9,11,12,17,18), often formed under ultra-high vacuum (UHV) conditions. Studies carried out on the Fe/S/Fe-oxide system (9,11) have demonstrated that interfacial sulfur will react to form SO_2, thus scissioning interfacial bonds, and resulting in the dewetting of thin iron oxide overlayers from iron substrates at significantly lower temperatures than those observed in the absence of sulfur. Studies have also been carried out on single-crystal nickel surfaces (18), demonstrating that the presence of interfacial sulfur will disrupt the epitaxial growth of the oxide. Because the electronic charge distribution of sulfur-metal bonds at a surface may differ significantly from those in the bulk phase (9,11,19) the chemical reaction pathways at surfaces and interfaces may differ considerably from those expected from thermodynamics calculations using free energies derived from bulk values (11).

In order to study the effects of sulfur on interfacial chemical bonding under well-controlled conditions, we have deposited monolayer and submonolayer concentrations of aluminum onto clean and sulfur-covered Fe(111) single-crystal surfaces under UHV conditions. Deposition of aluminum onto the S/Fe(111)(1×1) surface leads to aluminum insertion between the sulfur atoms and the iron substrate, resulting in an Fe-Al-S disordered adlayer, and inhibited oxidation of the aluminum upon exposure to O_2 at 300

K. In the absence of sulfur, the Fe(111) undergoes a pseudo rectangular reconstruction -- the so-called "clock" structure as evidenced by the complex LEED pattern that is observed (20). Aluminum deposited on the sulfur-free Fe(111)(clock) surface is readily oxidized at 300 K.

2.2. Experimental

Experiments were carried out in a UHV system that is drawn schematically in Fig. 2.1 (21). This chamber is evacuated by turbomolecular, and ion- and titanium-sublimation pumps, to maintain a base pressure $\leq 5 \times 10^{-11}$ Torr after bake-out. Typical working pressures range from 9×10^{-11} to 3×10^{-10} Torr. The system is equipped with an electron-beam (e-beam) evaporation source for deposition (PVD) of ultrathin layers of pure metals, and an ion gun for sputter-cleaning the sample. Additional facilities include four-grid optics for low energy electron diffraction (LEED), a scanning tunneling microscope (STM), an Auger electron spectrometer (AES), manual leak valves for introducing small amounts of gases (O_2, H_2S) into the chamber, and a quadrupole mass analyzer (QMA) for detecting residual gases in the chamber. Samples are introduced from air into the UHV chamber via a load-lock chamber by means of a magnetic linear feedthrough. Sample transfer to the STM stage is accomplished with the use of a wobble-stick. A high precision *x-y-z* manipulator allows translation of the sample along the three directions within the chamber, as well as rotation about the manipulator axis.

Auger spectra were recorded using a cylindrical mirror analyzer (CMA) with a coaxial electron gun (Physical Electronics). The electron gun was operated with an excitation energy of 3 keV with an estimated spot diameter of 0.2 cm^2. In order to assure

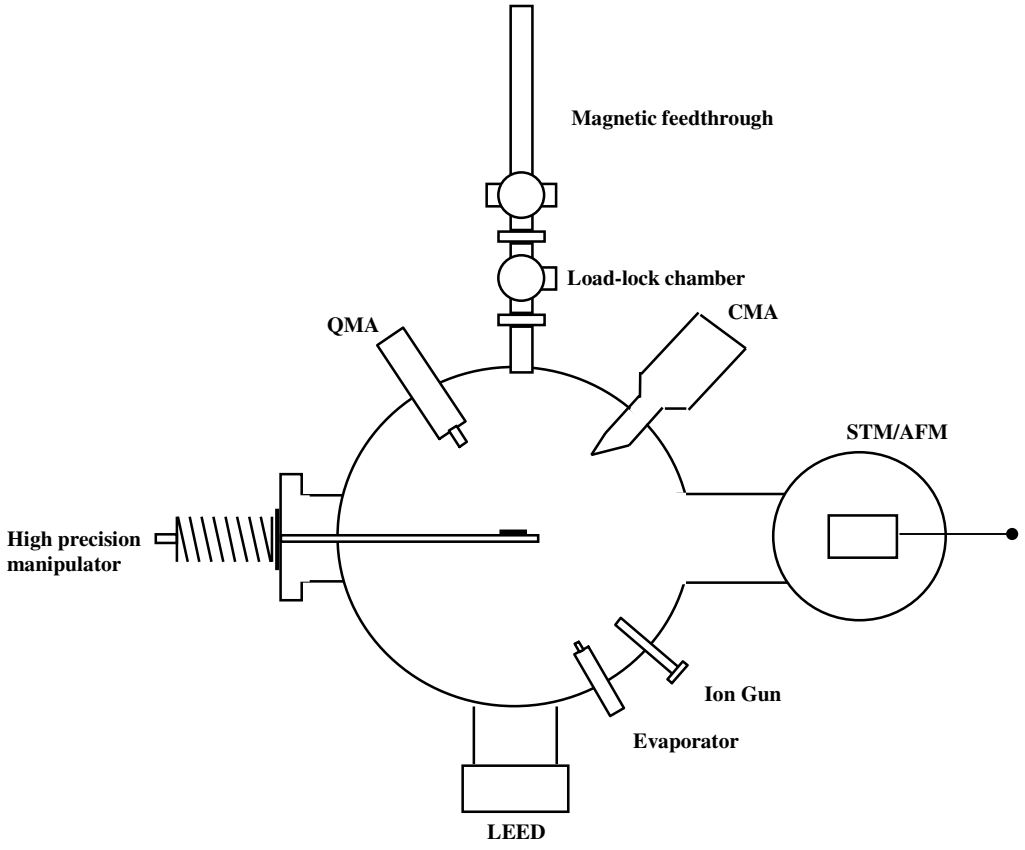

Fig. 2.1. Schematic of the top view of the UHV-AES/LEED/STM chamber.

consistent peak energies, the sample-to-analyzer distance was always adjusted by measuring the energy of the 3000 eV elastic peak (22). Auger spectra were acquired in the N(E) mode and then digitally derivatized (23) for display in the dN(E)/d(E) mode. Aluminum, sulfur and oxygen intensities were determined from the Auger peak-to-peak heights of the Al(LVV), S(LVV) and O(KVV) signals at 68 eV, 152 eV, and 510 eV, respectively. Both the Fe(MVV) transition (~ 47 eV) and the Fe(LMV) transition (651 eV) were monitored. Atomic concentrations were calculated from relative intensities and published (24) atomic sensitivity factors, according to:

$$N_A/N_B = I_A X_B/I_B X_A \quad (2\text{-}1)$$

where N_A, I_A, and X_A represent, respectively, the atomic concentration, the peak to peak height (pph) intensity, and the atomic sensitivity factor of element A. The difference in mean free path lengths for the two transitions, ~ 4.5 Å for the Fe(MVV) vs. 11.4 Å for the Fe(LMV) transition (25,26), provides a convenient method for calibrating the thickness of an attenuating overlayer by using the equation

$$I = I_0 e^{-d/\lambda} \quad (2\text{-}2)$$

In Eq. (2-2), I_0 is the intensity of the Auger peak [normalized relative to Fe(LMV)] before aluminum deposition, and I is the intensity of the peak [normalized relative to Fe(LMV)] after aluminum deposition, d is the thickness of the aluminum overlayer, and λ is the inelastic mean free path of the element. The percentage attenuation in the Fe(MVV) and S(LVV) intensities can be calculated as follows:

$$\% \text{ Attenuation} = \left[\frac{I_0 - I}{I_0}\right] \times 100 \quad (2\text{-}3)$$

In addition, the Fe(MVV) and Al(LVV) spectral lineshapes and energies, which are sensitive to changes in electronic structure due to oxidation (27-30), were monitored.

During Auger and LEED measurements, the sample was mounted on a heater block attached to a UHV sample manipulator. Sample temperatures during annealing were recorded with a type K thermocouple mounted at the resistive current heater block, and not directly attached to the sample. Therefore the sample annealing temperatures reported here must be regarded as approximate.

Aluminum deposition was carried out from an e-beam heated crucible mounted within the UHV chamber. Evaporative deposition of aluminum was carried out at constant power [32 Watts (W)] for varying times. Since the deposition rate proved sensitive to slight fluctuations in power, aluminum depositions are reported in terms of power × time (W sec) (31). During aluminum deposition, the pressure in the chamber stayed below 1×10^{-9} Torr. No contamination of deposited aluminum was observed in Auger spectra. Pressure in the ionization chamber was measured using a nude ion gauge mounted out of line of sight of the sample, and calibrated for N_2. O_2 exposures were carried out using electronic-grade oxygen without further purification. The gas was admitted to the UHV chamber via a manual leak valve and stainless steel doser tube. O_2 exposures were carried out by backfilling the chamber and are reported here in terms of Langmuir (L; $1L = 10^{-6}$ Torr-sec). Reported exposures have not been corrected for flux to the sample, or the different ion gauge sensitivities of N_2 and O_2.

2.3. Results

2.3.1. Clean and Sulfur-Modified Fe(111)

The same Fe(111) single-crystal used in a previous study (20) was cleaned in UHV by a combination of Ar-ion sputtering and annealing so as to remove observable amounts of carbon, nitrogen and oxygen from the surface. Annealing the sample to 870 K in UHV resulted in the complex LEED pattern reported previously (20) and referred to as the “clock structure”. This clock structure and the corresponding atomic-resolution STM image (20) indicate a complex reconstruction which may be effected by low levels of oxygen or other impurities on the otherwise clean Fe(111) surface. This surface shall

be termed the Fe(111)(clock) surface. Annealing to 925 K - 975 K in UHV resulted in the (1×1) LEED pattern reported previously, with S/Fe pph ratios of ~ 1.0, and an atomic-resolution STM image (20,32) corresponding to the bulk-terminated Fe(111) structure. Previous studies (20,32) indicate that a S/Fe ratio of 1.0 corresponds closely to one "monolayer" (ML) of sulfur -- one sulfur atom in every three-fold site on the Fe(111) surface. This surface is labeled the S/Fe(111)(1×1) surface.

2.3.2. Aluminum Deposition on S/Fe(111)(1×1) vs. Fe(111)(clock)

The changes in relative aluminum and sulfur intensities as a function of aluminum deposition exposures are shown in Fig. 2.2. Both aluminum and sulfur Auger intensities

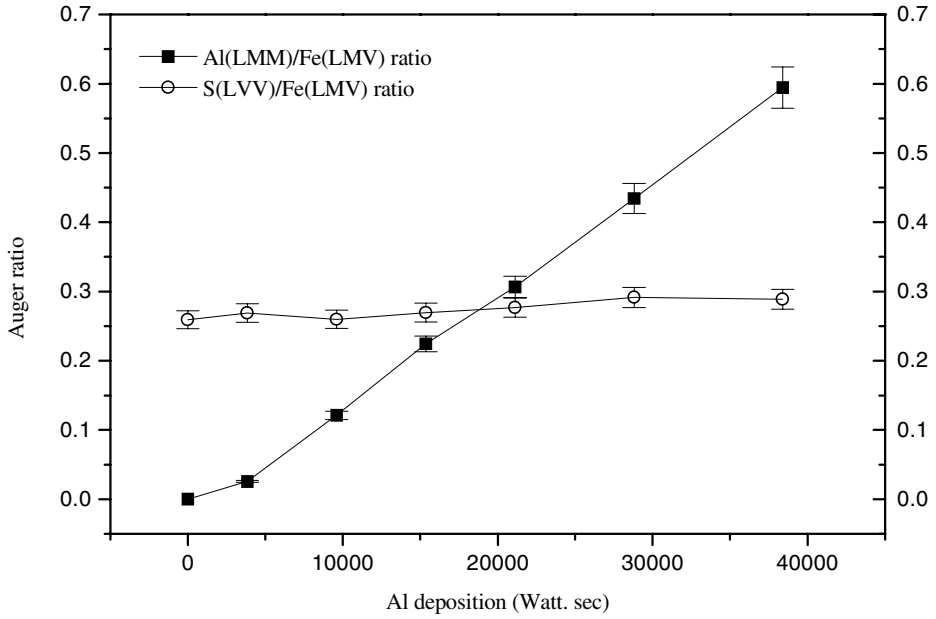

Fig. 2.2. Al(LVV)/Fe(LMV) and S(LVV)/Fe(LMV) ratios vs. aluminum deposition (W sec).

were normalized relative to the Fe(LMV) intensity, since this transition is less readily attenuated than the Fe(MVV) transition. As indicated in Fig. 2.2, the relative aluminum intensity increases linearly with deposition time, indicating a constant sticking coefficient. In contrast, the relative sulfur intensity increased slightly during aluminum deposition, indicating no significant attenuation by an aluminum overlayer. The maximum aluminum coverage displayed in Fig. 2.2 corresponds to an Al/S atomic ratio of 2.1(± 0.1). Since the sulfur coverage on this surface, as discussed above, is quite close to one sulfur atom for every surface three-fold site (20,32), maximum aluminum coverage corresponds to two aluminum atoms for every sulfur atom, or every three-fold site on the iron surface.

LEED images (not shown) became more diffuse with increasing aluminum coverage, indicating a disordered aluminum adlayer. This was confirmed by STM images (Fig. 2.3) which show constant-current scans of the S/Fe(111) surface before and after aluminum deposition. These images indicate conformal aluminum coverage of the surface, as opposed to the formation of three-dimensional islands interspersed with large patches of uncovered surface. The relative changes in the Fe(MVV)/Fe(LMV) intensity are shown in Fig. 2.4 as a function of aluminum deposition exposure. The data in Figs. 2.2 and 2.4 indicate that the aluminum surface coverage is sufficient to significantly attenuate the normalized Fe(MVV) intensity. The electron inelastic mean free paths at energies corresponding to the Fe(MVV) and S(LVV) intensities are 4.5 Å and 8.3 Å respectively (26,31). Therefore, using Eqs. (2-2) and (2-3), if the sulfur remained at the Fe-Al interface during aluminum deposition, the ~ 32% decrease in the normalized Fe(MVV) intensity [relative to the Fe(LMV) intensity; Fig. 2.4] would also be

accompanied by a decrease of ~ 20% in the normalized S(LVV) intensity (33). A significant decrease in S(LVV) intensity is observed for the ~ 5 Å thick iron oxide

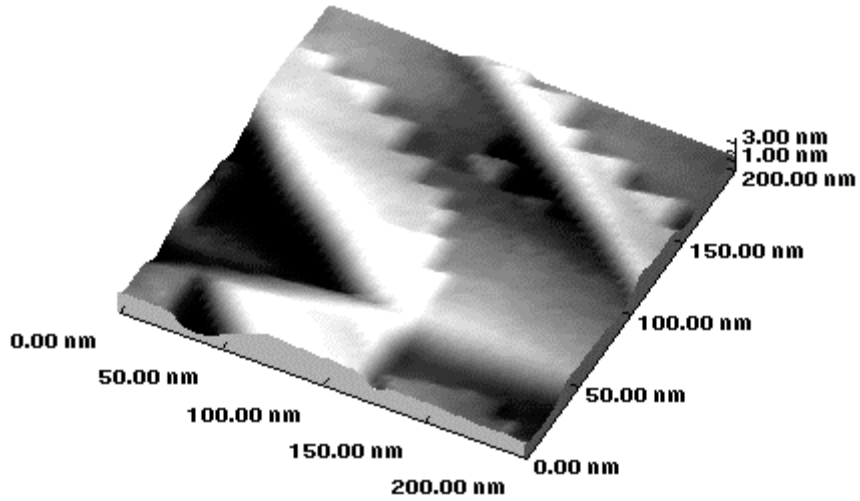

(a)

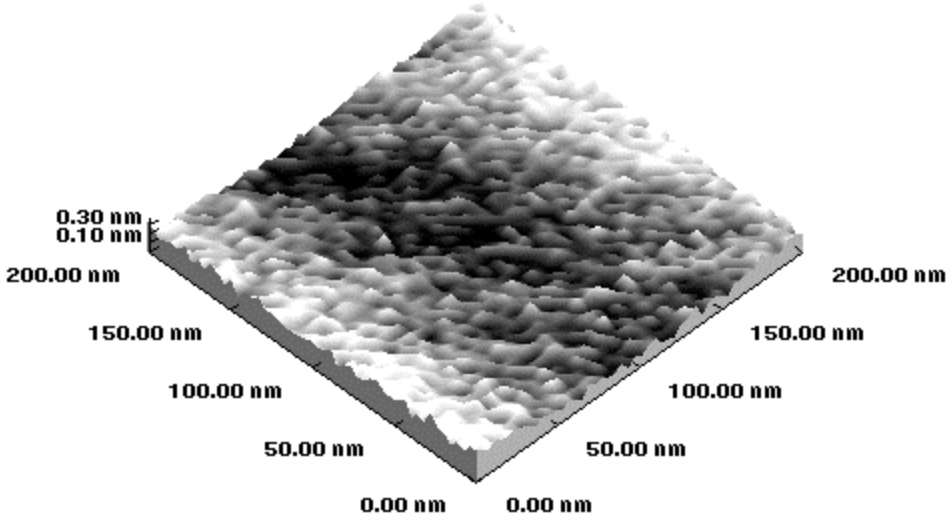

(b)

Fig. 2.3. STM images (a) before (U_{gap}= + 0.1 V, I = 1 nA), and (b) after ~ 2 monolayers aluminum deposition on S/Fe(111)(1×1) (U_{gap} = + 0.2 V, I = 1 nA).

overgrowth of a sulfur-modified iron substrate (9). In contrast, an increase of ~ 11.5% in the normalized S(LVV) intensity is observed (Fig. 2.2). The increase of the normalized S(LVV) signal upon deposition of the aluminum therefore demonstrates that sulfur atoms are not buried by the deposition of an aluminum overlayer. Instead, the deposited aluminum atoms apparently are inserted between sulfur atoms and the Fe(111) substrate.

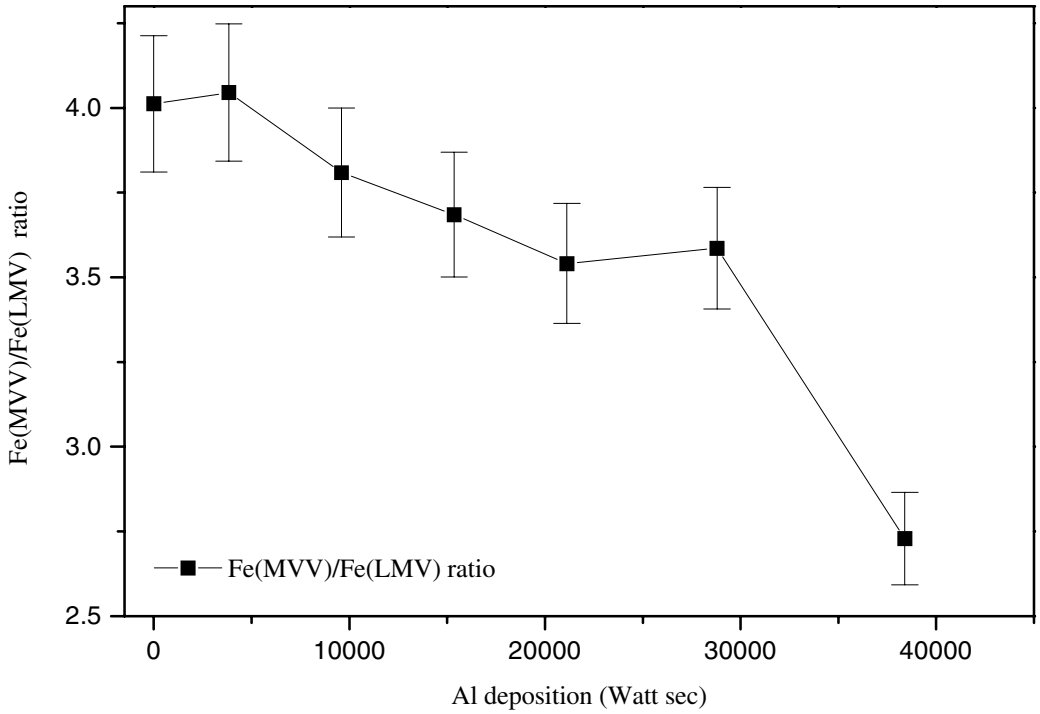

Fig. 2.4. Fe(MVV)/Fe(LMV) ratio vs. aluminum deposition (W sec).

Deposition of aluminum on clean Fe(111) was accomplished in a single deposition of 38,400 W sec. LEED spectra (not shown) indicated a diffuse pattern. Figure 2.5 shows Auger spectra of the Fe(111) clock surface before and after aluminum deposition. The relative attenuation of the Fe(MVV) intensity [normalized to the

Fe(LMV) intensity] is 24% (Fig. 2.5), comparable to that observed for deposition on the S/Fe(111)(1×1) surface (32%) (Fig. 2.4). Previous studies have shown that at extremely low deposition rates, a kinetically limited amount of Fe-Al alloying occurs at room temperature (34). No attempt was made, however, to determine whether such alloying occurred in this case.

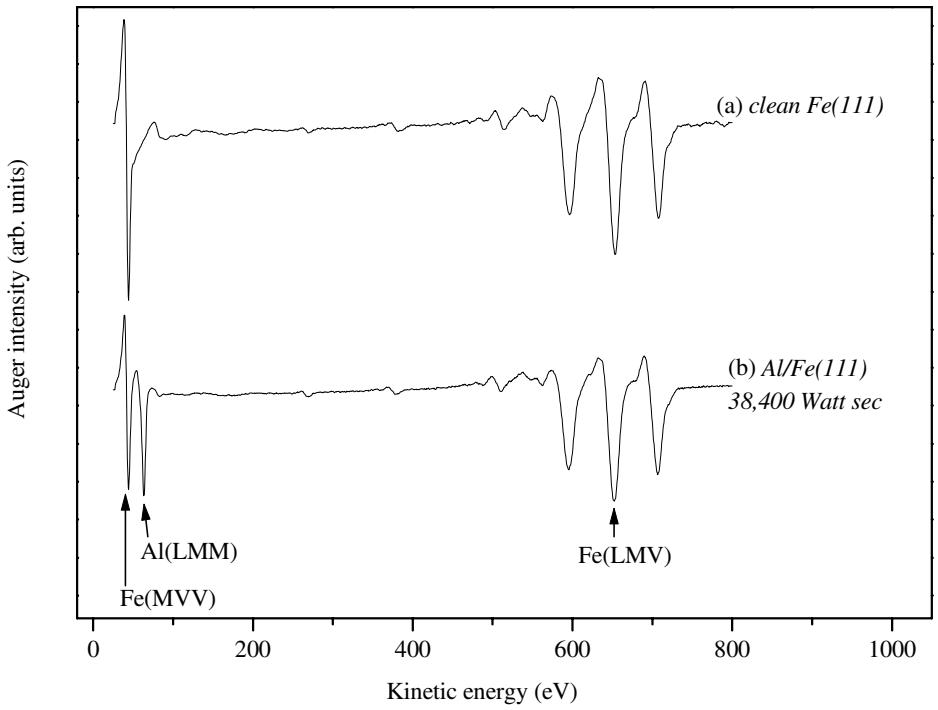

Fig. 2.5. Auger spectra of the Fe(111)(clock) surface:
(a) before and (b) after aluminum deposition.

2.3.3. Oxidation Studies

Both Al/S/Fe(111)(1×1) and the Al/Fe(clock) samples were oxidized by exposure to O_2 at 300 K under UHV conditions (maximum O_2 pressure: 1×10^{-7} Torr). The oxidation of iron or aluminum is characterized by changes in the Fe(MVV) and Al(LVV)

spectra. Changes in the Fe(MVV) spectrum include the appearance of features at 44 eV (associated with Fe_3O_4) and at 52 eV (Fe_2O_3) (27-29). In the case of the clean Fe(111)(clock) surface, changes signifying the onset of Fe_3O_4 were observed after exposures of 10 L or less at 300 K, while exposures of 30 L or more were required to observe such changes at the S/Fe(111)(1×1) surface (12). Changes in the Al(LVV) spectra involve the shift of the main peak from 68 eV to 54.5 eV (30) as well as the onset of a feature at 38 eV. Thus, in the case of extensive oxidation of both aluminum and iron, there would be considerable overlap of the Auger signals in the region of 52-55 eV. The oxidation spectra shown here (Fig. 2.6), however, display relatively little change in the Fe(MVV) lineshape, indicating that the aluminum is preferentially oxidized regardless of the presence or absence of sulfur. This is in accord with previous studies (34) of aluminum deposition on Fe(100), which reported preferential oxidation of aluminum.

A comparison of Fig. 2.6a and b demonstrates that in the presence of sulfur, the oxidation of aluminum is significantly retarded. In the case of Al/S/Fe(111)(1×1) (Fig. 2.6b), an O_2 exposure of 3 L results in only minor changes to the shape of the Al^0 feature at 68 eV and little observable growth, if any, at features at 38 eV or 55 eV which would correspond to Al^{3+}. In contrast, Al/Fe(111)(clock) exposed to 3 L of O_2 (Fig. 2.6a) reveals significant changes, including a considerable loss in intensity of the 68 eV feature, the formation of a visible shoulder at 55 eV, and the onset of an indentation at 38 eV. At 10 L exposure, the sample with sulfur present (Fig. 2.6b) reveals that the features at 55 eV and at 38 eV have significant intensity, but so does the feature at 68 eV, indicating that substantial amounts of metallic aluminum still remain in the surface

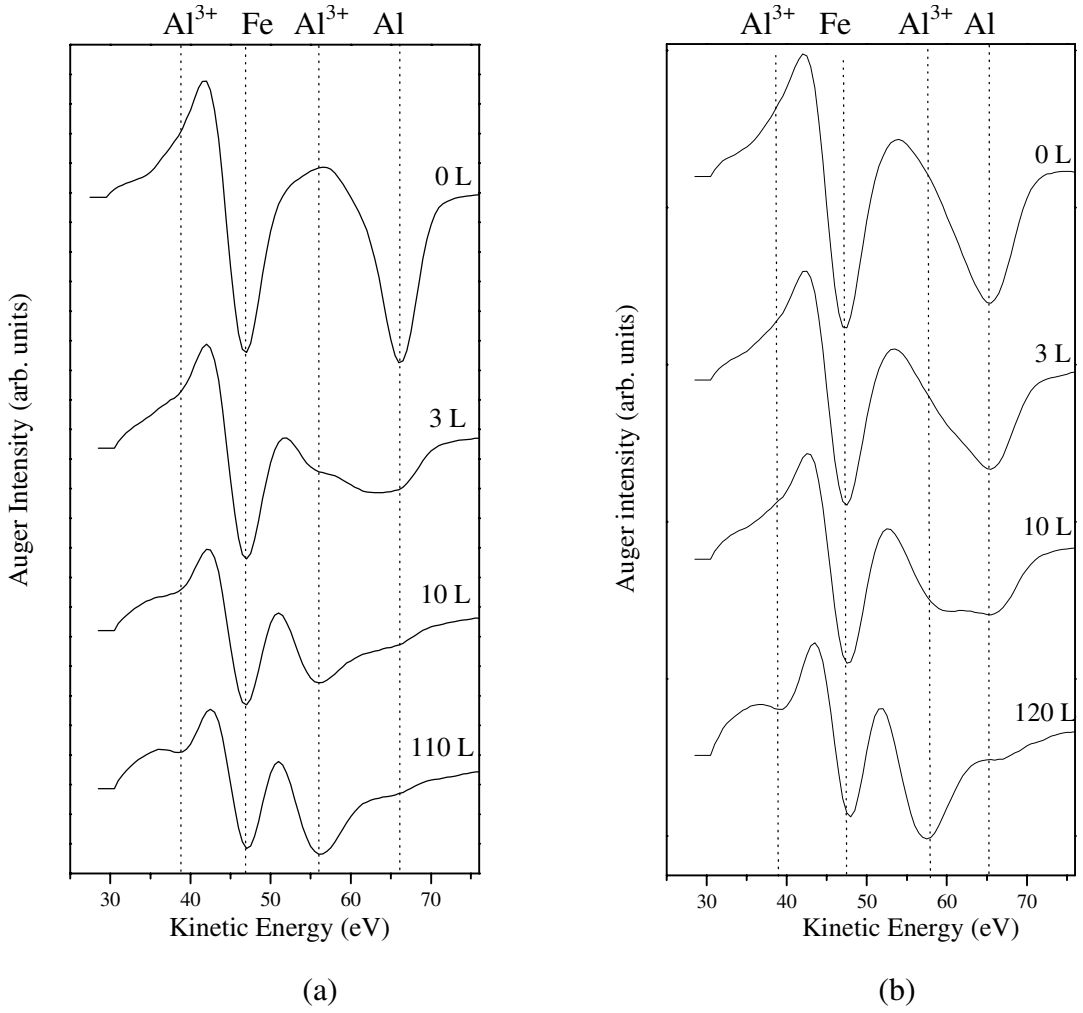

Fig. 2.6. Low energy Auger spectral region for oxidation of (a) Al/Fe(111)(clock) and (b) Al/S/Fe(111)(1×1).

region. The sulfur-free sample (Fig. 2.6a) shows very little metallic aluminum present after 10 L exposure. No significant further change in the sulfur-free sample is observed after a total exposure of 110 L (Fig. 2.6a), except for a slight growth in intensity of the 55 eV feature. The sulfur-containing sample after 120 L exposure (Fig. 2.6b) reveals a spectrum very similar to that observed for the sulfur-free sample after 110 L exposure (Fig. 2.6a). In both cases, such exposures have converted almost all the aluminum to

Al^{3+}. In order to determine whether the presence of sulfur was directly correlated with inhibited oxidation, two Al/S/Fe(111)(1×1) samples were compared. For the first sample (data shown in Fig. 2.6b), the S/Al atomic ratio was 0.5. For the second, the atomic ratio was 0.7. The Fe(MVV)/Al(LVV) Auger spectral region for each sample before and after exposure to 10 L O_2 is shown in Fig. 2.7. After 10 L exposure, the sample with the lower S/Al ratio (Fig. 2.7a) shows perceptible oxidation of the aluminum, as evidenced by the appearance of a feature at 55 eV with intensity roughly equal to that of the aluminum metal feature at 68 eV. In contrast, the sample with the higher S/Al ratio shows no perceptible oxidation. This demonstrates that an increasing relative concentration of sulfur to aluminum inhibits aluminum oxidation at 300 K.

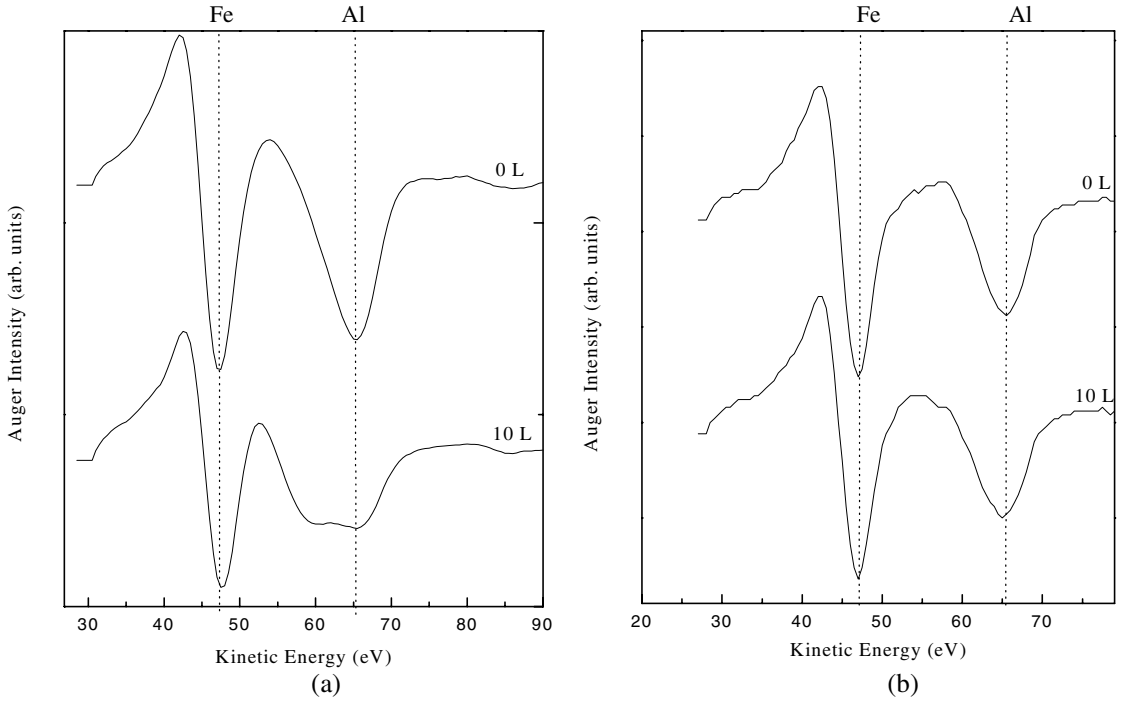

Fig. 2.7. Evolution of the low energy spectral region for Al/S/Fe(111): (a) S/Al atomic ratio = 0.5; (b) S/Al atomic ratio = 0.7.

Although the above data indicate that sulfur is not overgrown by deposited metallic aluminum, it is of pertinent interest to understand whether oxidation leads to aluminum oxide overgrowing the sulfur layer. The issue is complicated because a determination of the total Al Auger intensity (Al^0 and Al^{3+}) is problematic due to an overlap of spectral features in the region of 50 eV-70 eV. Fe(MVV) features are also affected, although apparently to a lesser degree than the aluminum-related features. Figure 2.8 displays changes in the O(KVV), S(LVV) and Fe(MVV) intensities,

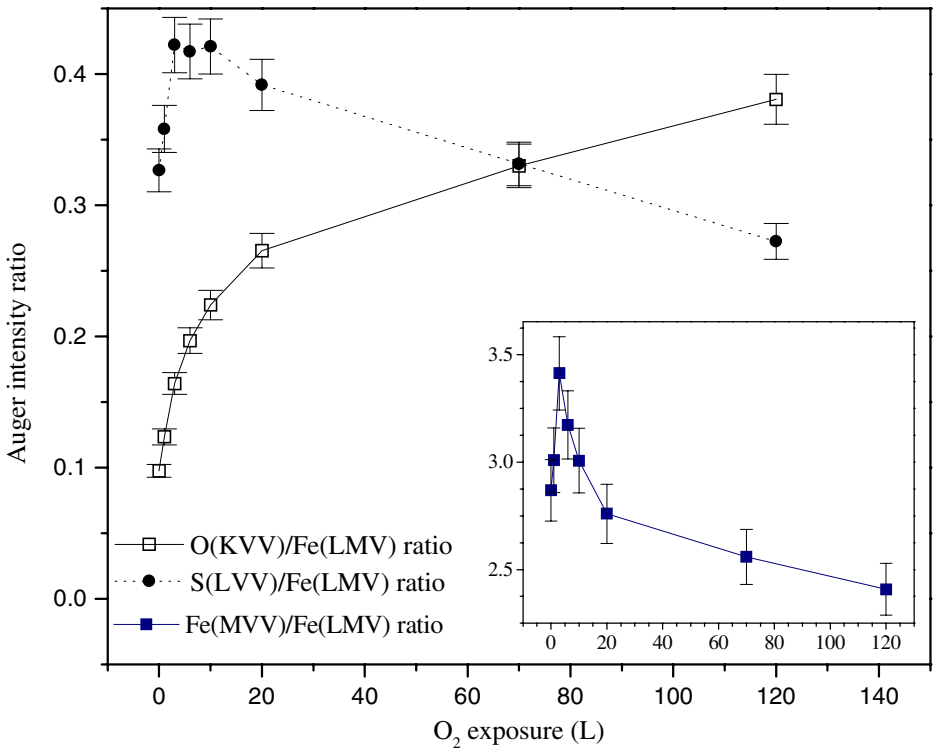

Fig. 2.8. O(KVV)/Fe(LMV), S(LVV)/Fe(LMV) and Fe(MVV)/Fe(LMV) Auger ratios vs. O_2 exposure at the surface of Al/S/Fe(111)(1×1) [sample the same as in Figs. 2.6 (b) and 2.7 (a)].

normalized to the Fe(LMV) intensity, which is unaffected by such spectral overlap. The relative oxygen intensity continues to increase rapidly for exposures up to 20 L, and then more slowly for exposures up to 120 L. The relative sulfur intensity also increases to 20 L, followed by a gradual decline for exposures up to 120 L. At 120 L, the relative sulfur Auger intensity is approximately that observed prior to oxidation.

If the sulfur remained at the surface of the growing alumina overlayer, then one would expect the relative sulfur intensity [i.e., relative to the Fe(LMV) intensity] to either remain constant or slowly increase, because of further attenuation of the underlying iron Auger signal. If the developing alumina overlayer were to uniformly overgrow the sulfur, then one would expect a monotonic decay of the S(LVV) signal intensity. As indicated by the data in Fig. 2.8, neither model provides an accurate description of what is occurring. The increase in S(LVV) intensity up to 20 L O_2 exposure suggests that initially the oxidation process results in further attenuation of the Fe(LMV) signal from the substrate without overgrowth of the sulfur adatoms. This might be due to initial alumina growth in sulfur-free areas, or the segregation of oxygen- and sulfur-covered domains, as has been observed on Fe(111) surfaces (17,35). Subsequent overgrowth of the sulfur at higher exposures could then account for the gradual decrease in relative sulfur intensity. However, whether the alumina forms in three-dimensional islands or conformal layers, and whether the sulfur segregates to the alumina-iron interface or remains on or within the alumina cannot be determined from the data.

2.4. Discussion

The data presented here indicate that the deposition of aluminum metal on a sulfur-modified Fe(111) surface at 300 K results in the formation of a sulfur-modified aluminum overlayer. The aluminum atoms are inserted between the sulfur and the iron substrate. This is confirmed by an increase of the sulfur Auger intensity during aluminum deposition, and by the inhibition of oxidation at 300 K for deposition onto S/Fe(111)(1×1). The Fe-S, Fe-O, Al-S and Al-O bond dissociation energies are listed in Table 2.1 (36). The S-Al bond is stronger than the S-Fe bond by 52 kJ mol^{-1}. Even allowing for the fact that sulfur-metal bonds at surfaces and interfaces may well have different charge densities than bonds in bulk ionic compounds (11,19), the data in Table 2.1 indicate a strong driving force for the abstraction of sulfur from the Fe(111) surface by deposited aluminum atoms. The LEED and STM data indicate that the aluminum overlayer, as modified by sulfur, is disordered at 300 K. Since a diffuse LEED pattern was also observed for aluminum deposition on sulfur-free Fe(111)(clock), it is apparent

Table 2.1. Bond enthalpies

Bond	Bond enthalpy (kJ mol^{-1})
Al-O	511
Al-Al	133
S-Fe	322
Fe-Al	133 ± 6
S-Al	374
Fe-O	390
Fe-Fe	100

that the aluminum deposition, rather than the presence of sulfur, results in disorder.

Given the insertion of aluminum atoms between sulfur and the iron substrate, the sulfur-induced inhibition of aluminum oxidation is not surprising. Similar effects have been observed for the oxidation of iron surfaces (17,32) and attributed to sulfur and oxygen competition for the same surface sites. The data do not give a decisive indication as to whether oxidation of the sulfur-modified aluminum adlayer leads to alumina overgrowth of the sulfur, or to a more complex picture, possibly involving conformational changes in the alumina overlayer. The data clearly indicate, however, that for O_2 exposures > 20 L, sulfur does not remain on top of a conformal alumina adlayer.

Previous studies (34) of aluminum deposition on Fe(100) suggest that at low aluminum coverage and deposition rates, alloying occurs at the Al-Fe(100) interface. Faster deposition rates apparently kinetically hinder alloying. Actual deposition rates in the experiments reported here suggest a deposition rate of approximately two aluminum monolayers (based on sulfur and aluminum Auger intensities) in 1200 sec. This is slightly slower than the "fast" deposition rate (2 aluminum monolayers/1000 sec) reported to kinetically hinder Fe-Al alloying (34). In any case, iron and aluminum Auger data previously reported (34) show distinct changes in the slope of the aluminum and iron uptake curves. No such breaks are apparent in the aluminum uptake curve for S/Fe(111)(1×1) (Fig. 2.2). Whether this departure from layer-by-layer growth is due specifically to the presence of sulfur, or to the differences in Fe(111) vs. Fe(100) growth modes cannot be discerned from these data.

2.5. Summary and Conclusions

In summary, aluminum deposition onto the sulfur-modified Fe(111)(1×1) surface results in the formation of a sulfur-modified aluminum overlayer. The overlayer is disordered at 300 K. Subsequent oxidation at 300 K is inhibited compared to oxidation of an aluminum overlayer deposited on a sulfur-free Fe(111) surface. The inhibition is more pronounced at higher S/Al atomic ratios. The increase of sulfur intensity and the oxygen uptake curves are consistent with sulfur at the surface of the aluminum overlayer.

The displacement of sulfur by aluminum has implications for the formation of alumina-metal interfaces during the oxidation of Fe-Al and Ni-Al alloys. In the absence of interfacial sulfur, the formation of adherent alumina scales has been demonstrated (3,5) under controlled conditions. The presence of sulfur at or near the alloy surface prior to the oxidation process might result in a significant alteration of the chemical composition of the interfacial region, and also affect the stability of the oxide at elevated temperatures. A careful investigation of the effects of sulfur on the thermal stability of oxides on binary and ternary aluminum-containing alloys would also aid in understanding the microscopic mechanism for their accelerated corrosion in the presence of sulfur. The results of such a study are presented and discussed in the following chapters.

2.6. Chapter References

(1) Seah, M. P. in *Practical Surface Analysis: Auger and X-ray Photoelectron Spectroscopy*; 2 ed.; Briggs, D. and Seah, M. P., Eds.; Wiley: New York, 1990; Vol. 1, p 311.

(2) Stott, F. H. *Rep. Prog. Phys.* **1987**, *50*, 861.

(3) Smialek, J. L. *Metall. Trans. A* **1991**, *22*, 739.

(4) Meier, G. H. *Mater. Corros.* **1996**, *47*, 595.

(5) Smialek, J. L.; Jayne, D. T.; Schaeffer, J. C.; Murphy, W. H. *Thin Solid Films* **1994**, *253*, 285.

(6) Hou, P. Y.; Wang, Z.; Prüßner, K.; Alexander, K. B.; Brown, I. G. in *3rd International Conference on Microscopy of Oxidation*; Hou, P. Y.; Wang, Z.; Prüßner, K.; Alexander, K. B.; Brown, I. G., Eds.; The Institute of Materials: Trinity Hall, Cambridge, UK, 1996, p 1.

(7) Kiely, J. D.; Yeh, T.; Bonnell, D. A. *Surf. Sci.* **1997**, *393*, L126.

(8) Hou, P. Y.; Stringer, J. *Oxid. Met.* **1992**, *38*, 323.

(9) Cabibil, H.; Kelber, J. A. *Surf. Sci.* **1995**, *329*, 101.

(10) Fox, P.; Lees, D. G.; Lorimer, G. W. *Oxid. Met.* **1991**, *36*, 491.

(11) Cabibil, H.; Kelber, J. A. *Surf. Sci.* **1997**, *373*, 257.

(12) Lin, J.-S.; Ekstrom, B.; Addepalli, S. G.; Cabibil, H.; Kelber, J. A. *Langmuir* **1998**, *14*, 4843.

(13) Whittle, D. P.; Stringer, J. *Phil. Trans. Roy. Soc. Lond. A* **1980**, *295*, 309.

(14) Funkenbusch, A. W.; Smeggil, J. G.; Bornstein, N. S. *Metall. Trans. A* **1985**, *16*, 1164.

(15) Hou, P. Y.; Stringer, J. *J. Phys. IV* **1993**, *3*, 231.

(16) Hong, S. Y.; Anderson, A. B.; Smialek, J. L. *Surf. Sci.* **1990**, *230*, 175.

(17) Arabczyk, W.; Baumann, T.; Müssig, H. J.; Storbeck, F.; Meisel, A. *Vacuum* **1990**, *41*, 79.

(18) Liu, J.; Lu, J. P.; Chu, P. W.; Blakely, J. M. *J. Vac. Sci. Technol.* **1992**, *10*, 2355.

(19) Panzner, G.; Egert, B. *Surf. Sci.* **1984**, *144*, 651.

(20) Lin, J.-S.; Cabibil, H.; Kelber, J. A. *Surf. Sci.* **1998**, *395*, 30.

(21) Lin, J.-S.; Cabibil, H.; Ekstrom, B.; Kelber, J. A. *Surf. Sci.* **1997**, *371*, 337.

(22) Riviere, J. C. in *Practical Surface Analysis: Auger and X-ray Photoelectron Spectroscopy*; 2 ed.; Briggs, D. and Seah, M. P., Eds.; Wiley: New York, 1979; Vol. 1, p 19.

(23) RBD Enterprises: Bend, OR 97702.

(24) Davis, L. E.; MacDonald, N. C.; Palmberg, P. W.; Raich, G. E.; Weber, R. E. *Handbook of Auger Electron Spectroscopy*; 2 ed.; Physical Electronics Industries, Inc.: Eden Prairie, 1979.

(25) Colaianni, M. L.; Chen, P. J.; Yates, J. T., Jr. *Surf. Sci.* **1990**, *238*, 13.

(26) Seah, M. P.; Dench, W. A. *Surf. Interface Anal.* **1979**, *1*, 2.

(27) Smentkowski, V. S.; Yates, J. T., Jr. *Surf. Sci.* **1990**, *232*, 113.

(28) Ertl, G.; Wandelt, K. *Surf. Sci.* **1975**, *50*, 479.

(29) Seo, M.; Lumsden, J. B.; Staehle, R. W. *Surf. Sci.* **1975**, *50*, 541.

(30) Homeny, J.; Buckley, M. M. *Materials Lett.* **1990**, *9*, 443.

(31) Chen, J. G.; Colaianni, M. L.; Weinberg, W. H.; J. T. Yates, Jr. *Surf. Sci.* **1992**, *279*, 223.

(32) Cabibil, H.; Lin, J.-S.; Kelber, J. A. *Surf. Sci.* **1997**, *382*, L645.

(33) Seah, M. P. in *Practical Surface Analysis: Auger and X-ray Photoelectron Spectroscopy*; 2 ed.; Briggs, D. and Seah, M. P., Eds.; Wiley: New York, 1990; Vol. 1, p 201.

(34) Schulze, R. K.; Taylor, T. N.; Paffett, M. T. *J. Vac. Sci. Technol.* **1994**, *12*, 3054.

(35) Arabczyk, W.; Narkiewicz, U.; Kalucki, K.; Friedenberg, E. *Appl. Surf. Sci.* **1993**, *72*, 45.

(36) Lide, D. R. *CRC Handbook of Chemistry and Physics*; 74 ed.; CRC Press: Boca Raton, 1994, p 9/123.

CHAPTER 3

SULFUR-INDUCED DESTABILIZATION OF ALUMINUM OXIDE AT THE Fe(poly)-S-Al_2O_3 INTERFACE

3.1. Introduction

We report the destabilization of alumina by interfacial sulfur at the alumina-sulfur-iron interface. The reduction occurs at temperatures above 400 K under UHV conditions, and is followed by diffusion of aluminum into the bulk Fe(poly) substrate. In the absence of interfacial sulfur, the alumina-iron interface is stable to 900 K. Sulfur has been directly implicated in oxide scale spallation during thermal cycling (1-4). Experimental studies of polycrystalline alloy/alumina (1,2,4) and single-crystal alumina/Ni(poly) surfaces (3) have shown that sulfur will segregate to an existing alumina-metal interface. The presence of sulfur at the metal-alumina interface sharply degrades the thermal stability of the metal-oxide interface, leading to spallation. The effects of sulfur are also observed in chromia-forming and ferrous oxide-forming systems (5-9). In addition to the above, we have shown (in Chapter 2) that the deposition of aluminum on S/Fe(111)(1×1) at 300 K in UHV results in the insertion of aluminum between the sulfur atoms and the iron substrate, which retards the oxidation of aluminum deposited on the sulfur-covered Fe(111) surface.

Although oxide spallation has been associated with the segregation of sulfur to the oxide-metal interface (2,4), enhanced interfacial roughening (10), and interfacial void formation (11), the exact mechanism for sulfur-induced spallation is still a matter of

controversy (1,4-8,12-16). It has been shown recently (8) that sulfur can induce dewetting of iron oxide from an iron metal substrate by chemical reduction of an interfacial FeO 'glue layer', coincident with formation of SO_2. The destruction of the interfacial glue layer results in dewetting of Fe_2O_3 from the sulfur-covered metal surface. We present here for the first time, evidence that the presence of sulfur at the alumina-Fe(poly) interface leads to the destabilization of the ultrathin aluminum oxide film (~2.3 Å thick) at elevated temperatures, accompanied by the formation of metallic aluminum.

3.2. Experimental

Experiments were carried out in a UHV chamber shown schematically in Fig. 3.1 (6). It is equipped with facilities for temperature-programmed desorption (TPD) using a quadrupole mass analyzer and for Auger electron spectroscopy. A nude ion gauge monitored the pressure in the chamber. A base pressure of 2×10^{-10} Torr after bakeout was maintained by turbomolecular and ion-titanium sublimation pumps. A type-K thermocouple junction that was spot-welded at the backside of the sample monitored the temperature. The iron sample (Alfa Aesar, 99.98% purity) was a polycrystalline foil with an area of ~ 1 cm^2 and a thickness of 0.5 mm. It was polished to mirror finish using 0.05-μm alumina paste. It was then attached to two tantalum leads that allowed for resistive heating. The sample was cleaned in UHV by repeated cycles of Ar^+ sputtering and annealing from 800 to 1000 K. Minor concentrations of carbon, nitrogen and sulfur were observed, but were removed by the sputter/annealing treatment. The sputter/anneal cycle was continued until no impurities were observed upon annealing in UHV.

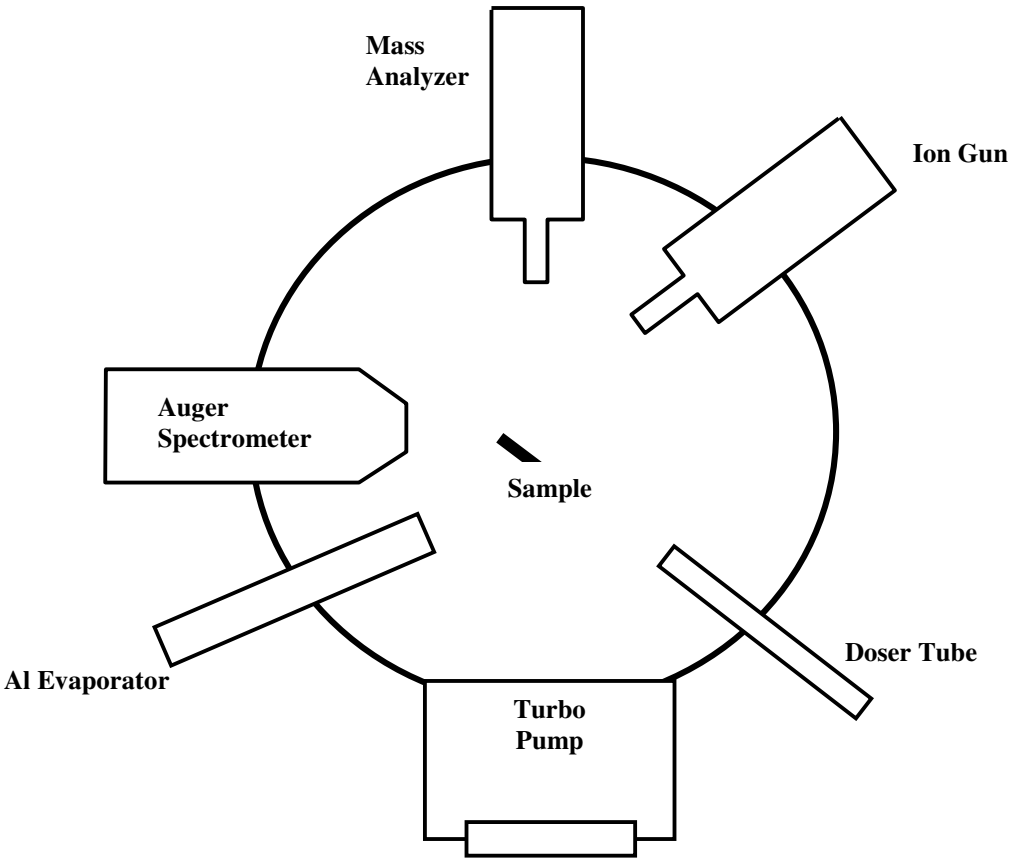

Fig. 3.1. Schematic of the AES/TDS system.

Evaporative deposition of aluminum was carried out with the use of a commercial UHV-evaporator (Focus GmbH) at constant power [32 Watts (W)] for varying times. Aluminum depositions are reported in terms of power × time (W-sec). Sulfur and oxygen dosing were carried out using electronic-grade H_2S and O_2 gases without further purification. The gases were admitted to the UHV chamber via manual leak valves and stainless steel doser tubes. Exposures were determined by monitoring background pressure and time of exposure [1 Langmuir (L) = 10^{-6} Torr-sec], and have not been corrected for the effects of ion-gauge sensitivity, flux to the sample or directional dosing.

Subsequent comparison of these data to those obtained in a different chamber by backfilling with oxygen indicate that the doser enhancement factor for oxygen in these experiments is ~ 100.

Auger spectra were collected in the derivative [dN(E)/d(E)] mode using a commercial cylindrical mirror analyzer with coaxial electron gun, a lock-in amplifier at 4V peak-to-peak modulation, and an XY recorder. The electron excitation energy was 3 keV. Relative concentrations of surface species were determined by using published Auger sensitivity factors (17) and intensities proportional to peak-to-peak signal height (pph) according to:

$$N_A/N_B = I_A X_B/I_B X_A \tag{3-1}$$

where N_A, I_A, and X_A represent the atomic concentration of element A, the peak-to-peak height (pph) and the atomic sensitivity factor, respectively. The fractional monolayer coverage of an adsorbate was calculated using equation (18)

$$\frac{\theta_A\{1-\exp[-a_A/\lambda_A(E_A)]\}}{(1-\theta_A)\{1-\exp[-a_A/\lambda_A(E_B)]\}} = \frac{N_A}{N_B} \tag{3-2}$$

In Eq. (3-2), θ_A is the fractional coverage, a_A is the atomic diameter and λ_A is the mean free path length of element A. Changes in the intensities of the Al(LMM), Al^{3+}(LMM), S(LMM), O(KVV), Fe(MVV), and Fe(LMV) transitions located, respectively, at 68 eV, 54 eV, 152 eV, 510 eV, 47 eV, and 651 eV were monitored. Because the Fe(LMV) transition is less readily attenuated, all the AES intensities are normalized relative to its intensity. The thickness of an attenuating overlayer was calculated using the mean free path length value of 4.4 Å (18) for the Fe(MVV) transition and the equation

$$I = I_0 e^{-d/\lambda} \tag{3-3}$$

where, I_0 is the intensity of the peak before overlayer deposition, and I is the intensity of the peak after deposition, d is the thickness of the attenuating overlayer, and λ is the inelastic mean free path of the element. The percentage attenuation in the Fe(MVV) and S(LMM) intensities can be calculated as follows:

$$\% \text{ Attenuation} = \left[\frac{I_0 - I}{I_0}\right] \times 100 \qquad (3\text{-}4)$$

Although Auger is commonly used to determine surface elemental composition, the energies of the Fe(MVV) (19-21) and Al(LMM) (22-24) transitions are sensitive to oxidation state, and this permits the use of Auger to monitor changes in the aluminum and iron oxidation states upon oxygen exposure or annealing. The oxidation of Al^0 to Al^{3+} is associated with a shift of the Al(LMM) transition (in derivative mode) from 68 eV to 54 eV (23). For metallic iron, the Fe(MVV) transition is at 47 eV. The Fe_3O_4 and Fe_2O_3 are associated with features at 44 eV and 52 eV (20), respectively. Therefore, while extensive oxidation of both aluminum and iron would result in considerable signal overlap, initial changes from the metallic state as a function of controlled oxidation can be used to determine the preferential oxidation of one element or the other.

3.3. Results

3.3.1. Aluminum Deposition on Clean and Sulfur-modified Fe(poly)

The AES uptake curve (aluminum Auger intensity vs. deposition time) for aluminum deposition was examined for the clean polycrystalline iron sample. Auger spectra were collected after exposing the iron sample to aluminum at room temperature. Changes in the Al(LMM)/Fe(LMV) intensity ratio as a function of aluminum deposition time are

displayed in Fig. 3.2. Because the inelastic mean free path of Fe(LMV) is relatively large (11.4 Å) (18), this transition is less readily attenuated. Hence, all the AES intensities are normalized relative to the intensity of the Fe(LMV) transition. The first sharp break in the uptake curve indicates the deposition of one monolayer of aluminum (25). Subsequent aluminum depositions were then calibrated using the uptake curve in Fig. 3.2.

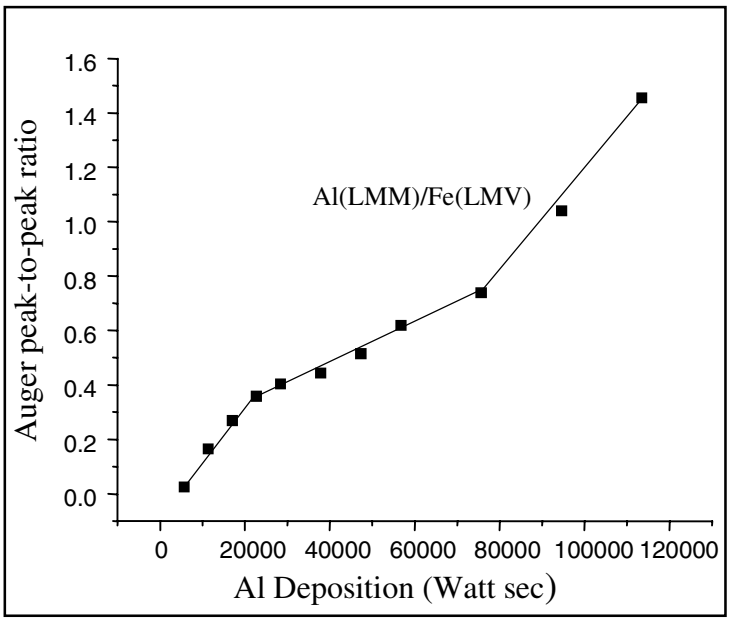

Fig. 3.2. Changes in the Al(LMM)/Fe(LMV) intensity ratio during the deposition of aluminum onto clean Fe(poly) sample at 300 K.

Figure 3.3 displays the Auger spectra of the (a) clean Fe(poly) sample, (b) the Fe-S interface, (c) the Fe-Al-S interface and (d) the Fe-S-Al_2O_3 interface. An adlayer of sulfur was prepared by exposing the clean polycrystalline iron sample (Fig. 3.3a) to H_2S at room temperature to obtain an S/Fe atomic ratio of ~ 0.4 (Fig. 3.3b). This atomic ratio is equivalent to a sulfur surface coverage of ~0.4 monolayer [Eqs. (3-1) and (3-2)]. Aluminum was then deposited onto the Fe-S surface. Aluminum deposition exposure

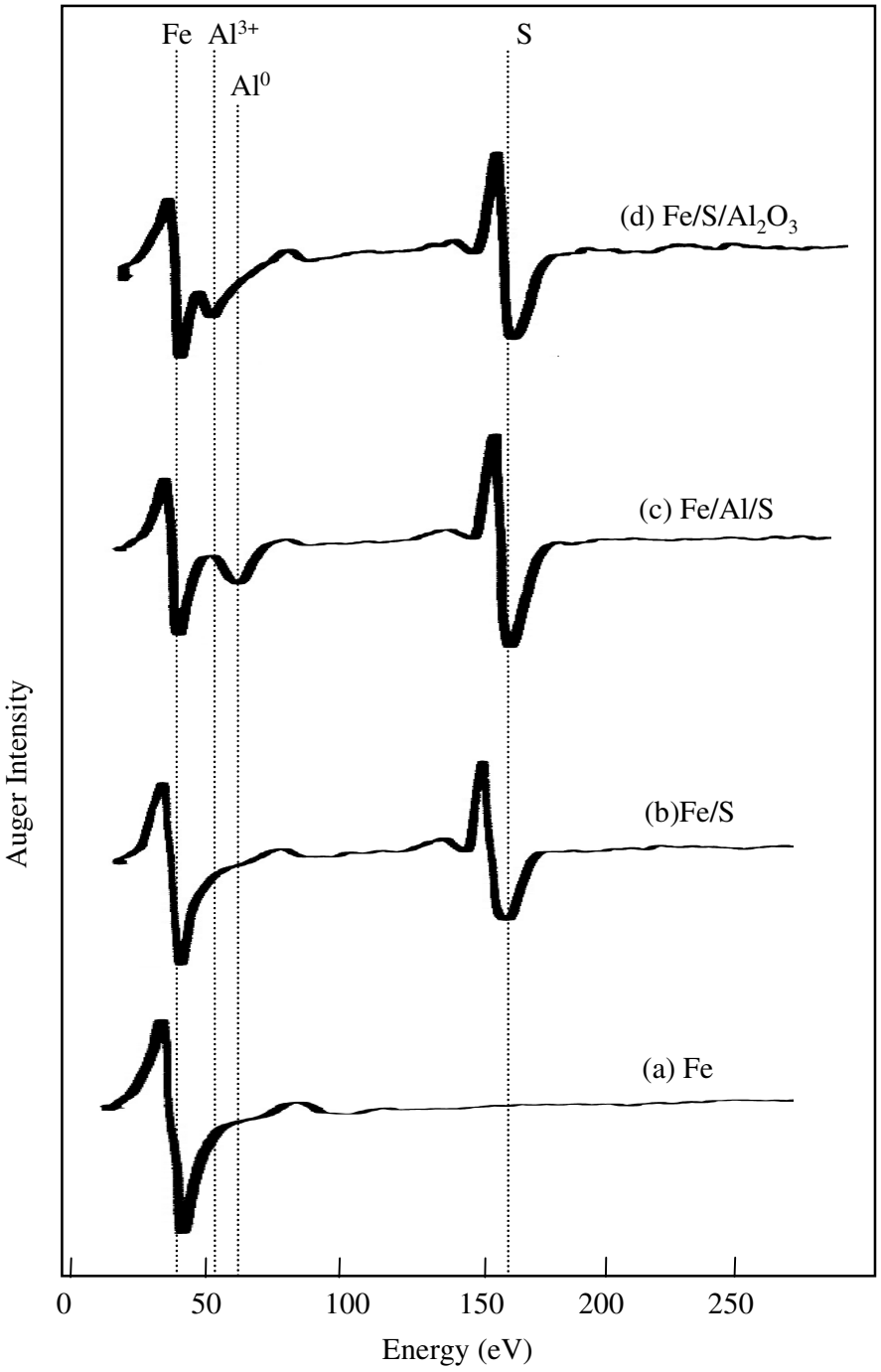

Fig. 3.3. Development of the Al^{3+} Auger signal (54 eV) upon oxidizing the metallic Al (68 eV) deposited at the Fe(poly)-S interface at 300 K. The Fe(MVV) at 47 eV and the S(LMM) at 152 eV do not shift during sample oxidation.

corresponding to ~ one monolayer of aluminum was obtained at ~ 20000 W-sec (Fig. 3.3c). The average overlayer thickness of the deposited aluminum was calculated [Eq. (3-3)] as 2.8 ± 0.2 Å. Since the atomic diameter of aluminum is 2.6 Å, this thickness is consistent with ~ one monolayer of deposited aluminum. Figure 3.3b and 3.3c show that upon depositing aluminum, the Fe(MVV) signal is further attenuated, while the relative intensity of the S(LMM) transition increases. The increase in the intensity of the sulfur signal and the decrease in the intensity of the Fe(MVV) signal indicate that aluminum is inserted between the iron and sulfur layers. This Al/S place exchange at the iron surface has already been reported in Chapter 2.

The resulting Fe-Al-S interface was exposed to O_2 at 300 K under UHV conditions (maximum O_2 pressure: 1×10^{-7} Torr). The Auger spectrum that was collected after O_2 exposure is shown in Fig. 3.3d. Oxygen exposure results in an increased attenuation of the Fe(MVV) signal, but no significant shifts in energy occurred that would indicate the presence of Fe_3O_4 (44 eV) and Fe_2O_3 (52 eV) (9,19-21). The Al(LMM) signal, on the other hand, shifts from 68 eV to 54 eV. The appearance of a peak at 54 eV, which is the spectral signature of Al^{3+}, indicates the formation of Al_2O_3 (23). Calculations using Eq. (3-1) yield an O/Al atomic ratio of 1.4, signifying essentially a highly stoichiometric aluminum oxide layer on the Fe-S surface.

One interesting feature of the spectra in Fig. 3.3 (c and d) is the attenuation of both the S(LMM) and Fe(MVV) signals upon the oxidation of aluminum. Changes in the intensities of these signals can provide a convenient way of determining whether or not sulfur is overgrown by aluminum oxide. Because the iron Auger signal is further

attenuated due to the growing alumina layer, one would observe an increased sulfur intensity relative to the Fe(LMV) signal had sulfur remained on the alumina surface. The fact that the relative sulfur intensity was attenuated by 28% upon oxidizing the Fe-Al-S interface indicates that sulfur was overgrown by aluminum oxide. With the use of Eqs. (3-3) and (3-4), one can show that the 40% attenuation of the Fe(MVV) signal [relative to Fe(LMV)] from spectrum (b) to spectrum (d) corresponds to an average overlayer thickness of 2.3 Å. If sulfur were overgrown by the same layer, its signal relative to that of Fe(LMV) should be attenuated by 24%, which is in close agreement with the actual attenuation of 28%. Hence, one can conclude that during the oxidation of aluminum, sulfur remains at the iron-aluminum oxide interface.

Another notable feature shown in Fig. 3.3 (spectra b and c) is the absence of a bifurcation at the high-energy end of the S(LMM) signal. Previous investigation of this Auger transition (26) revealed information on the chemical bonding between sulfur and iron surface atoms. The appearance and disappearance of a bifurcation at the higher energy end of the S(LMM) transition has been linked to the strength of the interaction between sulfur and iron atoms both in the presence or absence of an oxide overlayer, i.e., the presence of the bifurcation indicates a relatively stronger chemical bonding between sulfur and iron atoms. The same behavior was also observed for nickel and sulfur interactions (27). Hence, the absence of this bifurcation in the spectra shown in Fig. 3.3 is indicative of a weaker interaction between sulfur and the iron atoms in the polycrystalline sample under the present experimental conditions.

In the absence of sulfur, exposure of the Al-Fe interface to O_2 at 300 K results in oxidation of both aluminum and iron. The oxide resulting from the oxidation of

aluminum deposited on the clean Fe(poly) sample has an O/Al atomic ratio of 0.91, indicating that the intensity measured around 53 eV contains some contributions from Fe^{2+} (52 eV) and/or Fe^{3+} (44eV). The appearance of the Fe-ion Auger peaks indicates that iron is oxidized as well. In addition, a closer inspection of the Auger spectra (not shown) around this region shows a considerable broadening of the peak, which indicates an overlapping of several bands. A similar broadening has been reported in Chapter 2.

3.3.2. Annealing of Al_2O_3/S/Fe(poly) and Al_2O_3/Fe(poly)

The Fe-S-Al_2O_3 interface was annealed to successively higher temperatures in UHV. The sample was held at a given temperature for 5 minutes. Changes in the S(LMM) and Al(LMM) Auger intensities [relative to the Fe(LMV) intensity] are plotted versus the annealing temperature in Fig. 3.4. The relative aluminum intensity from the Fe-S-Al_2O_3 sample increases between 300 K and 400 K, then gradually decays as the temperature increases. The sulfur signal exhibits an exactly opposite behavior with respect to the aluminum. The sulfur signal initially decreases between 300 K and 400 K, followed by an increase in its intensity above 400 K. The increase in the aluminum intensity can be attributed to the spreading of the oxide layer across the surface, rendering a more uniform attenuation layer. Because the oxide covers a relatively larger area of the underlying metal substrate after heating it to 400 K, the iron signal experiences further attenuation in its intensity. Because sulfur remains at the Fe-Al_2O_3 interface, it experiences a reduction in its intensity as the oxide forms a more uniform layer at 400 K.

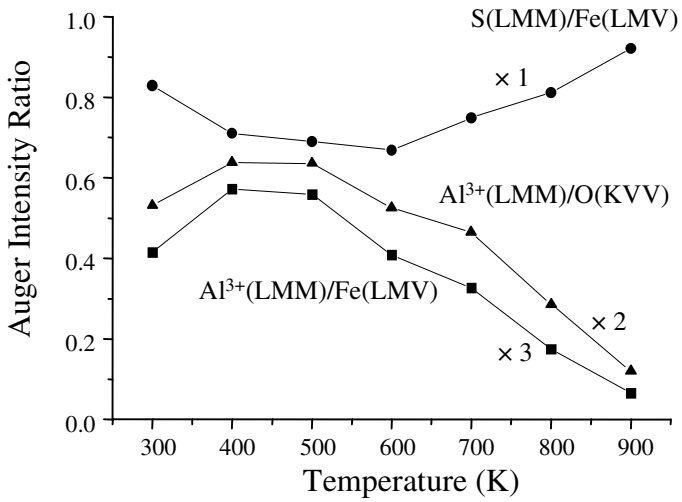

Fig. 3.4. Changes in the Al^{3+}(LMM)/Fe(LMV), S(LMM)/Fe(LMV) and Al^{3+}(LMM)/O(KVV) intensity ratios during the annealing of Fe-S-Al_2O_3 at elevated temperatures. The heating period is set for five minutes at a given temperature.

Figure 3.4 also shows that at temperatures above 400 K, the aluminum signal for the Fe-S-Al_2O_3 sample decreases significantly in intensity relative to the Fe(LMV) signal. The decrease in the aluminum intensity at elevated temperatures could conceivably result from any of the following: [1] the formation of three-dimensional oxide islands, [2] diffusion of Al_2O_3 into the bulk, and [3] the chemical reduction of the oxide and subsequent diffusion of metallic aluminum. Analysis of the Auger spectra cannot conclusively rule out dewetting of the oxide overlayer as responsible for the marked attenuation of the aluminum intensity. If the oxide simply coalesced into three-dimensional islands, then the relative atomic concentrations of aluminum atoms to oxygen atoms should remain constant, since the chemical composition of the metal oxide is not destroyed in the process. The longer mean free path (18) for the O(KVV)

transition (14.7 Å) relative to the Al(LMM) transition would cause preferential attenuation of the Al(LMM) signal during three-dimensional islanding (dewetting). Such data are also consistent with the chemical reduction of alumina to aluminum metal at the interface, followed by diffusion into the bulk (*vide infra*).

Diffusion of Al_2O_3, *per se*, into the bulk is ruled out on the basis of the results obtained for the sulfur-free Fe-Al_2O_3 sample. The changes in aluminum and oxygen Auger intensities with temperature are compared in Fig. 3.5 for Fe-S-Al_2O_3 and Fe-Al_2O_3. Because of the oxidation, in the absence of sulfur, of both aluminum and iron, which is characterized by a considerable overlap of the Auger signals in the region of 52-55 eV (where the Al^{3+} signal is located), the Al^{3+}/O intensity ratio cannot be calculated accurately. In the absence of sulfur, however, the ratio of the intensity of the peak

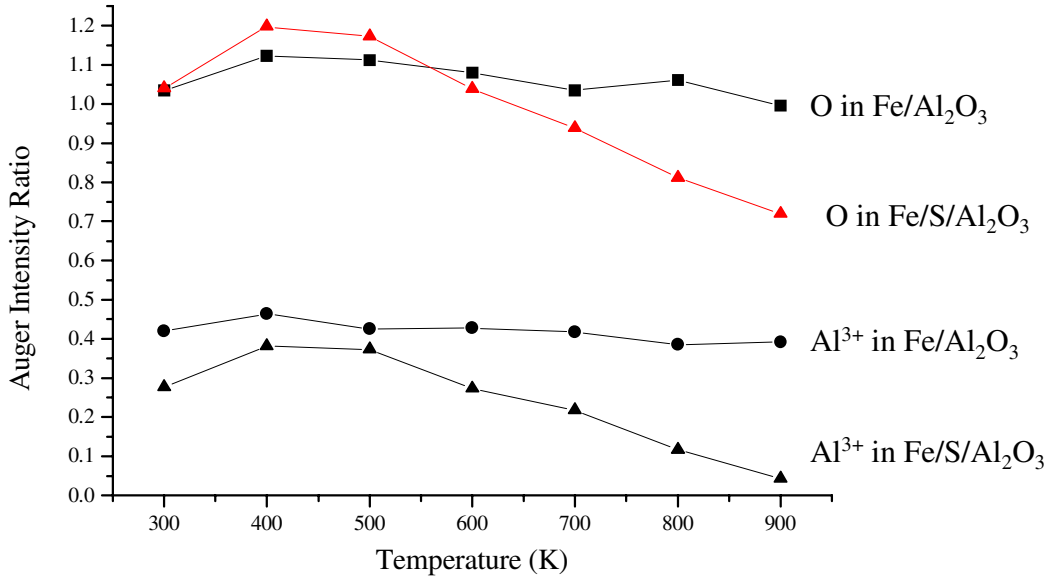

Fig. 3.5. Comparison of changes in Al^{3+} and oxygen Auger intensities with temperature for Fe-S-Al_2O_3 and Al_2O_3/Fe.

centered around 53 eV to the oxygen intensity for the Fe-Al_2O_3 is unchanged by the annealing process, indicating a stable oxide layer. This is consistent with previously reported studies (28) of the iron deposited on Al_2O_3 in which neither interfacial reaction nor diffusion was observed below 900 K. These data indicate that, in the absence of sulfur, the oxide layer (i.e., aluminum and iron oxides) on the Fe(poly) sample is highly stable during the annealing process up to ~ 900 K.

Evidence for the formation of Al^0 at the Fe-S-Al_2O_3 interface upon annealing is shown in Fig. 3.6. The formation of metallic aluminum is indicated by the appearance of a small feature at 68 eV (23) (Fig. 3.6a). The appearance of the 68 eV transition cannot be attributed to changes in iron or sulfur oxidation states (9,19-21,26). Figure 3.6a shows the evolution of the Al^0 signal as the Fe-S-Al_2O_3 sample temperature is held at 600 K from 5 to 30 minutes. The Auger signal at 68 eV begins to appear upon heating the sample at 600 K for 15 minutes. This signal continues to develop up to a heating period of 30 minutes. The development of an Auger signal at around 68 eV is indicative of the formation of metallic aluminum.

Conversion of Al^{3+} into Al^0 as the Fe-S-Al_2O_3 sample is annealed progressively from 300 K to 800 K is also evident in Fig. 3.6b. A decrease in the intensity of the Al^{3+} signal is accompanied by an increase in the Al^0 intensity when the sample is heated from 300 K to 700 K. A slight decrease in the Al^0 intensity as the sample temperature reaches 800 K is observed in Fig. 3.6b. The appearance of the Al^0 Auger peak in the spectra presented in Fig. 3.6 clearly indicates that chemical reduction of aluminum oxide occurs

in the presence of sulfur at the Fe-Al_2O_3 interface during annealing at elevated temperatures.

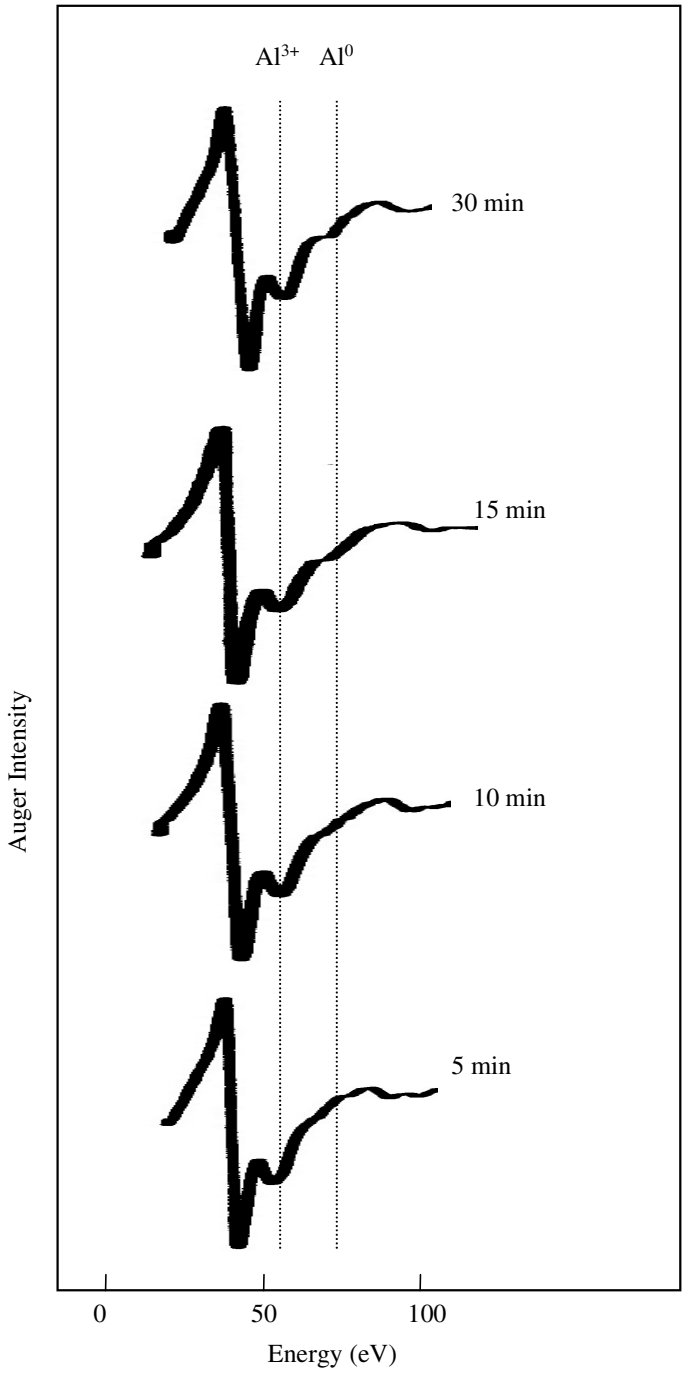

Fig. 3.6 (a). Evolution of the Al^0 Auger signal as the Fe(poly)-S-Al_2O_3 sample is annealed at successively longer periods at 600 K.

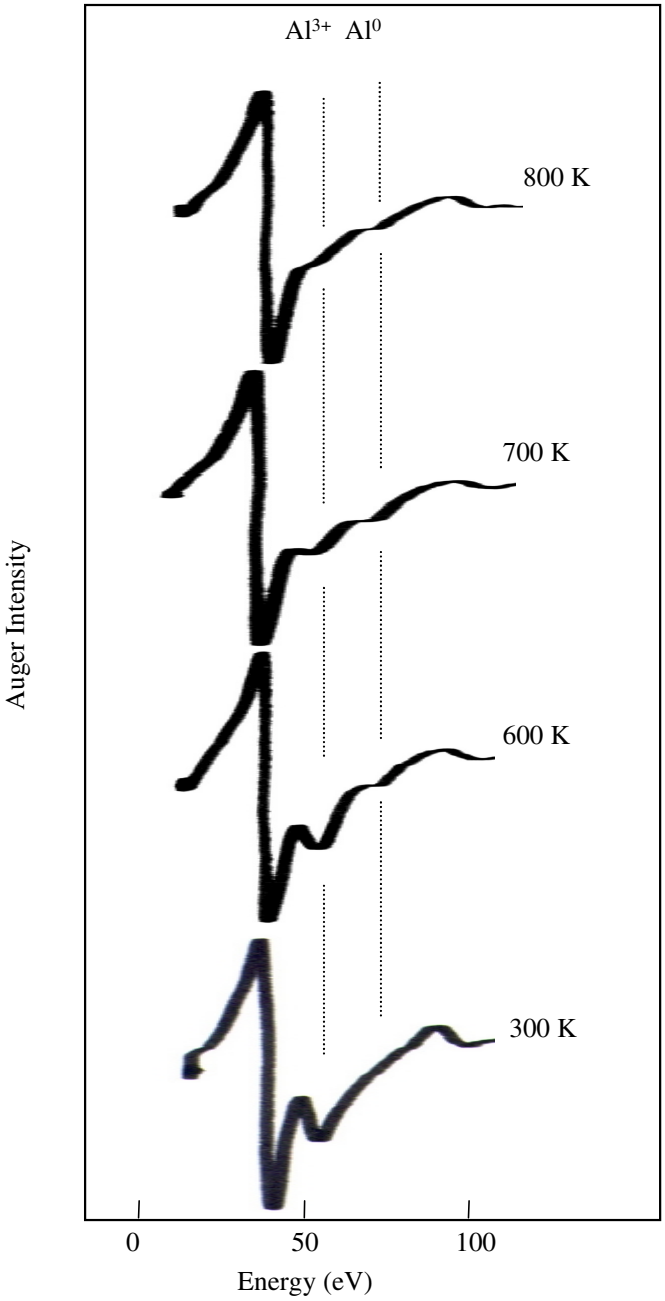

Fig. 3.6 (b) Growth of the Al^0 Auger signal and the attenuation of the Al^{3+} signal as the Fe(poly)-S-Al_2O_3 sample is annealed progressively to higher temperatures. The heating period is set for 30 minutes at a given temperature.

In Fig. 3.6 a,b, one can also observe the absence of a 1:1 correspondence between the attenuation of the Al^{3+} signal and the growth of the Al^0 signal. Annealing for longer times at 600 K (Fig. 3.6a) does not result in a progressive increase in the Al^0 intensity. Similarly, annealing to progressively higher temperatures (Fig. 3.6b) results in a decrease in the Al^{3+} intensity at 54 eV, but without a corresponding increase in the intensity of the Al^0 feature (68 eV). At 800 K, for example (Fig. 3.6b), the Al^{3+} signal disappears almost completely from the spectra, yet the Al^0 signal intensity does not increase upon heating the sample from 700 K to 800 K. The data indicate that the decrease in the Al^{3+} signal intensity (54 eV) is *not* accompanied by a corresponding increase in the Al^0 signal intensity (68 eV). The data in Figs. 3.4 and 3.6 therefore indicate that the $Al^{3+} \rightarrow Al^0$ chemical reduction is accompanied by the removal of aluminum from the interfacial region.

The transport of aluminum from the interface could arise either from aluminum diffusion or aluminum desorption. In order to determine the thermal behavior of metallic aluminum at the Fe-S interface, a Fe-Al-S sample (no oxidation) was annealed progressively to higher temperatures between 300 K and 800 K. Changes in the intensities of the Al(LMM) and S(LMM) relative to the Fe(LMV) as functions of annealing temperature are given in Fig. 3.7. At higher temperatures, the aluminum intensity relative to Fe(LMV) decreases as the aluminum metal leaves the surface. Since the vapor pressure of aluminum at 800 K is below 10^{-11} Torr (29), sublimation is negligible. A previous study (30) involving low-energy ion-scattering spectroscopy (LEISS) and AES measurements reported a similar behavior in which aluminum

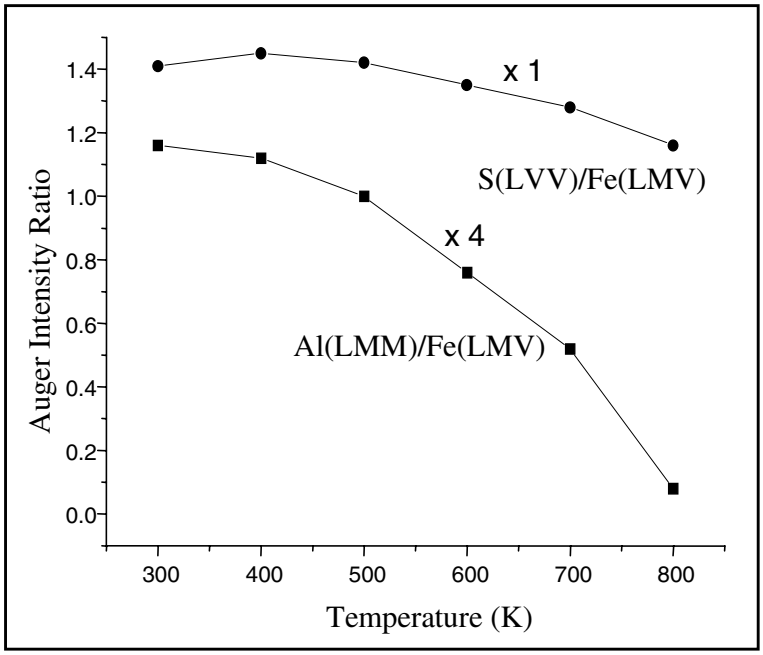

Fig. 3.7. Changes in the Al(LMM) intensity relative to the Fe(LMV) intensity as the Fe(poly)-Al-S is annealed from 300 K to 800 K.

deposited on clean Fe(100) surfaces diffuses into the bulk, and forms stoichiometric alloys with iron. The presence of sulfur does not appear to affect the alloying behavior of aluminum metal. Because the Fe(LMV) becomes less attenuated as aluminum diffuses into the bulk, one would expect the relative sulfur intensity to gradually decrease if the sulfur remains on the surface. Figure 3.7 does show a slight downward trend in the intensity of S(LMM) relative to Fe(LMV), indicating that sulfur remains on the surface upon diffusion of aluminum into the bulk. The diffusion of aluminum metal into the bulk is consistent with the fact that the intensity of the Al^0 signal does not continue to increase even as the Al^{3+} signal decreases in intensity when the Fe-S-Al_2O_3 sample is heated to

800 K. The concentration of metallic aluminum at the interface apparently reaches a steady state during the annealing process.

In view of the formation of SO_2 reported (6,8) at iron oxide-sulfur-iron metal interfaces, preliminary attempts were made to observe the evolution of SO_2 or other sulfur-containing species (e.g., S_2) by temperature programmed desorption. No such reaction products were observed.

3.4. Discussion

The Auger spectra presented here (Figs. 3.4-3.6) indicate that an aluminum oxide overlayer on Fe(poly) is destabilized by the presence of interfacial sulfur at temperatures above 600 K in UHV conditions. The data in Fig. 3.4 indicate that this instability is marked by a sharp decrease in aluminum surface coverage. The data in Fig. 3.5 demonstrate that this instability is due specifically to the presence of interfacial sulfur, in agreement with previously published reports (28) of the stability of the (sulfur-free) Al_2O_3-Fe interface to 900 K in UHV. The data also indicate that the destabilization of the oxide overlayer is accompanied by the formation of some Al^0, as indicated by the onset of a feature at 68 eV in the Al(LMM) spectra above 600 K (Fig. 3.6 a and b). The failure to observe Al^0 formation in the absence of interfacial sulfur indicates that the appearance of metallic aluminum is specifically associated with the presence of interfacial sulfur, rather than to extraneous effects, such as electron-stimulated reduction of the oxide during the acquisition of Auger spectra. The intensity of the Auger feature corresponding to the formation of Al^0 (68 eV, Fig. 3.6) does not increase monotonically, however, with the decrease in Al^{3+} intensity (54 eV, Fig. 3.6). Since the vapor pressure

of aluminum at or below 800 K is negligible, the desorption of aluminum from the surface is ruled out. The data therefore indicate one of two possibilities:

(a) The instability is due to the formation of three-dimensional aluminum oxide islands on the Fe(poly) substrate, together with the reduction of some Al^{3+} to Al^0, or

(b) Al^{3+} is reduced to Al^0 by interfacial sulfur, and this is followed by diffusion of metallic aluminum into the bulk Fe(poly) substrate.

Either of the above possibilities would of necessity involve the sulfur-induced scission of some aluminum-oxygen bonds. Such a step is hard to justify on the basis of standard bond dissociation enthalpies (31) (Table 3.1). For example, a simple O/S exchange reaction at the Al-O/Fe-S interface would be endothermic:

$$\text{Al-O} + \text{Fe-S} \rightarrow \text{Al-S} + \text{Fe-O} \qquad \Delta H = 69 \text{ kJ mol}^{-1} \qquad (3\text{-}5)$$

SO_2 formation would provide an additional driving force for reaction (3-5), but no such

Table 3.1. Bond Enthalpies

Bond	Bond Enthalpy (kJ mol^{-1})
Al- O	511
Al-Al	133
S-Fe	322
Fe-Al	133 ± 6
S-Al	374
Fe-O	390
Fe-Fe	100

reaction product has yet been observed. The above reaction step would, however, account for the formation of Al^0, since the formation of an Al-S-Fe interface in the absence of oxygen results in a metallic Al(LMM) spectrum (Fig. 3.3).

A partial explanation for the formation of metallic aluminum in the presence of interfacial sulfur is that the iron-sulfur bond at a surface or interface is substantially different in electronic structure and reactivity than that found for bulk FeS. XPS (26) and work function measurements (32,33) demonstrate that Fe-S (26,32) and Ni-S (33) chemical bonds are essentially covalent. This may be due to the enhanced screening of metal-sulfur charge separation in the presence of a metallic substrate compared to an ionic bulk sulfide phase. A loss of partial ionic character would be expected to result in enhanced reactivity (34). That this is indeed the case is demonstrated by the observed (6,8) interfacial sulfur attack on iron-oxygen bonds at the Fe/S/Fe-O interface, despite the fact that the observed reaction is thermodynamically unfavorable on the basis of free energies of bulk phases. There is therefore ample evidence that iron-sulfur bonds at surfaces or interfaces display enhanced reactivity compared to bulk sulfide phases. A greatly reduced Fe-S dissociation enthalpy would make reaction (3-5) thermodynamically favorable.

In addition to enhanced Fe-S reactivity, another likely driving force for the destabilization of the alumina overlayer is the diffusion of metallic aluminum into the iron bulk. Studies of aluminum deposited onto iron under UHV conditions (30) in the absence of sulfur indicate substantial Al-Fe alloy formation even at 300 K. That metalllic aluminum will diffuse into bulk iron at temperatures above 600 K, even in the presence

of interfacial sulfur, is demonstrated by the results in Fig. 3.7. Therefore, once metallic aluminum is produced at the interface, diffusion of the metallic aluminum into the iron substrate occurs at elevated temperatures. Therefore, alternative (b) - the sulfur induced reduction of alumina to aluminum, followed by diffusion of metallic aluminum into the bulk - is more likely, since metallic aluminum should not be stable on the iron surface above 600 K.

If diffusion of metallic aluminum into iron is indeed a significant driving force for the above phenomenon, one would expect alumina overlayers to remain stable in the presence of interfacial sulfur, *provided that the substrate is a high aluminum content alloy*. The presence of metallic aluminum in the substrate would inhibit the diffusion of additional metallic aluminum from the interface to the bulk. In order to verify this hypothesis, similar studies were performed on Al_2O_3 films grown on $Ni_3Al(111)$ samples. The results of these investigations are presented in the following chapters (Chapters 4-6).

3.5. Summary and Conclusions

The thermal stability of Al_2O_3 on a polycrystalline iron sample in the presence of sulfur was studied by Auger electron spectroscopy. Aluminum was deposited at 300 K under UHV conditions onto a polycrystalline iron substrate modified by adsorbed sulfur. Subsequent exposure to O_2 at 300 K under UHV conditions resulted in the formation of aluminum oxide on top of the S/Fe surface, with negligible oxidation of iron. In contrast, a similar treatment of the Al-Fe interface in the absence of sulfur resulted in some iron as well as aluminum oxidation. When the resulting Fe-S-Al_2O_3 interface was annealed from 300 K to 800 K, Auger electron measurements revealed the formation of Al^0. The

concentration of metallic aluminum remained limited even as the concentration of Al^{3+} continued to decrease upon annealing. In the absence of sulfur, the oxidized Al-Fe interface remained stable until ~900 K, in agreement with other work (28).

The above data demonstrate that interfacial sulfur destabilizes an Al_2O_3 overlayer on Fe(poly) at temperatures above 600 K. This instability is marked by a significant reduction in aluminum surface coverage, and the formation of some Al^0. No such effects are observed if sulfur is not present at the interface. Whether these effects are due to dewetting of the alumina overlayer from the iron substrate and the formation of Al_2O_3 islands, or indicate the reduction of Al^{3+} to Al^0 at the interface, followed by Al^0 diffusion into the bulk, cannot be discerned from the present data. Either possibility, however, must involve sulfur-induced attack of some aluminum-oxygen bonds at the interface, which is highly endothermic on the basis of the bond dissociation enthalpies derived from bulk phases. These results demonstrate the enhanced reactivity of iron-sulfur bonds at an interface compared to a bulk phase, similar to what has been previously observed (6,8) at Fe oxide-sulfur-Fe interfaces.

3.6. Chapter References

(1) Smialek, J. L. *Metall. Trans. A* **1991**, *22*, 739.

(2) Smialek, J. L.; Jayne, D. T.; Schaeffer, J. C.; Murphy, W. H. *Thin Solid Films* **1994**, *253*, 285.

(3) Kiely, J. D.; Yeh, T.; Bonnell, D. A. *Surf. Sci.* **1997**, *393*, L126.

(4) Hou, P. Y.; Wang, Z.; Prüßner, K.; Alexander, K. B.; Brown, I. G. in *3rd International Conference on Microscopy of Oxidation*; Hou, P. Y., Wang, Z., Prüßner, K., Alexander, K. B. and Brown, I. G., Eds.; The Institute of Materials: Trinity Hall, Cambridge, UK, 1996, p 1.

(5) Hou, P. Y.; Stringer, J. *Oxid. Met.* **1992**, *38*, 323.

(6) Cabibil, H.; Kelber, J. A. *Surf. Sci.* **1995**, *329*, 101.

(7) Fox, P.; Lees, D. G.; Lorimer, G. W. *Oxid. Met.* **1991**, *36*, 491.

(8) Kelber, J. A.; Addepalli, S. G.; Lin, J.-S.; Cabibil, H. in *High Temperature Corrosion and Materials Chemistry*; Hou, P. Y., McNallan, M. J., Oltra, R., Opila, E. J. and Shores, D. A., Eds.; The Electrochemical Society, Inc.: San Diego, CA, 1998; Vol. 98-99, p 190.

(9) Lin, J.-S.; Ekstrom, B.; Addepalli, S. G.; Cabibil, H.; Kelber, J. A. *Langmuir* **1998**, *14*, 4843.

(10) Walker, C. G.; El Gomati, M. M. *Appl. Surf. Sci.* **1988-89**, *35*, 164.

(11) Grabke, H. J.; Wiemer, D.; Viefhaus, H. *Fresenius J. Anal. Chem.* **1991**, *341*, 402.

(12) Stott, F. H. *Rep. Prog. Phys.* **1987**, *50*, 861.

(13) Funkenbusch, A. W.; Smeggil, J. G.; Bornstein, N. S. *Metall. Trans. A* **1985**, *16*, 1164.

(14) Hou, P. Y.; Stringer, J. *J. Phys. IV* **1993**, *3*, 231.

(15) Hong, S. Y.; Anderson, A. B.; Smialek, J. L. *Surf. Sci.* **1990**, *230*, 175.

(16) Arabczyk, W.; Baumann, T.; Müssig, H. J.; Storbeck, F.; Meisel, A. *Vacuum* **1990**, *41*, 79.

(17) Davis, L. E.; MacDonald, N. C.; Palmberg, P. W.; Raich, G. E.; Weber, R. E. *Handbook of Auger Electron Spectroscopy*; 2 ed.; Physical Electronics Industries, Inc.: Eden Prairie, 1979.

(18) Seah, M. P. in *Practical Surface Analysis: Auger and X-ray Photoelectron Spectroscopy*; 2 ed.; Briggs, D. and Seah, M. P., Eds.; Wiley: New York, 1990; Vol. 1, p 201.

(19) Smentkowski, V. S.; Yates, J. T., Jr. *Surf. Sci.* **1990**, *232*, 113.

(20) Ertl, G.; Wandelt, K. *Surf. Sci.* **1975**, *50*, 479.

(21) Seo, M.; Lumsden, J. B.; Staehle, R. W. *Surf. Sci.* **1975**, *50*, 541.

(22) Michael, R.; Gastaldi, J.; Allasia, C.; Jourdan, C.; Derren, J. *Surf. Sci.* **1980**, *95*, 309.

(23) Chen, J. G.; Crowell, J. E.; Yates, J. T., Jr. *Phys. Rev. B* **1986**, *33*, 1436.

(24) Homeny, J.; Buckley, M. M. *Materials Lett.* **1990**, *9*, 443.

(25) Argile, C.; Rhead, G. E. *Surf. Sci. Rep.* **1989**, 272.

(26) Panzner, G.; Egert, B. *Surf. Sci.* **1984**, *144*, 651.

(27) Windawi, H.; Katzer, J. R. *J. Vac. Sci. Technol.* **1979**, *16*, 497.

(28) Colaianni, M. L.; Chen, P. J.; Yates, J. T., Jr. *Surf. Sci.* **1990**, *238*, 13.

(29) O'Hanlon, J. F. *A User's Guide to Vacuum Technology*; 2 ed.; John Wiley & Sons: New York, 1989.

(30) Schulze, R. K.; Taylor, T. N.; Paffett, M. T. *J. Vac. Sci. Technol.* **1994**, *12*, 3054.

(31) Lide, D. R. *CRC Handbook of Chemistry and Physics*; 74 ed.; CRC Press: Boca Raton, 1994, p 9/123.

(32) Arabczyk, W.; Müssig, H.-J.; Storbeck, F. *Phys. Status Solidi A* **1979**, *55*, 437.

(33) Hardegree, E. L.; Ho, P.; White, J. M. *Surf. Sci.* **1986**, *165*, 488.

(34) Pauling, L. *The Nature of the Chemical Bond*; 3 ed.; Cornell University Press: Ithaca, New York, 1960.

CHAPTER 4

STM ATOMIC SCALE CHARACTERIZATION OF THE γ'-Al_2O_3 FILM ON $Ni_3Al(111)$

4.1. Introduction

Aluminum oxide is an important ceramic material because of its various technological applications (1). It exists in several phases with different crystal structures (2), the most notable of which are α-Al_2O_3 (sapphire), and the γ-Al_2O_3 phase that is used as a support for transition metal catalysts. Owing to the technological significance of alumina, numerous studies have been carried out to understand its electronic and structural properties (2-8). Bulk alumina or other oxide samples cannot be easily investigated by STM or conventional electron spectroscopic methods because they are insulating and produce charging effects. This drawback, however, can be overcome by employing thin films of metal oxides (6). Experimental studies have demonstrated that oxide films which are several monolayers thick simulate bulk-terminated samples in many respects (6).

Single-crystal samples of Ni-Al alloys have been used as substrates for the formation of thin Al_2O_3 films (5,7-10). X-ray photoelectron spectroscopy (XPS) studies (7,11,12) on Ni_3Al samples in UHV have demonstrated that aluminum oxide is the only oxidation product at O_2 partial pressures $< 10^{-6}$ Torr at T = 573-973 K. Well-ordered, 5 Å thick γ'-Al_2O_3 films have been prepared at 700-1200 K on $Ni_3Al(111)$ (7,8), $Ni_3Al(100)$ (7), NiAl(111) (10), and NiAl(110) (5,13-17) substrates. These films have

been characterized by various electron spectroscopic and microscopic techniques including high-resolution electron energy-loss spectroscopy (HREELS) (8,10), LEED (5,7,8,10) and transmission electron microscopy (TEM) (13). The above measurements point towards oxygen termination of the γ'-Al_2O_3 film. Recent HREELS and LEED studies (8) have proposed a two-domain structure for the γ'-Al_2O_3 film formed on $Ni_3Al(111)$. *Ab initio* calculations (3) performed on 5 Å thick $Al_2O_3(001)$ films simulated on Al(111) and Mo(110) substrates have demonstrated that the tetrahedrally coordinated Al^{3+} ions are located nearly in the same plane as the oxygen ions for electroneutrality. Since the radius of the O^{2-} ions (= 1.40 Å) is much larger than the radius of the Al^{3+} ions (= 0.53 Å), one expects the surface spectroscopy and reactivity of the oxide to be dominated by the oxygen anions (18).

STM studies of epitaxial Al_2O_3 films grown on NiAl(110) (15) have reported the coexistence of two domains of the oxide, in accordance with the LEED pattern. One of the domains was found to be incommensurate with the substrate (15). The incommensurability was attributed to weaker oxide-substrate interactions compared to the lateral interactions within the oxide (5). Cotterill et al. (19) proposed a model in which oxygen atoms are chemisorbed on a quasi-hexagonal Al(111) layer on top of a 100% nickel layer on $Ni_3Al(110)$. STM studies of the oxidation of NiAl(001) (9,20) have observed the formation of Al-O clusters at room temperature. Annealing the amorphous Al_2O_3 phase to 1300 K yields a crystalline θ-Al_2O_3 phase that exhibits an anisotropic island growth and roughness on a nanoscopic scale (9,20). No reports, however, are available to date on the STM atomic scale characterization of the γ'-Al_2O_3 film formed on $Ni_3Al(111)$. The results presented in this chapter corroborate earlier electron

spectroscopic findings on the oxidation of $Ni_3Al(111)$ (7,8,21). In addition, these results provide substantial evidence in support of the proposed structure of an ultrathin film of Al_2O_3 based on theoretical calculations performed by Jennison et al. (3).

In the present chapter, STM, LEED and AES results are reported for the clean and oxidized $Ni_3Al(111)$ in UHV. The clean $Ni_3Al(111)$ surface exhibits a bulk-like (2×2) configuration of aluminum atoms, in agreement with previous results (8,22). At room temperature, the oxide formed by saturation exposure to O_2 is amorphous. Phase transitions are observed in the temperature range of 300-1100 K, consistent with earlier studies (2). AES measurements during thermal treatment of the oxide in the temperature range from 300 K to 1100 K demonstrate aluminum enrichment and provide evidence for the formation of an aluminum-rich layer at the γ'-Al_2O_3-$Ni_3Al(111)$ interface. The γ'-alumina film formed after annealing to ~ 1100 K possesses a hexagonal symmetry as determined by LEED. The LEED pattern demonstrates the ordering of O^{2-} ions with a lattice dimension of 2.9 ± 0.1 Å. STM atomic-resolution imaging (discussed below) reveals a hexagonal arrangement of protrusions [assigned to the aluminum atoms at the Al_2O_3-$Ni_3Al(111)$ interface], with an average interatomic spacing of 3.0 ± 0.1 Å.

4.2. Experimental

Experiments were carried out in an Omicron UHV-STM system described in Section 2.2 (23). The base pressure of the experimental chamber is 5×10^{-11} Torr after bake-out. The chamber is equipped with facilities for AES, reverse-view LEED and STM, as well as sample cleaning and gas dosing, and is pumped by a 60 l s^{-1} turbomolecular pump, and ion- and titanium-sublimation pumps.

AES measurements were performed using a cylindrical mirror analyzer with a coaxial electron gun (Physical Electronics). Auger data were collected with an excitation beam energy of 3 keV in the integral mode [N(E)] under computer control, and then differentiated [dN(E)/dE] and smoothed using a Savitzky-Golay program (24). Intensities were determined from appropriate peak-to-peak heights (pph) and molar concentrations were calculated (25) using the peak-to-peak heights (pph) and published atomic sensitivity factors (26) according to:

$$\frac{X_A}{X_B} = F_{AB}^{A} \times \left(\frac{I_A}{I_A^{\infty}} \right) \Big/ \left(\frac{I_B}{I_B^{\infty}} \right) \qquad (4\text{-}1)$$

where X_A, I_A and I_A^{∞}, respectively, represent the molar concentration, Auger peak-to-peak height (pph) and atomic sensitivity factor of element A. The Auger electron matrix factor F_{AB}^{A} for the element A in a homogeneous binary alloy AB can be estimated by considering backscattering effects and differences in the mean free paths of A and B (25). The error in the intensity ratios due to variations in electron flux from the analyzer has been calculated to be ~ 7%.

The $Ni_3Al(111)$ sample (purchased from MaTeck) had a diameter of 10 mm, and a thickness of 0.5 mm. It was polished on one side with an orientation miscut angle < 0.25°. The sample was spot-welded onto a tantalum plate and placed on a manipulator that can be heated resistively up to ~1100 K. Sample temperature was measured by means of a *K*-type Cr-Al thermocouple not directly attached to the sample. Hence, sample temperatures reported in this chapter must be regarded as approximate.

The $Ni_3Al(111)$ sample contained carbon, oxygen, and sulfur as impurities. The sample was cleaned *in situ* by repeated cycles of Ar^+ sputtering and subsequent annealing

at ~ 1100 K. The cleanliness of the sample was checked by AES, and by the formation of a sharp (2×2) LEED pattern (8). The sample was oxidized at room temperature (~ 300 K) by backfilling the chamber with O_2 gas (99.997% pure, purchased from Matheson) through a manual leak valve at partial pressures in the range from 1×10^{-7} to 5×10^{-7} Torr. Pressure was measured using a nude ion gauge (calibrated for N_2) mounted out of line-of-sight to the sample. Exposures are reported in terms of Langmuir ($1L = 10^{-6}$ Torr-sec) and have not been corrected for ion-gauge sensitivity, flux to the sample, or effects of directional dosing.

The $O_{(510)}$, $Ni_{(848)}$ and $Al_{(1396)}$ Auger intensities were monitored during oxidation and thermal treatment. From the attenuation (I/I_0) of the intensity of the Ni L_3VV peak (848 eV) and calculated mean free path values [$\lambda \cong 18.6$ Å for $Ni_{(848)}$ in Ni_3Al (27)], the thickness (d) of the oxide overlayer can be estimated according to:

$$I = I_0 e^{-d/\lambda} \tag{4-2}$$

In addition, the changes in Al $L_{23}VV$ (68 eV) and Ni $M_{23}VV$ (61 eV) Auger lineshapes, which are sensitive to variations in electronic states (28-30), were monitored to detect the oxidation of $Ni_3Al(111)$. Annealing the oxidized sample for 15-20 minutes at 1000-1100 K resulted in a distinct LEED pattern reported earlier (7,8) for the well-ordered γ'-Al_2O_3 film formed on $Ni_3Al(111)$. The well-ordered γ'-Al_2O_3 film could also be prepared by oxidizing the $Ni_3Al(111)(2\times2)$ at 1000-1100 K, as published previously (7,8).

Surface ordering was checked using STM and LEED. The four-grid retarding field analyzer for LEED measurements was calibrated using a Si(111)(7×7) sample. The LEED pattern of the γ'-Al_2O_3/$Ni_3Al(111)$ (*vide infra*) reveals substrate spots in addition

to those corresponding to the oxide. From the known bulk lattice constant of Ni_3Al (31), the dimension of the surface unit-cell of $Ni_3Al(111)$ can be calculated to be 5.03 Å. Since both the substrate and oxide reciprocal lattices are visible in the LEED pattern of the ordered oxide, errors that arise due to changes in sample position can be eliminated by this method. The sample was transferred between the manipulator and the STM stage by means of a wobble-stick. Constant-current STM topographies were recorded at room temperature by applying a positive bias voltage to the sample (typically, $U_{gap} = + 0.1V$), while maintaining the feedback current at 1 nA. STM tips were prepared by electrochemically etching a polycrystalline tungsten wire (diameter 0.01 in.). STM atomic-resolution images were calibrated with a HOPG (highly oriented pyrolytic graphite) sample. The STM images presented in this chapter have been processed to reduce linear background along the *x*- and *y*- directions of the scan and high frequency noise. The lattice dimensions from LEED and STM have been determined with a precision of ± 0.1.

4.3. Results

4.3.1. Clean $Ni_3Al(111)$

The Auger spectrum of the clean $Ni_3Al(111)$ sample (Fig. 4.1) exhibits the Ni L_3VV transition at 848 eV and the Ni MVV transition at 104 eV. The Al $KL_{23}L_{23}$ transition is observed at 1396 eV. The inset depicts the lineshape of the Ni $M_{23}VV$ transition at 61 eV. The shoulder at 68 eV corresponds to the Al $L_{23}VV$ transition. The molar concentration of aluminum in the $Ni_3Al(111)$ surface was calculated using Eq. (4-1). For NiAl, the matrix factor of the Al (1396 eV) peak is $F_{NiAl}^{Al} = 0.7$ (2), considering

backscattering effects and mean free paths of $Al_{(1396)}$ and $Ni_{(848)}$ (25). Since NiAl and Ni_3Al are both binary alloys of nickel and aluminum, $F^{Al}_{Ni_3Al} \cong F^{Al}_{NiAl} = 0.7$. Substituting in Eq. (4-1), the molar fraction of aluminum in the $Ni_3Al(111)$ surface is estimated to be $X_{Al} \cong 0.24 \pm 0.01$. The value corresponds to a bulk-like composition of aluminum atoms, and

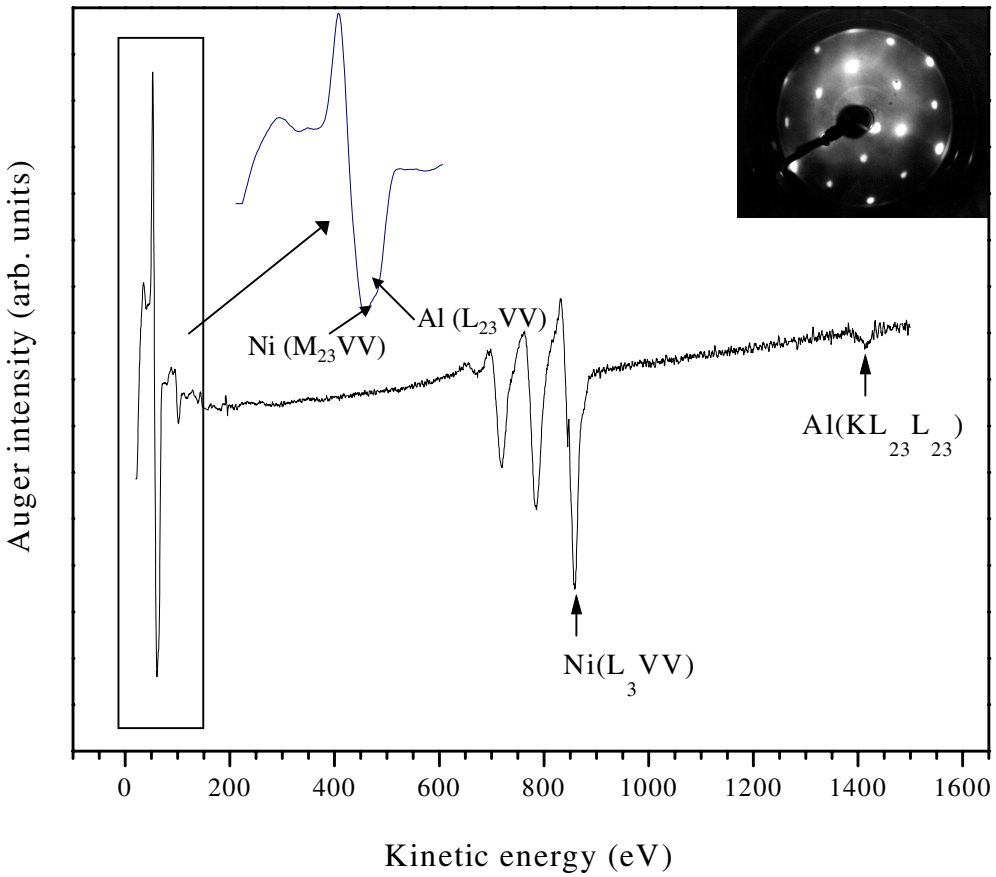

Fig. 4.1. Auger spectrum of clean $Ni_3Al(111)$; insets show the low-energy aluminum and nickel peaks and the (2×2) LEED pattern of the clean sample.

demonstrates that no excess aluminum is present on the clean surface compared with the bulk. Since aluminum is preferentially removed from the surface during Ar^+ sputtering

(32), segregation of aluminum from the bulk to the surface occurs during annealing at T > 900 K until an equilibrium, bulk-like surface composition is attained.

Ni_3Al crystallizes in a face-centered cubic (fcc) lattice, with a stoichiometric composition of three nickel and one aluminum atoms in the {111} plane (32). The bulk unit-cell length is a = 3.56 Å (31). Therefore, the basis vectors in the $Ni_3Al(111)(2\times2)$ surface have a length of $a\sqrt{2}$ = 5.03 Å, corresponding to the distance between two aluminum nearest neighbors. The clean, well-annealed $Ni_3Al(111)$ sample exhibits a sharp (2×2) LEED pattern (inset in Fig. 4.1) (8). The lattice constant calculated from LEED is 4.9 ± 0.1 Å, in accord with the previously proposed (8) "ordered alloy" structure in which every aluminum atom is surrounded by six nearest nickel neighbors in the (111) surface.

Large area (500 nm × 500 nm) STM scans (Fig. 4.2a) show that the clean sample is flat on a nanoscopic scale, with steps oriented along the <110> direction (typical step

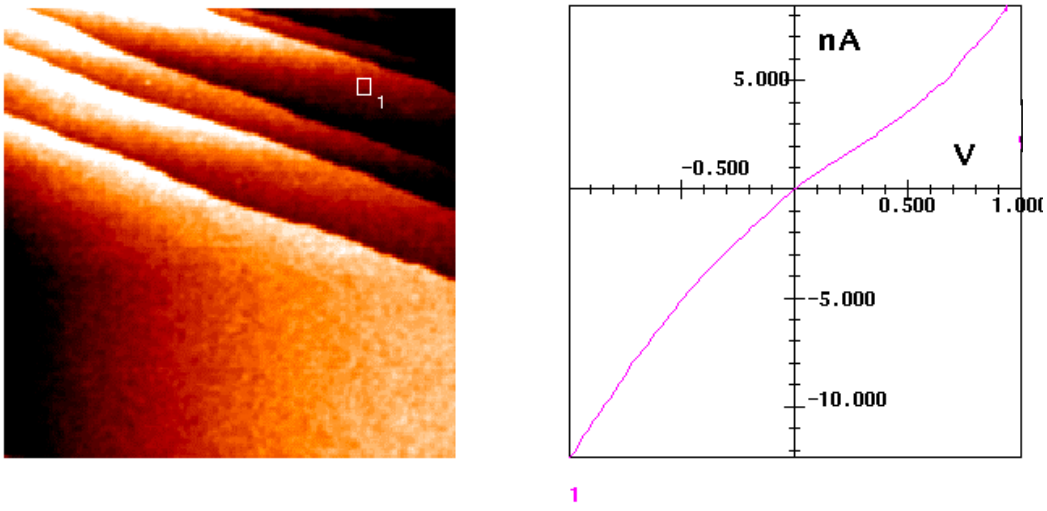

Fig. 4.2 (a). STM image (500 nm × 500 nm) of the clean $Ni_3Al(111)$ surface (U_{gap} = + 0.1 V, I = 1 nA). The I/V curve is also shown.

height ≈ 2–5 Å, terrace width = 10-60 nm). I/V spectroscopy (Fig. 4.2a) of the clean surface demonstrates ohmic behavior. Atomic-resolution imaging (20 nm × 20 nm) of the surface (Fig. 4.2b) reveals a hexagonal array, with a corrugation amplitude of 0.4 ± 0.1 Å, and an average interatomic distance of 4.9 ± 0.1 Å. The interatomic distance is in excellent agreement with the distance between two aluminum nearest neighbors in the $Ni_3Al(111)(2\times2)$ unit-cell. The STM data, along with the AES and LEED results, are consistent with the presence of a bulk-like structure of the $Ni_3Al(111)(2\times2)$ surface (22).

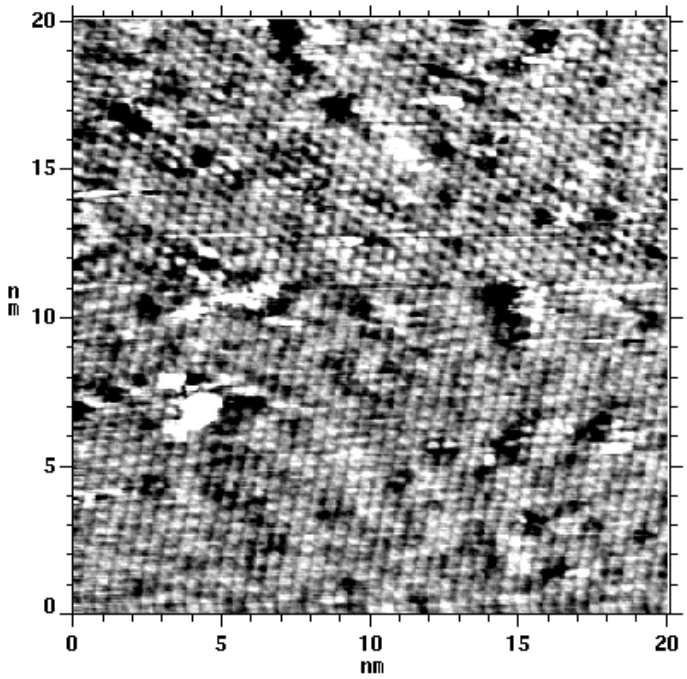

Fig. 4.2 (b). An atomic-resolution (20 nm × 20 nm) STM image of the clean $Ni_3Al(111)$ surface (U_{gap} = + 0.1 V, I = 1 nA).

4.3.2. Oxidation of $Ni_3Al(111)(2\times2)$ at 300 K

The clean $Ni_3Al(111)(2\times2)$ sample was oxidized at ~ 300 K by backfilling the chamber with O_2 gas at partial pressures in the range from 1×10^{-7} to 5×10^{-7} Torr, and the $O_{(510)}/Ni_{(848)}$ ratio vs. O_2 exposure was monitored by AES. The oxygen uptake curve

(Fig. 4.3a) reveals a high sticking probability for oxygen up to an exposure of ~ 64 L. The saturation level is attained at ~ 256 L O_2 when the $O_{(510)}/Ni_{(848)}$ atomic ratio ≅ 0.57 ± 0.09.

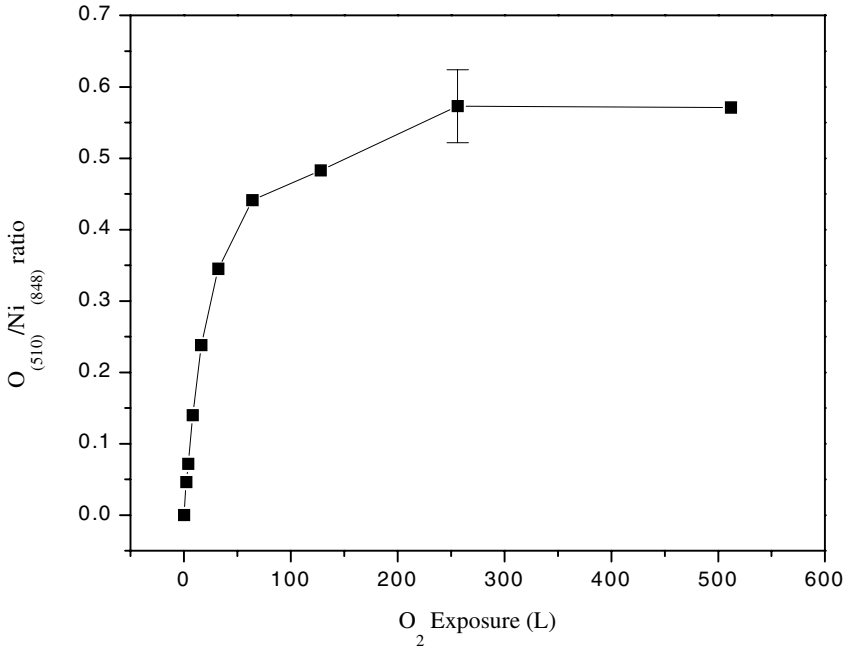

Fig. 4.3 (a). Changes in the $O_{(510)}/Ni_{(848)}$ intensity ratio vs. O_2 exposure on clean $Ni_3Al(111)$ at 300 K.

Changes in the low-energy aluminum and nickel Auger spectral lineshapes have been used to estimate the degree of oxidation of the Ni_3Al sample (28-30). The oxidation of aluminum is characterized by the shift of the metallic aluminum peak (68 eV) to 54 eV (28,29), and the onset of a shoulder at 38 eV (28,29). Similarly, the conversion of nickel to Ni^{2+} is signified by a shift of the Ni $M_{23}VV$ metallic peak (61 eV) to 53.5 eV (30). Thus, in case of the Ni_3Al sample, there would be considerable overlap in the spectral region of 50-60 eV in the event of oxidation of both nickel and aluminum, and detection

of nickel oxidation in particular would be problematic. The extensive overlap of the metallic/oxidized nickel and aluminum peaks also makes accurate quantification of the Auger data difficult. The evolution of the Auger low-energy lineshape with increasing O_2 exposure at 300 K is shown in Fig. 4.3b. The disappearance of the metallic aluminum peak (68 eV) and the appearance of the Al^{3+} shoulder at 38 eV demonstrate the oxidation of aluminum (28,29).

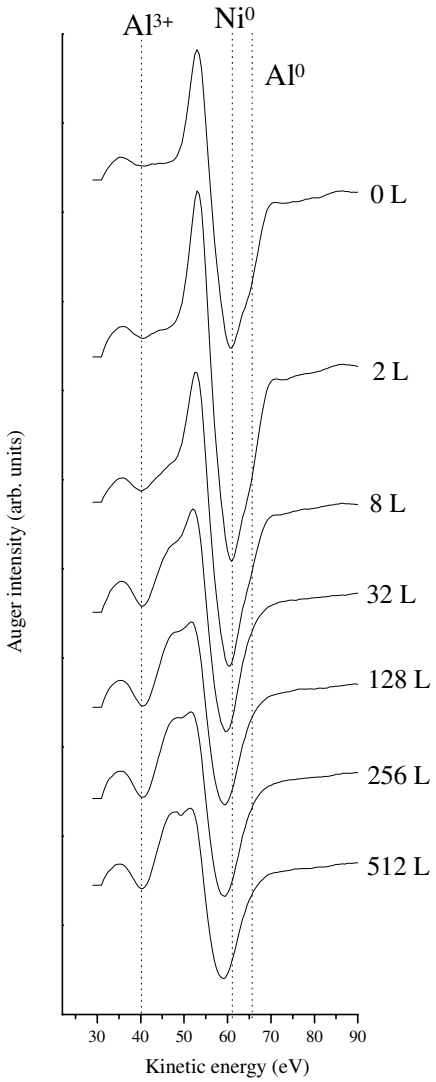

Fig. 4.3 (b). Changes in the Auger lineshape with increasing exposure of the $Ni_3Al(111)$ sample to O_2 at 300 K.

The oxide prepared at ~ 300 K exhibits no LEED pattern, indicating the absence of long-range order, consistent with previous reports for the oxidation of single-crystal Ni-Al alloys (2,8-10,20,33,34). The initial stages of oxidation of $Ni_3Al(111)$ at ~ 300 K were studied by STM imaging (Fig. 4.4). The clean sample was exposed to 2.65 L O_2 at 3.2×10^{-8} Torr partial pressure at ~ 300 K [$O_{(510)}/Ni_{(848)}$ atomic ratio after oxidation ≅ 0.05]. The Auger low-energy region (not shown) shows a decrease in the intensity of the $Al_{(68)}$ peak (although it does not disappear completely) after 2.65 L exposure, demonstrating that the oxidation of aluminum commences at exposures as low as 2.65 L on a clean $Ni_3Al(111)$ surface. STM images were obtained after oxidation at 2.65 L O_2 exposure (U_{gap} = + 0.1 V, I = 1 nA). Large area scans (not shown) display oxide islands scattered on step terraces, consistent with the results of a recent

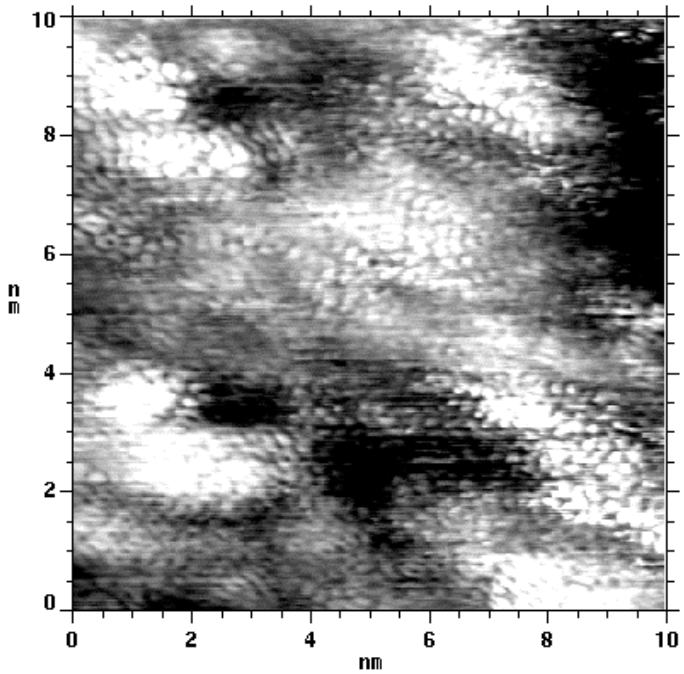

Fig. 4.4. STM (10 nm × 10 nm) image of the $Ni_3Al(111)$ surface after exposure to 2.65 L O_2 at 300 K (U_{gap} = + 0.1 V, I = 1 nA).

STM study of the oxidation of $Ni_3Al(111)$ (22). A high-resolution (10 nm × 10 nm) topograph (Fig. 4.4) reveals no ordered structures. However, a nearest-neighbor spacing of 3.0 ± 0.1 Å is observed. The STM data are consistent with findings by low energy ion scattering (LEIS) demonstrating that oxide growth on Ni_3Al single crystals at T < 900 K occurs by formation of islands (7,21) interspersed with patches of the uncovered (2×2) substrate (35). STM studies of the oxidation of $Ni_3Al(110)$ (19) have also reported oxide island formation at T < 970 K. Recent STM studies of the variable-temperature oxidation of $Ni_3Al(111)$ (22) have reported that the ratio of oxide islands formed on terraces to those formed at steps is highly dependent upon the adsorption temperature. The temperature of the surface during oxidation controls the mobility of the aluminum and oxygen atoms in the surface (22). At T = 1000 K, oxide nucleation occurs preferentially at step edges, due to the high mobility of oxygen and aluminum atoms (22).

4.3.3. The well-ordered γ′-Al_2O_3

The $Ni_3Al(111)$ with ~ 4.0% sulfur and ~ 5.2% carbon impurities was oxidized at ~ 300 K in the presence of excess O_2 (~ 700 L, $P_{O_2} = 1 \times 10^{-7}$ to 5×10^{-7} Torr). The oxidized sample was progressively annealed in UHV up to ~ 1100 K (in steps of 100 K) for 15 minutes at each temperature. The $O_{(510)}/Al_{(1396)}$, $O_{(510)}/Ni_{(848)}$ and $Al_{(1396)}/Ni_{(848)}$ ratios (Fig. 4.5a) and LEED were monitored with increasing temperature. The $O_{(510)}/Al_{(1396)}$ ratio (Fig. 4.5a) decreases steadily upon successive annealing and attains a value of ~ 0.71 ± 0.02 at ~ 1100 K. A decrease in the $O_{(510)}/Al_{(1396)}$ ratio was also

observed when an oxidized NiAl(111) sample was annealed at various temperatures (10). In contrast, the $O_{(510)}/Ni_{(848)}$ ratio (= 0.57 ± 0.09 at 300 K) (Fig. 4.5a) decreases up to T = 500 K, then increases up to ~ 900 K, after which a decline in the ratio is observed again [$O_{(510)}/Ni_{(848)}$ ratio after annealing to 1100 K ≅ 0.64 ± 0.05]. This is different from the case of the NiAl(111) sample (10), where a steady decay in the $O_{(510)}/Ni_{(848)}$ ratio vs. temperature was observed during annealing. An increase in the $Al_{(1396)}/Ni_{(848)}$ ratio (Fig. 4.5a) and the appearance of the Al^0 peak (Fig. 4.5b) as the sample is annealed to elevated temperatures demonstrate aluminum segregation to the oxidized $Ni_3Al(111)$ surface upon annealing.

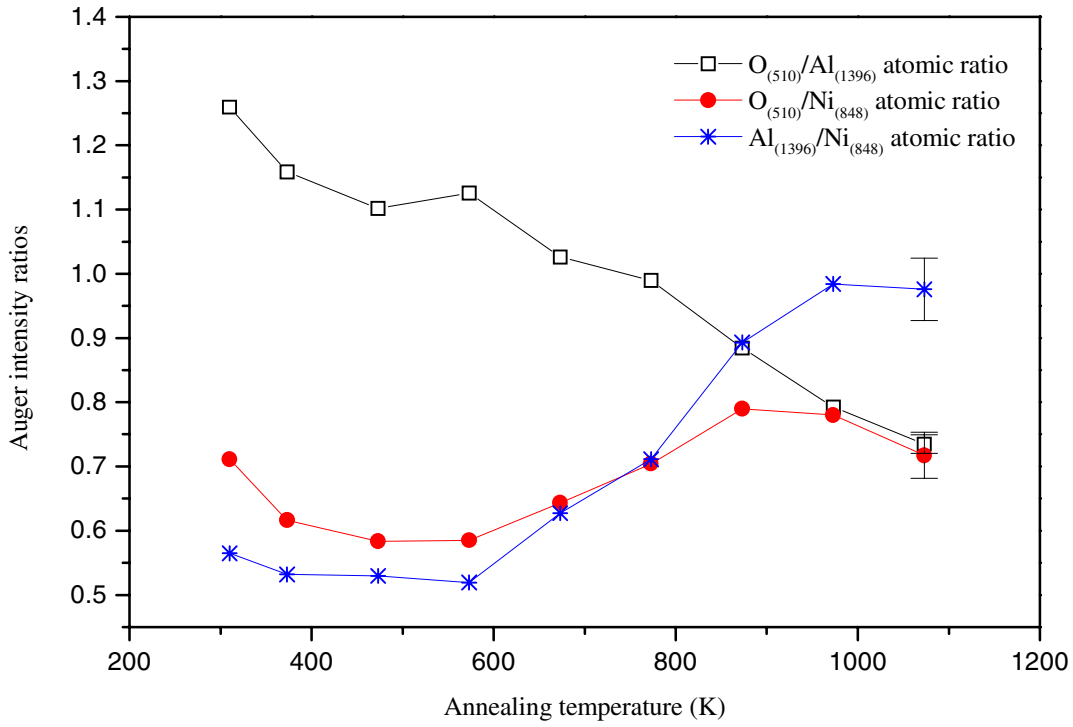

Fig. 4.5 (a). Effect of annealing the oxide formed on the $Ni_3Al(111)$ surface at 300 K: $O_{(510)}/Al_{(1396)}$, $Al_{(1396)}/Ni_{(848)}$ and $O_{(510)}/Ni_{(848)}$ atomic ratios vs. annealing temperature.

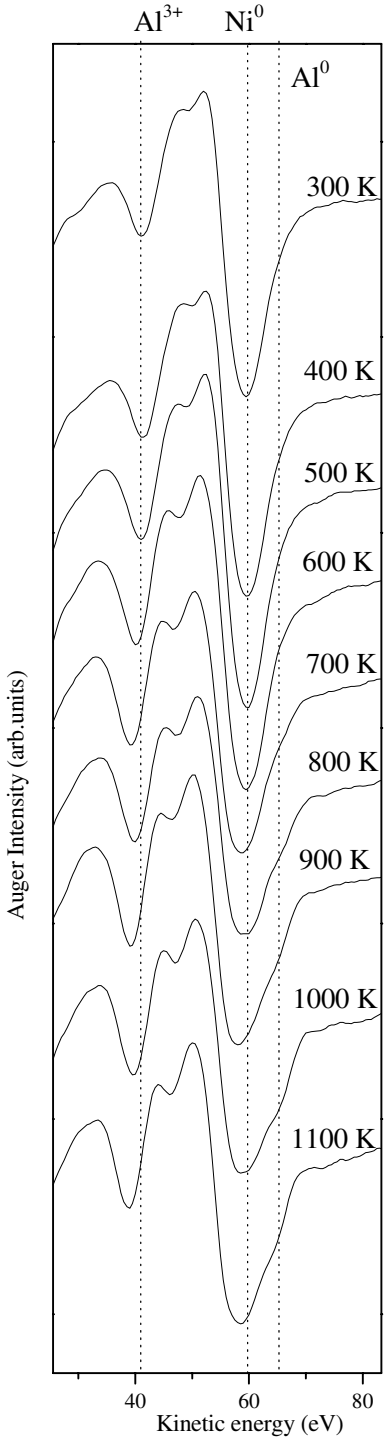

Fig. 4.5 (b). Effect of annealing the oxide formed on the $Ni_3Al(111)$ surface at 300 K: low-energy lineshape (Auger) vs. annealing temperature.

It has already been shown (Fig. 4.4) that oxidation of the $Ni_3Al(111)$ surface proceeds via formation of oxide islands, in agreement with earlier results (7,19,21,22,35). The formation of oxide islands on the $Ni_3Al(111)$ surface at room temperature would attenuate the $Ni_{(848)}$ intensity to a lesser extent than would a uniform oxide overlayer. The Auger data (Fig. 4.5) indicate that the oxide film 'spreads out' across the surface in the temperature range of 500-800 K, causing further attenuation of the nickel signal, which leads to an increased $O_{(510)}/Ni_{(848)}$ ratio. Above ~ 800 K, the formation of metallic aluminum is observed in the Auger lineshape (Fig. 4.5b), consistent with aluminum segregation to the $Ni_3Al(111)$ surface upon annealing (32). Studies on oxidation of β-NiAl(110) have also observed the appearance of metallic aluminum (68 eV) peak in the Auger spectrum after oxidation at 973 K and subsequent annealing to 1073 K (14). Using Eq. (4-2), the thickness of the overlayer after annealing was estimated to be 7.5 ± 1.0 Å.

Annealing the oxide grown at room temperature on clean $Ni_3Al(111)$ to ~ 1100 K for 15-20 minutes results in the formation of the well-ordered γ'-Al_2O_3 with a LEED pattern (Fig. 4.6) that has been studied extensively (7,8). The LEED pattern demonstrates a hexagonal symmetry for the oxide. This pattern (Fig. 4.6) indicates the existence of two domains of the oxide that are rotated at angles of 24.5° and 37.5° with respect to the substrate, with a lattice spacing of 2.9 ± 0.1 Å. These values are in good agreement with those reported by Becker et al. (8). The presence of substrate spots in the LEED pattern demonstrates that the overlayer is a very thin film of aluminum oxide (8).

STM images of the ordered oxide film were acquired after the sample was cooled to room temperature. These images were recorded at a bias voltage (U_{gap}) of + 0.1 V, while maintaining the feedback current (I) at 1 nA. Large-area (500 nm × 500 nm) STM (constant-current tunneling) scans (Fig. 4.7a) of the ordered oxide show steps oriented along the <110> direction with typical step height equal to 2.8-5.3 Å and terrace widths ranging from 25nm to 125 nm. According to the LEED pattern (Fig. 4.6) of the ordered oxide, two domains that are rotated at 37.5° and 24.5° with respect to the substrate coexist on the surface, consistent with earlier reports (8). Attempts to identify the two domains by STM imaging were unsuccessful. Atomic-resolution (5 nm × 5 nm) imaging (Fig. 4.7b) reveals a hexagonal array of corrugations with an interatomic distance of 3.0 ± 0.1 Å. Based on the STM atomic-resolution images and LEED, a probable interpretation for the surface structure of the well-ordered γ-Al_2O_3 film is a $(1/\sqrt{3}\times 1/\sqrt{3})$ mesh on the $Ni_3Al(111)(2\times 2)$ substrate.

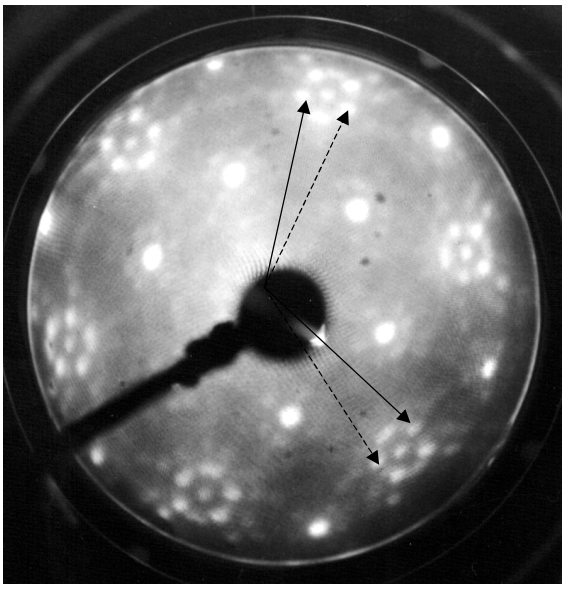

Fig. 4.6. LEED pattern of the ordered oxide after annealing at 1100 K for 15-20 minutes, E = 60 eV.

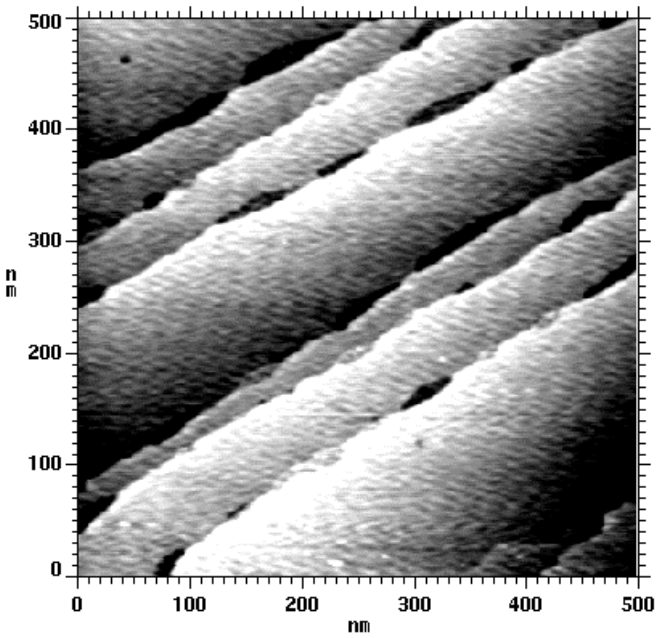

(a)

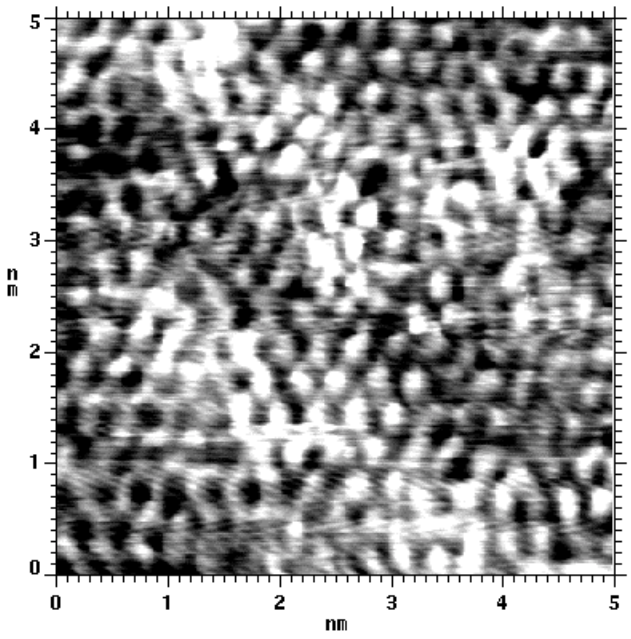

(b)

Fig. 4.7. STM images of the well-ordered oxide (U_{gap} = + 0.1 V, I = 1 nA): (a) large area scan (500 nm × 500 nm), (b) atomic-resolution image (5 nm × 5 nm).

4.4. Discussion

Aluminum oxide exists in the form of several phases in different temperature ranges (2). Room-temperature oxidation of Ni-Al alloys yields an amorphous aluminum oxide (*a*-Al_2O_3) phase that is stable up to 700 K. This phase is comprised of densely packed, randomly oriented oxygen clusters, with aluminum ions seated in tetrahedral sites (2). Upon annealing at temperatures in the range of 700-1200 K, the amorphous phase is transformed into the γ-like Al_2O_3 phase (referred to as γ′-Al_2O_3 in this report), which consists of octahedrally and tetrahedrally coordinated aluminum cations in an fcc oxygen sublattice (2). The θ-Al_2O_3 is the stable phase in the temperature range of 1200-1350 K (2). An α-like, faceted Al_2O_3 phase exists at temperatures > 1350 K (2,10). Annealing at T ≥ 1500 K leads to the decomposition of the oxide (2,10). We have characterized the γ′-Al_2O_3 thin film formed on Ni_3Al(111) at 1000-1100 K with the use of STM, AES and LEED.

Since the clean surface of the alloy is highly reactive, oxidation of Ni_3Al(111) at very low O_2 exposures (~ 3 L O_2) is not surprising. At ~ 300 K, the oxide formed by saturation exposure to O_2 does not display any long-range order as evidenced by LEED measurements. Similar results have been reported for the room-temperature oxidation of NiAl(001) (2,9,20,33), NiAl(110) (34) and NiAl(111) (10). High-resolution STM imaging at low oxygen exposures (Fig. 4.4) has revealed that oxidation proceeds via the formation of randomly oriented clusters with a nearest-neighbor distance of 3.0 ± 0.1 Å. Previously published reports for the room-temperature oxidation of NiAl(001) (9,20) have suggested the formation of a stable amorphous alumina phase with Al-O clusters.

These clusters are proposed to be comprised of randomly oriented oxygen fcc lattices in which the Al^{3+} occupy either octahedral or tetrahedral sites, consistent with an observed nearest-neighbor distance of 3.0 ± 0.1 Å (Fig. 4.4). This is analogous to the structure of the amorphous *a*-Al_2O_3 that is formed at 300 K (2).

Based on the enthalpies of formation of Al_2O_3 (ΔH_f = -1675.7±1.3 kJ mol^{-1}) and NiO (ΔH_f = -240.8 kJ mol^{-1}) (36), aluminum oxidation is thermodynamically more favorable. Hence, one expects that aluminum would be preferentially oxidized in the $Ni_3Al(111)$ surface. In the case of $Ni_3Al(111)$, however, the surface concentration of aluminum atoms is only ~ 25%. This implies that the formation of a uniform aluminum oxide film is not possible at room temperature. To promote the formation of a well-ordered aluminum oxide on the $Ni_3Al(111)$, aluminum atoms should segregate from the bulk to the surface. Since the thermal energy at room temperature is insufficient to promote diffusion of aluminum to the $Ni_3Al(111)$ surface, interaction of oxygen with both aluminum and nickel atoms is expected even at low O_2 partial pressures. Therefore, it is possible that the oxide formed at ~ 300 K is a mixture of both nickel oxide and amorphous Al_2O_3. Stirniman et al. (37) have demonstrated that AES is not a reliable technique for investigating the oxidation of nickel, since oxidation rates show an inverse dependence with temperature in the presence of the Auger electron beam. At room temperature and above, however, the effect of electron beam on oxidation rates was found to be small (37). In the present report, the oxidation of nickel cannot be conclusively established due to the overlap of the $Ni_{(61)}$ and $Al_{(68)}$ peaks in the Auger spectrum (Fig. 4.1). Becker et al. (8), however, have previously reported that HREELS measurements revealed the presence of energy-loss peaks that correspond to nickel-

oxygen interaction when the clean $Ni_3Al(111)$ was exposed to oxygen at room temperature. Furthermore, these authors demonstrated that the HREELS peaks associated with Ni-O interaction (8) disappeared from the HREELS spectrum when the oxide was heated above 800 K. Therefore, the disappearance of these peaks is attributable to the displacement of the nickel atoms in the Ni-O complex by the segregating aluminum atoms. At temperatures above ~ 600 K, segregation of aluminum is confirmed by the appearance of the metallic aluminum Auger signal at 68 eV (Fig. 4.5b). This result is consistent with previous studies that reported aluminum segregation upon annealing the clean $Ni_3Al(111)$ (32) and low-index single-crystal NiAl samples (14). As the oxidized $Ni_3Al(111)$ is annealed to higher temperatures, segregation of aluminum promotes the formation of the well-ordered γ-Al_2O_3.

The surface concentration of aluminum after annealing the $Al_2O_3/Ni_3Al(111)$ sample at ~ 1100 K was calculated using Eq. (4-1), giving a value of about 40%. Given the molar concentration of aluminum in the clean $Ni_3Al(111)$ surface of 25%, the aluminum concentration after the thermal treatment of the oxide represents a 60% increase of aluminum atoms in the $Ni_3Al(111)$ surface. While it is not possible to distinguish the neutral aluminum atoms from the Al^{3+} ions using AES, one can estimate the fraction of the intensity contributed by the Al^{3+} ions in the $Al_{(1396)}$ Auger transition using Eq. (4-3):

$$\frac{I_{surface}}{I_{total}} = \frac{\int_0^{2.12} e^{-x/\lambda} dx}{\int_0^{\infty} e^{-x/\lambda} dx} \qquad (4\text{-}3)$$

where x is the thickness of two layers of Al^{3+} (diameter of Al^{3+} = 1.06 Å), and the mean free path (λ) of the Al (1396 eV) peak in Ni_3Al is ~ 27 Å (27). The contribution from the Al^{3+} ions is estimated to be ~ 7.5%. In using Eq. (4-3), however, it is assumed that two layers of Al^{3+} ions exist in the surface. Since the concentration of the Al^{3+} ions in the γ-Al_2O_3 is considerably lower than a double layer of Al^{3+} ions due to the random distribution of Al^{3+} in the oxygen sublattice (2), the actual contribution due to Al^{3+} ions is < 7.5% of the total $Al_{(1396)}$ intensity. Therefore, the surface concentration of metallic aluminum after annealing the oxidized sample is close to 40%. One may argue that this segregated aluminum resulted in the change in the structure of the surface of the Ni_3Al alloy, giving rise to a surface composition of Ni_3Al_2, and that the metallic aluminum observed in the Auger spectra collected after annealing the sample above ~ 600 K is due to the Ni_3Al_2 surface. The LEED pattern shown in Fig. 4.6, however, does not support this interpretation. It is evident from this pattern that the substrate (first-order) spots correspond to the $Ni_3Al(111)$ surface structure in which the molar concentration of aluminum is 25%. An alternative interpretation is that the 'excess' aluminum atoms form an interfacial layer between the oxide and the Ni_3Al substrate. The observation that exposing the γ-Al_2O_3 to additional doses of oxygen at ~ 1100 K does not yield a thicker oxide provides a strong evidence that the 'excess' metallic aluminum is present at the $Ni_3Al(111)$-Al_2O_3 interface. This demonstrates that the transport of aluminum and/or oxygen is passivated by the 7.5 ± 1.0 Å thick oxide layer. Sondericker et al. (32) observed that in the case of the clean $Ni_3Al(111)(2\times2)$ surface, an $Al_{(68)}/Ni_{(61)}$ ratio corresponding to a surface concentration of aluminum atoms that is higher than 25% is unstable (32). According to these authors, the 'excess' aluminum diffuses back into the

bulk to re-establish the equilibrium concentration of the $Ni_3Al(111)$ (32). On the other hand, in the case of the γ-$Al_2O_3/Ni_3Al(111)$ system, the excess aluminum remained close to the oxide-alloy interface. To account for the aluminum enrichment at the oxide-alloy interface, we postulate that the aluminum interfacial layer is stabilized by oxygen chemisorption. Wandelt and coworkers (8) have found that γ-Al_2O_3 on $Ni_3Al(111)$ exhibits an HREELS energy-loss peak that characterizes chemisorption of oxygen on an Al(111) surface. Oxidation studies on $Ni_3Al(110)$ (19) have also presented results that showed the formation of the interfacial aluminum layer. A quasi-hexagonal layer of Al(111) on top of a 100% nickel layer on the $Ni_3Al(110)$ surface was recently proposed by Cotterill et al. (19) in order to account for the formation of an incommensurate oxygen-induced reconstruction on the $Ni_3Al(110)$ at 970 K. These authors (19) were able to demonstrate the existence of an Al(111)(1×1) layer with the use of LEED, where they obtained a pattern that consisted of a hexagonal overlayer with a lattice spacing (2.9 Å) consistent with the Al-Al separation. In the case of oxide formation on $Ni_3Al(111)$ at ~ 1100 K, the presence of a similar Al(111) interfacial layer with chemisorption sites for oxygen cannot be established unambiguously with the use of LEED, because the Al(111)(1×1) spots coincide with the second-order spots of the $Ni_3Al(111)(2\times2)$ substrate. While there is no direct evidence from LEED to definitively establish the existence of an Al(111)(1×1) interfacial layer, the results obtained from AES measurements - i.e., the 60% increase in the $Al_{(1396)}/Ni_{(848)}$ Auger atomic ratio and the appearance of the metallic $Al_{(68)}$ peak in the Auger surface-sensitive region - support the idea that an interfacial layer is formed upon annealing the oxide to ~ 1100 K.

The LEED pattern of the well-ordered γ′-Al_2O_3 is depicted in Fig. 4.6. The lattice constant for the γ′-Al_2O_3/Ni_3Al(111) obtained by LEED (Fig. 4.6) is 2.9 ± 0.1 Å. The ordering due to Al^{3+} ions (diameter = 1.06 Å) is not expected in the LEED pattern (Fig. 4.6) due to their smaller size relative to the O^{2-} ions (diameter = 2.8 Å) (18). According to Chen and Goodman (18), the "epitaxial relationship and the arrangement of ions" in the aluminum oxide overlayer are dominated by the larger O^{2-} ions. Hence, the LEED pattern observed for the γ′-Al_2O_3 can be attributed to the lattice arrangement of the O^{2-} anions. The lattice spacing of 2.9 ± 0.1 Å obtained from LEED (Fig. 4.6) would represent the (111) surface of the γ′-Al_2O_3, since the basis vectors for the (1×1) unit-cell of the (111) surface of the γ′-Al_2O_3 have a length of $a/\sqrt{2}$ = 2.79 Å (7). LEED studies of the growth of the γ′-Al_2O_3 film on Ni_3Al(111) (7), and NiAl(111) (10) have also suggested the growth of the (111) surface of the oxide on the corresponding substrate. The fact that the ordering due to O^{2-} ions is reflected in the LEED pattern (Fig. 4.6) does not, however, necessarily imply that the surface of the γ′-Al_2O_3 film on Ni_3Al(111) is oxygen-terminated. Many authors have concluded in various reports (5,10,13,18) that the thin film of Al_2O_3 grown on single-crystal metal/alloy surfaces is preferentially O^{2-}-terminated. This conclusion is largely based on the chemical inertness of the prepared oxide to various gas molecules (5,18). In this report, however, there is no clear evidence that can reveal the surface termination for the oxide film. Furthermore, theoretical calculations performed by Jennison et al. (3) on Al_2O_3(001)/Al(111) have shown that the Al^{3+} ions are accommodated nearly in the same plane as the oxygen anions for electroneutrality. Hence, the γ′-Al_2O_3 film may exhibit, *de facto*, either an O^{2-} or Al^{3+}

surface termination. In practice, however, the larger size of the oxygen anions would dominate oxide surface spectra and properties.

Atomic-resolution (5 nm × 5 nm) imaging of the ordered oxide film (Fig. 4.7b) reveals a hexagonal array of corrugations with an interatomic distance of 3.0 ± 0.1 Å. In STM images that are atomically resolved, identification of specific species largely depends on the electronegativity, atomic size and polarizability (spatial extension of atomic orbitals) of the substrate/adsorbate atoms, the characteristics of the tip, the tunneling parameters chosen, and tip-surface interactions (38,39). Therefore, theoretical modeling is necessary to extract meaningful information regarding surface structure and ordering in STM images. In the absence of such models, however, other reliable information such as lattice constants and surface reactivity obtained from a variety of surface science tools including AES and LEED could be used to interpret STM atomic-resolution images. The existence of the oxide overlayer on the $Ni_3Al(111)$ has been unambiguously established by AES analysis. STM images (Fig. 4.7b) and the LEED pattern (Fig. 4.6) of the oxide give almost identical lattice dimensions. The possibility that Al^{3+} ions are the ones imaged in the STM is unlikely on the basis of theoretical considerations. Although a recent theoretical study of bulk γ-Al_2O_3 (4) has shown that cation vacancies preferentially occupy octahedral sites, the structure of this alumina is still a subject of controversy (2,4). Because the film thickness of the γ'-Al_2O_3 obtained in the present work corresponds only to approximately two oxide layers, it probably would not assume the bulk structure of γ-Al_2O_3. Theoretical calculations (3) carried out for such ultrathin films indicate that tetrahedral coordination of Al^{3+} is energetically preferred, and that at room temperature, the Al^{3+} sublattice is probably disordered (3). Such random

distribution would not register any coherent structure in the STM images. Since the LEED provides evidence for the lattice configuration of the O^{2-} ions, one might infer that the corrugations observed in the STM images are associated with the O^{2-} ions. It is important to note, however, that under the tunneling conditions employed, i.e., bias voltages of + 0.1 V, the oxide surface structure cannot be clearly detected by STM. At these low bias voltages, electrons tunnel into the electronic states of the underlying metal instead of those of the oxide, with the oxide overlayer behaving as a tunneling barrier (40). The surface structure of the oxide can be detected accurately at higher values of sample bias, as observed for STM imaging of SiO_2/Si(111) (40). Therefore, it is more likely that the STM atomic resolution image (Fig. 4.7b) corresponds to the γ'-Al_2O_3(111)-Ni_3Al(111) interface. STM studies of ordered Al_2O_3 films prepared on NiAl(110) (16,17) have also reported imaging of the oxide-alloy interface at low bias voltages. We have already established that the γ'-Al_2O_3(111)-Ni_3Al(111) interface is enriched with aluminum as a result of segregation from the bulk during annealing. Therefore, the protrusions observed in the STM atomic-resolution image (Fig. 4.7b) are tentatively assigned to the aluminum atoms at the γ'-Al_2O_3(111)-Ni_3Al(111) interface. The interatomic distance of 3.0 ± 0.1 Å observed in the atomic-resolution image (Fig. 4.7b) would represent the (111) surface of aluminum (31).

On the basis of the AES, LEED and STM results discussed in this chapter, we propose the presence of: (1) a γ'-Al_2O_3(111) film with a hexagonal symmetry, and an average O^{2-}-O^{2-} spacing of 3.0 ± 0.1 Å, and (2) an aluminum-enriched interfacial layer between the ultrathin oxide film and the Ni_3Al(111) surface. The surface termination of

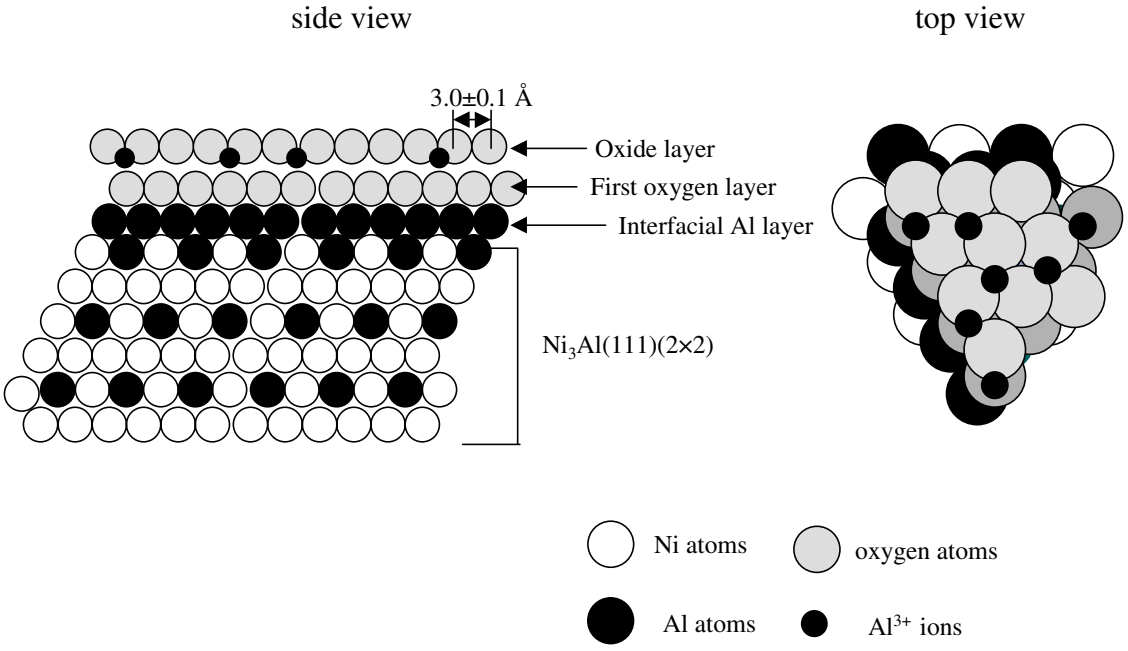

Fig. 4.8. Proposed structure for the γ′-Al_2O_3(111)-Ni_3Al(111) interface (side view and top view). Placement of Al^{3+} ions on top is purely schematic and not meant to conform to actual positions. Schematic is not drawn to scale.

the oxide film could be either O^{2-} or Al^{3+}. A thickness of 7.5 ± 1.0 Å indicates that the oxide film consists of more than one oxygen layer, consistent with earlier experimental (5,7,8) and theoretical (3) studies that proposed the formation of two Al-O bilayers. Based on the tunneling conditions employed, the protrusions observed in the STM atomic-resolution image (Fig. 4.7b) are tentatively assigned to aluminum atoms at the γ′-Al_2O_3-Ni_3Al(111) interface. The interatomic distance of 3.0 ± 0.1 Å obtained by STM atomic-resolution imaging (Fig. 4.7b) and LEED (Fig. 4.6) is in very good agreement with the average lattice spacing (2.90 ± 0.05 Å) for oxygen atoms chemisorbed in three-fold hollow sites of Al(111) (41). This indicates that the two oxygen layers should be in

registry with each other, with the first layer consisting of oxygen atoms adsorbed in three-fold hollow sites of the aluminum interfacial layer. The proposed model for the γ′-Al_2O_3 on the $Ni_3Al(111)$ surface is displayed in Fig. 4.8. This model consists of an aluminum layer of (111) orientation on top of the $Ni_3Al(111)$ substrate. The aluminum layer, which contains three-fold hollow sites, is in registry with the hexagonal symmetry of the $Ni_3Al(111)$ surface. The oxygen atoms of the first layer of the oxide are chemisorbed on the three-fold aluminum sites. The second oxide layer and the chemisorbed oxygen layer are connected by either tetrahedrally or octahedrally coordinated Al^{3+} ions. The Al^{3+} ions serve as anchors between the (1×1)-O chemisorbed layer and the higher oxide layer. The proposed structure for the γ′-$Al_2O_3(111)/Ni_3Al(111)$ correlates with the results of theoretical simulations on $Al_2O_3(001)/Al(111)$ (3).

4.5. Summary and Conclusions

In summary, the results reported in this chapter demonstrate that the clean $Ni_3Al(111)$ surface exhibits a bulk-like, (2×2) arrangement of aluminum atoms. Oxidation of $Ni_3Al(111)$ commences at exposures of O_2 as low as ~ 3 L, and oxide growth occurs in the form of randomly oriented oxide islands. The oxide exhibits no long-range order at ~ 300 K, demonstrating the formation of an *a*-Al_2O_3 phase that is known to be the product of the room-temperature oxidation of Ni-Al alloys. At T ≥ 800 K, the amorphous *a*-Al_2O_3 is transformed into the γ′-oxide film. AES measurements obtained by annealing the disordered oxide from 300-1100 K reveal aluminum

enrichment, and provide evidence for the formation of an aluminum-rich layer at the γ-Al_2O_3(111)-Ni_3Al(111) interface. The LEED pattern of the γ-Al_2O_3 reveals the ordering of the oxygen anions in the aluminum oxide surface, with a lattice constant of 2.9 ± 0.1 Å. STM atomic-resolution images corroborate the hexagonal symmetry of the Al_2O_3(111) film, with an average interatomic spacing of 3.0 ± 0.1 Å. Based on the tunneling parameters used, the protrusions observed in the atomic-resolution images have been tentatively assigned to the aluminum atoms located at the Al_2O_3-Ni_3Al(111) interface.

4.6. Chapter References

(1) Henrich, V. E.; Cox, P. A. *The Surface Science of Metal Oxides*; Cambridge University Press:, 1996.

(2) Gassmann, P.; Franchy, R.; Ibach, H. *Surf. Sci.* **1994**, *319*, 95.

(3) Jennison, D. R.; Verdozzi, C.; Schultz, P. A.; Sears, M. P. *Phys. Rev. B* **1999**, *59*, R15605.

(4) Mo, S.-D.; Xu, Y.-N.; Ching, W.-Y. *J. Am. Ceram. Soc.* **1997**, *89*, 1193.

(5) Jaeger, R. M.; Kuhlenbeck, H.; Freund, H.-J.; Wuttig, M.; Hoffmann, W.; Franchy, R.; Ibach, H. *Surf. Sci.* **1991**, *259*, 235.

(6) Street, S. C.; Xu, C.; Goodman, D. W. *Ann. Rev. Phys. Chem.* **1997**, *48*, 43.

(7) Bardi, U.; Atrei, A.; Rovida, G. *Surf. Sci.* **1992**, *268*, 87.

(8) Becker, C.; Kandler, J.; Raaf, H.; Linke, R.; Pelster, T.; Dräger, M.; Tanemura, M.; Wandelt, K. *J. Vac. Sci. Technol. A* **1998**, *16*, 1000.

(9) Blum, R.-P.; Niehus, H. *Applied Physics A* **1998**, *66*, S529.

(10) Franchy, R.; Masuch, J.; Gassmann, P. *Appl. Surf. Sci.* **1996**, *93*, 317.

(11) Venezia, A. M.; Loxton, C. M. *Surf. Sci.* **1988**, *194*, 136.

(12) Venezia, A. M.; Loxton, C. M. *Surf. Interface Anal.* **1988**, *11*, 287.

(13) Klimenkov, M.; Nepijko, S.; Kuhlenbeck, H.; Freund, H.-J. *Surf. Sci.* **1997**, *385*, 66.

(14) Viefhaus, H.; Roux, J. P.; Grabke, H. J. *Fresenius J. Anal. Chem.* **1993**, *346*, 69.

(15) Libuda, J.; Winkelmann, F.; Bäumer, M.; Freund, H.-J.; Bertrams, T.; Neddermeyer, H.; Mueller, K. *Surf. Sci.* **1994**, *318*, 61.

(16) Bertrams, T.; Brodde, A.; Hannemann, H.; C. A. Ventrice, J.; Wilhelmi, G.; Neddermeyer, H. *Appl. Surf. Sci.* **1994**, *75*, 125.

(17) Bertrams, T.; Brodde, A.; Neddermeyer, H. *J. Vac. Sci. Technol. B* **1994**, *12*, 2122.

(18) Chen, P. J.; Goodman, D. W. *Surf. Sci.* **1994**, *312*, L767.

(19) Cotterill, G. F.; Niehus, H.; O'Connor, D. J. *Surf. Rev. Lett.* **1996**, *3*, 1355.

(20) Blum, R.-P.; Ahlbehrendt, D.; Niehus, H. *Surf. Sci.* **1998**, *396*, 176.

(21) Bardi, U.; Atrei, A.; Rovida, G. *Surf. Sci. Lett.* **1990**, *239*, L511.

(22) Rosenhahn, A.; Schneider, J.; Becker, C.; Wandelt, K. *Appl. Surf. Sci.* **1999**, *142*, 169.

(23) Lin, J.-S.; Cabibil, H.; Ekstrom, B.; Kelber, J. A. *Surf. Sci.* **1997**, *371*, 337.

(24) RBD Enterprises, Bend, OR 97702.

(25) Seah, M. P. in *Practical Surface Analysis: Auger and X-ray Photoelectron Spectroscopy*; 2 ed.; Briggs, D. and Seah, M. P., Eds.; Wiley: New York, 1990; Vol. 1, p 201.

(26) Davis, L. E.; MacDonald, N. C.; Palmberg, P. W.; Raich, G. E.; Weber, R. E. *Handbook of Auger Electron Spectroscopy*; 2 ed.; Physical Electronics Industries, Inc.: Eden Prairie, 1979.

(27) Powell, C. J.; Jablonski, A.; Tilinin, I. S.; Tanuma, S.; Penn, D. R. *J. Electron Spectrosc. Relat. Phenom.* **1999**, *98-99*, 1.

(28) Chen, J. G.; Crowell, J. E.; Yates, J. T., Jr. *Phys. Rev. B* **1986**, *33*, 1436.

(29) Homeny, J.; Buckley, M. M. *Materials Lett.* **1990**, *9*, 443.

(30) Roberts, R. H.; Ramsey, J. A. *J. Electron Spectrosc. Relat. Phenom.* **1990**, *52*, 185.

(31) MacLaren, J. M.; Pendry, J. B.; Rous, P. J.; Saldin, D. K.; Somorjai, G. A.; Van Hove, M. A.; Vvedensky, D. D. *Surface Crystallographic Information Service: A Handbook of Surface Structures*; D. Reidel Publishing Company: Dordrecht, 1987.

(32) Sondericker, D.; Jona, F.; Marcus, P. M. *Phys. Rev. B* **1986**, *34*, 6770.

(33) Franchy, R.; So, S. K.; Gaßmann, P. *Surf. Rev. Lett.* **1996**, *3*, 1909.

(34) Isern, H.; Castro, G. R. *Surf. Sci.* **1989**, *211/212*, 865.

(35) Shen, Y.; O'Connor, D. J.; MacDonald, R. J. *Nuclear Instruments and Methods in Physics Research B* **1992**, *67*, 350.

(36) Lide, D. R. *CRC Handbook of Chemistry and Physics* 74 ed.; CRC Press: Boca Raton, 1994, p 9/123.

(37) Stirniman, M. J.; Li, W.; Sibener, S. J. *J. Chem. Phys.* **1995**, *103*, 451.

(38) Sautet, P. *Surf. Sci.* **1997**, *374*, 406.

(39) Tilinin, I. S.; Rose, M. K.; Dunphy, J. C.; Salmeron, M.; Van Hove, M. A. *Surf. Sci.* **1998**, *418*, 511.

(40) Fujita, K.; Watanabe, H.; Ichikawa, M. *J. Appl. Phys.* **1998**, *83*, 3638.

(41) Stöhr, J.; Johansson, L. I.; Brennan, S.; Hecht, M.; Miller, J. N. *Phys. Rev. B* **1980**, *22*, 4052.

CHAPTER 5

FORMATION OF A SULFUR ADLAYER ON $Ni_3Al(111)$

5.1. Introduction

Sulfur is a ubiquitous impurity in metals and alloys (1). Sulfur present on a metal or an alloy surface inhibits the formation of protective oxide scales on various substrates by occupying active sites that are otherwise available for oxygen chemisorption (2-4). In addition, interfacial sulfur induces grain-boundary embrittlement (1,5) and oxide degradation (6-8) at elevated temperatures.

Ni_3Al and other aluminides, in general, are technologically important materials (9) due to their resistance to high-temperature corrosion upon formation of a uniform aluminum oxide scale. The spallation of alumina scales at elevated temperatures (≥ 900°C) or upon thermal cycling has been associated with the presence of sulfur at the oxide-metal interface (10,11). The exact mechanism by which this occurs is not understood, and the interfacial chemistry of sulfur is therefore of technological as well as scientific interest. Previous studies the interfacial chemistry of sulfur at iron oxide-iron interfaces (8,12,13) have demonstrated that oxidation of clean and sulfur-modified metal substrates can provide useful model systems for a detailed study of the sulfur-induced disintegration of oxide scales. Studies in UHV have demonstrated that well-ordered, ultrathin films of γ'-Al_2O_3 can be prepared at 700-1200 K on various single-crystal Ni-Al alloy substrates (14,15). The ability to form ultrathin, highly ordered aluminum oxide

films makes possible a detailed investigation of oxide-metal interfacial chemistry using a variety of surface science techniques.

As a first step in investigating the effects of sulfur on alumina-aluminide interactions, we have conducted experiments in UHV to study the formation of a sulfur adlayer on $Ni_3Al(111)$. A study of the adsorption of sulfur on $Ni_3Al(111)$ is also interesting in view of the fact that a relatively large number of ordered overlayer structures is observed for varying sulfur coverages on different single-crystal substrates (16-24). On Ni(111), sulfur adsorption at low concentration levels produces LEED patterns with simple unit meshes, like the p(2×2) [at a sulfur coverage (θ_S) ≤ 0.25 ML] (25), and ($\sqrt{3}\times\sqrt{3}$)*R*30° (at $\theta_S \cong 0.33$ ML) (25). In these ordered structures, sulfur preferentially resides in three-fold fcc hollow sites on the Ni(111) surface (26,27). Adsorption of 0.4 ML sulfur on Ni(111) produces a ($5\sqrt{3}\times2$) LEED pattern (25,28), in which the first nickel layer is reconstructed into a (100)-like surface, in order to accommodate sulfur in four-fold coordinate sites (27). More complex and moiré-type LEED patterns were observed (28) at $\theta_S \geq 0.4$ ML, due to reorientation of the Ni(111) surface, and subsequent sulfide formation. In contrast to the commensurate overlayer structures formed by sulfur on Ni(111) (25,28), an incommensurate, two-dimensional 'surface sulfide' is observed after H_2S adsorption on Al(111) at 350-570 K (29,30). Only one report regarding the interactions of sulfur with Ni-Al alloys (18) is available in the literature. In the case of S/NiAl(111)(1×1), vibrational loss data indicated that the binding of sulfur in three-fold fcc sites is energetically favored (18). In addition, the surface of NiAl(111) [body centered cubic (bcc) lattice, with alternating aluminum and nickel layers) was preferentially nickel terminated in the presence of sulfur (18). In the

case of $Ni_3Al(111)$, since the surface structure consists of both nickel and aluminum atoms in a (2×2) arrangement (14), reaction with H_2S could lead to the binding of sulfur with either nickel or aluminum atoms in the surface, or with both. In this chapter, we summarize the AES and LEED results for the formation of an ordered sulfur adlayer on $Ni_3Al(111)$. A (2×2)-S adlayer with a sulfur coverage corresponding to 17.5-23 % of a monolayer (on an S/Ni atomic ratio basis) is formed by H_2S chemisorption on $Ni_3Al(111)$, followed by annealing to ~ 1100 K.

5.2. Experimental

Experiments were carried out in an Omicron UHV-STM/AFM chamber that has been described in Section 2.2 (31). The chamber is equipped with facilities for Auger, reverse-view LEED and STM/AFM (atomic force microscopy) measurements, as well as ion bombardment and gas dosing. The base pressure of 5×10^{-11} Torr after bake-out is maintained by a 100 l s^{-1} ion pump and a titanium sublimation pump.

Auger measurements were performed using a single-pass cylindrical mirror analyzer with a coaxial electron gun (Physical Electronics). Auger spectra were excited with a 3 keV electron beam. Data were acquired in the integral mode [N(E)] using RBS software (32), and then smoothed and differentiated [dN(E)/dE] using a Savitzky-Golay program in Microcal Origin 4.1 (33). In order to ensure consistent peak energies, the sample-to-analyzer distance was adjusted using the elastic peak at 3 keV (34). Surface ordering was checked by LEED. The four-grid retarding field analyzer for LEED measurements was calibrated using a Si(111)(7×7) sample. Lattice dimensions obtained by LEED are reported here with a precision of ± 0.1 Å.

The $Ni_3Al(111)$ sample (purchased from MaTeck) had a diameter of 10 mm, and a thickness of 0.5 mm. The sample was polished on one side with an orientation miscut angle < 0.25°. The sample was spot-welded to a tantalum sample plate and placed on an *x-y-z* manipulator. Sample heating was performed resistively, and temperature was measured using a *K*-type Cr-Al thermocouple attached to a sample clip approximately 5 mm away from the sample.

The $Ni_3Al(111)$ sample was cleaned in UHV by repeated cycles of Ar^+ bombardment (1 keV at $P_{Ar} = 5 \times 10^{-6}$ mbar) and subsequent annealing at ~ 1100 K. The cleanliness of the sample was verified by the absence of impurities in the Auger spectrum, and by the formation of a sharp (2×2) LEED pattern characteristic of the well-ordered $Ni_3Al(111)$ surface (14). H_2S (99.5% pure), purchased from Matheson, was admitted into the chamber via a stainless steel doser tube attached to a manual leak valve. Exposures expressed in Langmuir (1 L = 10^{-6} Torr-sec) have not been corrected for ion-gauge sensitivity, flux to the sample or effects of directional dosing. Pressure was measured using a nude ion gauge mounted out of line-of-sight to the sample.

Atomic concentrations were calculated by substituting the appropriate Auger peak-to-peak heights (pph) and published/calculated atomic sensitivity factors (35) into Eq. (5-1) (36),

$$\frac{X_A}{X_B} = F_{AB}^{A} \times \left(\frac{I_A}{I_A^{\infty}} \right) \Big/ \left(\frac{I_B}{I_B^{\infty}} \right) \qquad (5\text{-}1)$$

where X_A, I_A and I_A^{∞}, respectively, represent the molar concentration, Auger peak-to-peak height (pph) and atomic sensitivity factor of element A. The Auger electron matrix factor F_{AB}^{A} for aluminum in Ni_3Al has been calculated to be ~ 0.7 (37). An $Al_{(1396)}/Ni_{(848)}$

atomic ratio of ~ 0.45 for the clean, well-ordered $Ni_3Al(111)(2\times2)$ therefore corresponds to ~ 25% concentration of aluminum atoms in the surface (Chapter 4). The error in the intensity ratios due to variations in electron flux from the analyzer has been determined to be ~ 7%. From the mean free paths (λ) of the elements [λ of $S_{(152)}$ = 6.75 Å (38), λ of $Ni_{(848)}$ in Ni_3Al = 18.55 Å (38)], the coverage of sulfur (θ_S) relative to nickel was calculated according to Eq. (5-2) (36):

$$\frac{\theta_S\{1-\exp[-a_S/\lambda_S(E_S)]\}}{(1-\theta_S)\{1-\exp[-a_S/\lambda_S(E_{Ni})]\}}=\left(\frac{I_S}{I_S^{\infty}}\right)\Big/\left(\frac{I_{Ni}}{I_{Ni}^{\infty}}\right) \qquad (5\text{-}2)$$

In Eq. (5-2), E_A represents the Auger electron energy for element A, and a_S is the covalent diameter of the sulfur atom ($\cong$ 2.04 Å). In addition, the $Al_{(68)}$ and $Ni_{(61)}$ peaks, which are sensitive to changes in electronic states due to sulfide formation (29,30,39), were monitored. The lineshape of the $S_{(152)}$ signal was also monitored during exposure to H_2S and thermal treatment in order to detect any bulk/surface sulfide formation (39).

5.3. Results

The clean $Ni_3Al(111)(2\times2)$ surface was successively exposed to H_2S (P_{H_2S} = 1×10^{-8} Torr) at room temperature and the Auger spectrum of the surface was recorded after each exposure. The plot of the relative sulfur Auger intensity vs. H_2S exposure presented in Fig. 5.1a reveals that saturation is attained at ~ 6 L, when the $S_{(152)}/Ni_{(848)}$ atomic ratio $\cong 0.89 \pm 0.07$. Using Eq. (5-2), this atomic ratio corresponds to a sulfur coverage of ~ 26% relative to nickel. The $Al_{(1396)}/Ni_{(848)}$ atomic ratio (not shown) remained constant within experimental error, demonstrating the absence of aluminum enrichment in the

surface during reaction with H_2S at ~ 300 K. A diffuse (2×2) LEED pattern with intense background (not shown) was observed after exposure to ~ 20 L H_2S, indicating that sulfur adsorption at room temperature leads to a disordered surface.

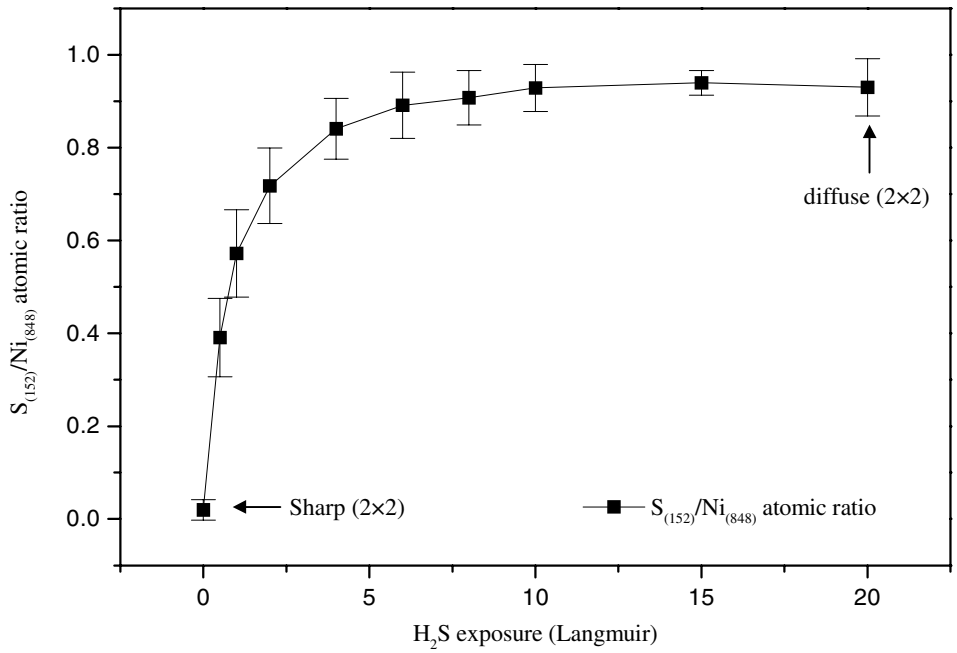

Fig. 5.1 (a). Relative sulfur Auger intensity as a function of H_2S exposure at 300 K.

The sulfur-covered surface produced by exposure of $Ni_3Al(111)$ to ~ 10 L H_2S at ~ 300 K was annealed progressively up to ~ 1100 K in UHV (for 15 minutes at each temperature). A plot of $S_{(152)}/Ni_{(848)}$ atomic ratio versus annealing temperature (Fig. 5.1b) shows a steady decline in the ratio at temperatures > 800 K. In contrast, the $Al_{(1396)}/Ni_{(848)}$ atomic ratio (not shown) was unaffected in the temperature range of 300-1100 K. Since the equilibrium concentration of the aluminum atoms in the clean $Ni_3Al(111)$ surface is ~ 25% (Chapter 4), any enrichment of aluminum in the surface

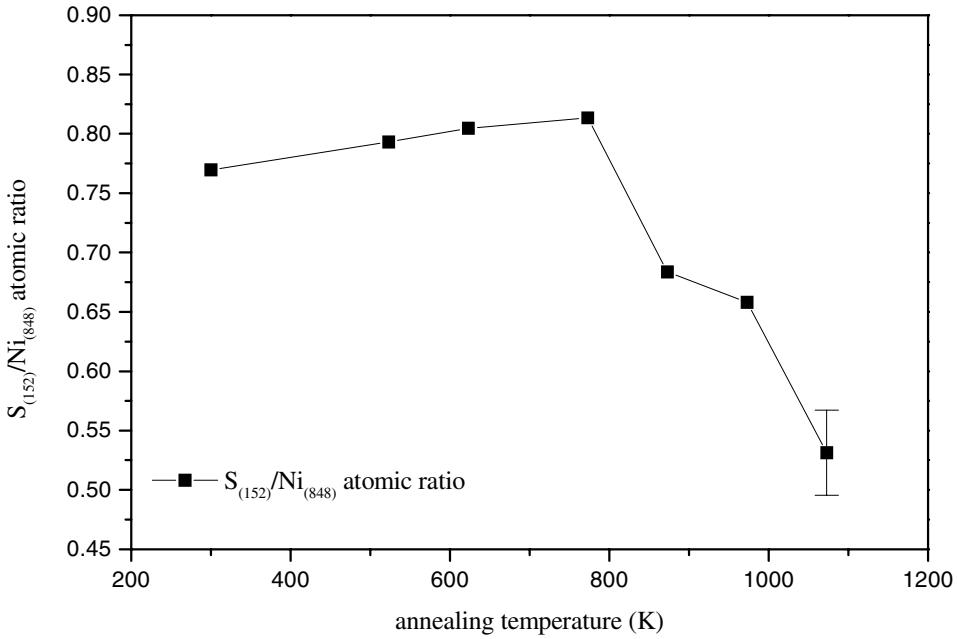

Fig. 5.1 (b). Effect of thermal treatment on $S_{(152)}/Ni_{(848)}$ atomic ratio following exposure to 10 L H_2S at 300 K.

region would be accompanied by an increase in this concentration, as reported in Chapter 4. The fact that the $Al_{(1396)}/Ni_{(848)}$ atomic ratio remains constant throughout the temperature range of 300 – 1100 K on the sulfur-covered $Ni_3Al(111)$ surface rules out any aluminum enrichment of the surface region during annealing. After annealing to ~ 1100 K, the $S_{(152)}/Ni_{(848)}$ atomic ratio was observed to decrease to 0.53 ± 0.04, which is equivalent to a sulfur coverage of ~ 17.5 % with respect to nickel. The corresponding LEED pattern was a sharp (2×2) (not shown). The lattice constant derived from LEED measurements (= 5.03 ± 0.1 Å) is consistent with that of the clean $Ni_3Al(111)(2\times2)$ surface (14). Adsorption of excess (~ 20 L) H_2S on the clean $Ni_3Al(111)$ surface at ~ 300 K, followed by annealing to ~ 1100 K also produced the same LEED pattern. These

results are in agreement with the adsorption of H_2S on various metallic substrates (16), where the formation of a (2×2) pattern was observed at sulfur coverages ≤ 0.25 ML.

At higher coverages ($\theta_S \geq 0.3$ ML), several sulfur-induced overlayer structures have been reported for various metal substrates (16-24). In order to obtain a higher coverage of sulfur, the $Ni_3Al(111)$ surface was exposed to H_2S ($P_{H_2S} = 1 \times 10^{-8}$ Torr) at ~ 800 K (temperature at which $S_{(152)}/Ni_{(848)}$ atomic ratio is maximum; Fig. 5.1b). The observed saturation coverage of $\theta_S = 0.3$ ML (relative to nickel) corresponds to an $S_{(152)}/Ni_{(848)}$ atomic ratio of 1.09 ± 0.07. The LEED pattern of the surface formed by exposure to H_2S at ~ 800 K (Fig. 5.2a) reveals considerable streaking of the spots in all directions relative to the (2×2) structure. Annealing for longer period of time at ~ 800 K did not yield a clearer LEED pattern**,** indicating a certain degree of disordering when the $Ni_3Al(111)$ surface is exposed to H_2S at this temperature. Upon flash annealing to ~ 1100 K, however, the diffuse LEED pattern displayed in Fig. 5.2a was transformed into a (2×2) pattern with significantly reduced streaking of the LEED spots (Fig. 5.2b). This transformation was accompanied by a decrease in the atomic ratio of $S_{(152)}/Ni_{(848)}$ from 1.09 ± 0.07 to 0.73. The LEED pattern displayed in Fig. 5.2a was not observed when the sulfur-covered $Ni_3Al(111)$ surface prepared at room temperature was annealed to ~ 800 K. No appreciable changes in the $Al_{(1396)}/Ni_{(848)}$ atomic ratio (not shown) were noted either during H_2S exposure at 800 K, or after flash annealing to 1100 K, indicating that the surface concentration of aluminum remained constant.

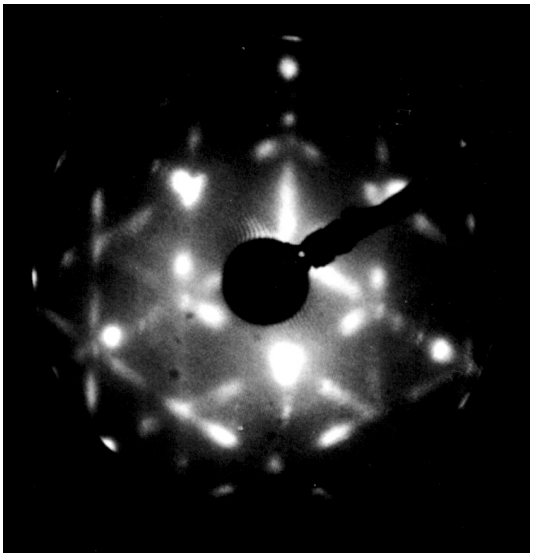

(a)

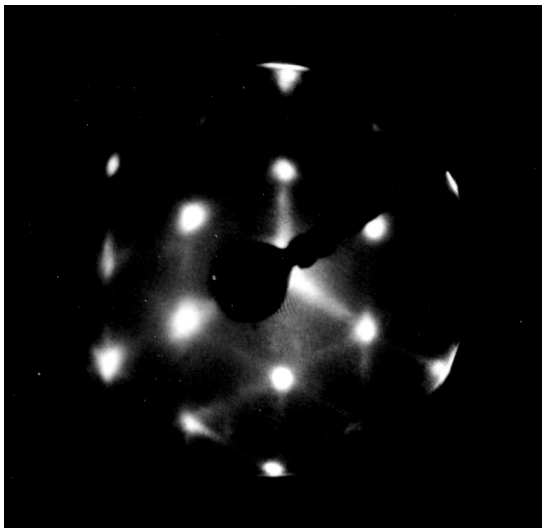

(b)

Fig. 5.2. LEED patterns of the $Ni_3Al(111)$ surface (a) after H_2S uptake at 800 K (E = 65.8 eV); (b) after flash annealing the diffuse LEED pattern in (a) to ~ 1100 K (E = 65.1 eV).

No changes indicative of the formation of Al^{3+} (40,41) were observed in the lineshape of the $Al_{(68)}$ peak (not shown) either during H_2S exposure, or after annealing to ~ 1100 K. Studies of the sulfidation of Al(111) (29,30) have reported a shift of the low-energy aluminum peak from 68 eV to 63 eV as a result of Al_2S_3 formation. Similarly, the formation of bulk Ni_3S_2/NiS, or 'surface' nickel sulfide is characterized by the appearance of a shoulder in the Ni($M_{23}VV$) peak (39). In case of the $Ni_3Al(111)$ sample, such slight shifts signifying sulfide formation would not be observed in the Auger spectra, due to the overlap of the $Ni_{(61)}$ and the $Al_{(68)}$ peaks (42). The S(LVV) transition (not shown), however, did not exhibit any bifurcation characteristic of a bulk/surface sulfide formation (39).

5.4. Discussion

The room-temperature uptake curve for H_2S on the $Ni_3Al(111)$ surface (Fig. 5.1a) reveals a high sticking probability up to exposures of 0.5-1 L at $P_{H_2S} = 1 \times 10^{-8}$ Torr. In order to estimate the initial sticking coefficient for H_2S on the $Ni_3Al(111)$ surface, we plotted the surface coverage of sulfur [θ_S; calculated using Eq. (5-2)] as a function of H_2S exposure up to 1 L (plot not shown). The exposure is dependent upon the flux F of the incident H_2S molecules, the time of exposure t, and the concentration of atoms in the $Ni_3Al(111)$ surface [$N \cong 1 \times 10^{15}$ atoms cm^{-2} by convention (43)], according to the equation

$$\text{Exposure} = \frac{Ft}{N} \qquad (5\text{-}3)$$

In Eq. (5-3), the flux of the H_2S molecules striking the $Ni_3Al(111)$ surface is given by (43)

$$F = 3.51\times10^{22}\left[\frac{P}{\sqrt{MT}}\right] \qquad (5\text{-}4)$$

where P is the partial pressure of H_2S (= 1×10^{-8} Torr), M is its molecular weight in g mole^{-1}, and T is the reaction temperature (300 K). From the plot of H_2S exposure versus sulfur coverage (θ_S), the initial sticking coefficient was estimated to be ~ 0.65.

The clean $Ni_3Al(111)$ surface exhibits a sharp (2×2) LEED pattern, indicative of the ordered arrangement of aluminum atoms in the surface (14). A (2×2) pattern (not shown) was observed after the $Ni_3Al(111)$ surface was exposed to H_2S at ~ 300 K and subsequently annealed at ~ 1100 K for 20 minutes. The corresponding sulfur coverage, derived from Auger measurements, is ~ 0.175 ML (on an S/Ni atomic ratio basis). A diffuse LEED pattern with streaks (Fig. 5.2a) corresponding to θ_S = 0.3 ML was observed after exposure to H_2S at ~ 800 K. The formation of the diffuse pattern with streaks (Fig. 5.2a) indicates a certain degree of disordering when the $Ni_3Al(111)$ surface is exposed to H_2S at ~ 800 K. Upon flash annealing to ~ 1100 K, the diffuse LEED pattern was converted to a (2×2) structure (Fig. 5.2b). Since the $Al_{(1396)}/Ni_{(848)}$ atomic ratio remained constant (within experimental error) both during H_2S exposure at ~ 800 K, and after flash annealing to ~ 1100 K, the changes observed in the LEED pattern are not attributable to aluminum or nickel surface segregation. Whether the disorder observed upon H_2S exposure at 800 K reflects only disorder of the sulfur adatoms, or also involves disordering of the $Ni_3Al(111)$ surface layer, cannot be definitively determined from the present data.

The transformation of the diffuse LEED pattern represented in Fig. 5.2a to the (2×2) ordered structure in Fig. 5.2b upon flash annealing is coincident with the decrease in the sulfur coverage to ~ 0.23 ML relative to nickel. Since the decrease in the sulfur coverage indicates the removal of sulfur from the surface, the change in the LEED pattern shown in Fig. 5.2 cannot be due to the thermally induced migration of sulfur atoms to more energetically favorable adsorption sites in the surface. It is not possible, however, to make a definite determination of the pathway of the removal of some of the sulfur atoms upon annealing the sulfur-covered Ni_3Al surface at ~ 1100 K, because no residual gas measurements were carried out to monitor the desorption of sulfur-containing species from the surface. Furthermore, the decrease in the sulfur coverage can be attributed either to desorption, or diffusion into the bulk or both.

With the exception of the formation of an incommensurate, two-dimensional 'surface sulfide' by the reaction of H_2S with Al(111) at 350-570 K (29,30), sulfur preferentially occupies three-fold and four-fold hollow sites on most metal/alloy substrates (16,18,25,27,44), as shown by LEED, HREELS, and LEIS experiments. At coverages ≤ 0.25 ML, sulfur adsorbs in the three-fold fcc hollow sites (sites with third layer atoms beneath) in the case of fcc metals [hcp hollow sites (sites with second layer atoms beneath) in case of hexagonal close packed (hcp) metals] (16), where its binding is most energetically favored. When the sulfur coverage exceeds 0.3 ML, sulfur atoms occupy neighboring fcc sites, leading to repulsion between the atoms (16). The repulsive interaction is relieved by occupancy of hcp hollow sites by the sulfur atoms (16). This was also observed by Franchy et al. in the case of S/NiAl(111)(1×1) (18), where HREELS spectra were characterized by two vibrational losses that indicate sulfur

adsorption in two different three-fold hollow sites (fcc and hcp). Since the intensity of the energy-loss peak for the fcc site increased relative to that of the hcp site at higher temperatures, these authors concluded that sulfur preferentially occupies fcc three-fold nickel sites in (1×1)-S/NiAl(111) (18).

Although the observed LEED pattern for the S/Ni_3Al(111) ($\theta_S \leq 0.25$ ML) is indicative of a (2×2) surface structure, it is not possible to unambiguously assign the observed LEED spots to either sulfur or aluminum, since the lattice dimension calculated from the pattern is consistent with the Al-Al separation in the clean Ni_3Al(111) surface . The absence of 'extra adsorbate spots' in the LEED pattern for the sulfur-covered Ni_3Al(111) surface at ~ 1100 K (Fig. 5.2b), however, indicates that the sulfur overlayer assumes a lattice arrangement consistent with the (2×2) structure. From the LEED pattern we could not rule out a (1×1) lattice structure, because the first-order spots of the (1×1)-S structure would coincide with the second-order spots of the clean Ni_3Al(111). AES measurements, however, reveal a sulfur coverage (< 0.25 ML) that is consistent with the (2×2) but not with the (1×1) lattice arrangement. The (2×2)-S overlayer ordering indicates that sulfur binds to three-fold hollow sites (fcc or hcp) or aluminum on-top sites. Without quantitative (I/V) LEED calculations, one cannot establish nuclear positions with the use of the LEED pattern alone. For this reason, we are unable to unequivocally assign the adsorption sites for the sulfur overlayer. Previous studies regarding sulfur adsorption on most metal/alloy substrates (16,18,25,27,44), however, have demonstrated that sulfur atoms preferentially adsorb on high coordination sites. Furthermore, Yoon et al. have shown that binding of sulfur in three-fold fcc sites is

energetically favored (16). In the case of S/NiAl(111) system, Franchy et al. (18) observed that sulfur preferentially occupies fcc three-fold nickel sites in (1×1)-S/NiAl(111). We therefore propose that the (2×2)-S adlayer on $Ni_3Al(111)$ ($\theta_S \leq 0.25$ ML) consists of sulfur occupying three-fold fcc hollow sites on the $Ni_3Al(111)$.

5.5. Summary and Conclusions

In summary, the adsorption of H_2S on $Ni_3Al(111)$ at two different temperatures, followed by annealing to ~ 1100 K results in the formation of a (2×2)-S covered surface, with sulfur coverages in the range of 17.5 – 23 %. No sulfide formation is detectable from the Auger lineshape of the sulfur signal. The concentration of aluminum in the sulfur-covered surface is found to correspond to ~ 25%, as in case of the clean $Ni_3Al(111)$ surface.

5.6. Chapter References

(1) Oudar, J. *Mater. Sci. Eng.* **1980**, *42*, 101.

(2) Lin, J.-S.; Ekstrom, B.; Addepalli, S. G.; Cabibil, H.; Kelber, J. A. *Langmuir* **1998**, *14*, 4843.

(3) Liu, J.; Lu, J. P.; Chu, P. W.; Blakely, J. M. *J. Vac. Sci. Technol.* **1992**, *10*, 2355.

(4) Lad, R. J.; Schrott, A. G.; Blakely, J. M. *J. Vac. Sci. Technol. A* **1985**, *3*, 1282.

(5) Seah, M. P. in *Practical Surface Analysis: Auger and X-ray Photoelectron Spectroscopy*; 2 ed.; Briggs, D. and Seah, M. P., Eds.; Wiley: New York, 1990; Vol. 1, p 311.

(6) Hou, P. Y.; Stringer, J. *Oxid. Met.* **1992**, *38*, 323.

(7) Stott, F. H. *Rep. Prog. Phys.* **1987**, *50*, 861.

(8) Kelber, J. A.; Addepalli, S. G.; Lin, J.-S.; Cabibil, H. in *High Temperature Corrosion and Materials Chemistry*; Hou, P. Y., McNallan, M. J., Oltra, R., Opila, E. J. and Shores, D. A., Eds.; The Electrochemical Society, Inc.: San Diego, CA, 1998; Vol. 98-99, p 190.

(9) Meier, G. H. *Mater. Corros.* **1996**, *47*, 595.

(10) Hou, P. Y.; Wang, Z.; Prüßner, K.; Alexander, K. B.; Brown, I. G. in *3rd International Conference on Microscopy of Oxidation*; Hou, P. Y., Wang, Z., Prüßner, K., Alexander, K. B. and Brown, I. G., Eds.; The Institute of Materials: Trinity Hall, Cambridge, UK, 1996, p 1.

(11) Smialek, J. L.; Jayne, D. T.; Schaeffer, J. C.; Murphy, W. H. *Thin Solid Films* **1994**, *253*, 285.

(12) Cabibil, H.; Kelber, J. A. *Surf. Sci.* **1995**, *329*, 101.

(13) Cabibil, H.; Kelber, J. A. *Surf. Sci.* **1997**, *373*, 257.

(14) Becker, C.; Kandler, J.; Raaf, H.; Linke, R.; Pelster, T.; Dräger, M.; Tanemura, M.; Wandelt, K. *J. Vac. Sci. Technol. A* **1998**, *16*, 1000.

(15) Jaeger, R. M.; Kuhlenbeck, H.; Freund, H.-J.; Wuttig, M.; Hoffmann, W.; Franchy, R.; Ibach, H. *Surf. Sci.* **1991**, *259*, 235.

(16) Yoon, H. A.; Salmeron, M.; Somorjai, G. A. *Surf. Sci.* **1998**, *395*, 269.

(17) Cabibil, H.; Lin, J.-S.; Kelber, J. A. *J. Vac. Sci. Technol. B* **1998**, *16*, 30.

(18) Franchy, R.; Wuttig, M.; Ibach, H. *Surf. Sci.* **1987**, *189/190*, 438.

(19) Dunphy, J. C.; Sautet, P.; Ogletree, D. F.; Salmeron, M. B. *J. Vac. Sci. Technol. A* **1993**, *11*, 1975.

(20) Colaianni, M. L.; Chorkendorff, I. *Phys. Rev. B* **1994**, *50*, 8798.

(21) Partridge, A.; Tatlock, G. J.; Leibsle, F. M.; Flipse, C. F. J.; Hoermandinger, G.; Pendry, J. B. *Phys. Rev. B* **1993**, *48*, 8267.

(22) Parker, T. M.; Condon, N. G.; Lindsay, R.; Thornton, G.; Leibsle, F. M. *Surf. Rev. Lett.* **1994**, *1*, 705.

(23) Ruan, L.; Stensgaard, I.; Lægsgaard, E.; Besenbacher, F. *Surf. Sci.* **1993**, *296*, 275.

(24) Nien, C.-H.; Abdelrehim, I. M.; Madey, T. E. *Surf. Rev. Lett.* **1999**, *6*, 77.

(25) Perdereau, M.; Oudar, J. *Surf. Sci.* **1970**, *20*, 80.

(26) Kitajima, Y.; Yagi, S.; Yokoyama, T.; Imanishi, A.; Takenaka, S.; Ohta, T. *Surf. Sci.* **1994**, *320*, L89.

(27) Mullins, D. R.; Huntley, D. R.; Overbury, S. H. *Surf. Sci. Lett.* **1995**, *323*, L287.

(28) Edmonds, T.; McCarroll, J. J.; Pitkethly, R. C. *J. Vac. Sci. Technol.* **1971**, *8*, 68.

(29) Wiederholt, T.; Brune, H.; Wintterlin, J.; Behm, R. J.; Ertl, G. *Surf. Sci.* **1995**, *324*, 91.

(30) Jacobi, K.; Muschwitz, C. V.; Kambe, K. *Surf. Sci.* **1980**, *93*, 310.

(31) Lin, J.-S.; Cabibil, H.; Ekstrom, B.; Kelber, J. A. *Surf. Sci.* **1997**, *371*, 337.

(32) RBD Enterprises: Bend, OR 97702.

(33) Microcal Software, Inc.: Northampton, MA 01060.

(34) Riviere, J. C. in *Practical Surface Analysis: Auger and X-ray Photoelectron Spectroscopy*; 2 ed.; Briggs, D. and Seah, M. P., Eds.; Wiley: New York, 1979; Vol. 1, p 19.

(35) Davis, L. E.; MacDonald, N. C.; Palmberg, P. W.; Raich, G. E.; Weber, R. E. *Handbook of Auger Electron Spectroscopy*; 2 ed.; Physical Electronics Industries, Inc.: Eden Prairie, 1979.

(36) Seah, M. P. in *Practical Surface Analysis: Auger and X-ray Photoelectron Spectroscopy*; 2 ed.; Briggs, D. and Seah, M. P., Eds.; Wiley: New York, 1990; Vol. 1, p 201.

(37) Gassmann, P.; Franchy, R.; Ibach, H. *Surf. Sci.* **1994**, *319*, 95.

(38) Powell, C. J.; Jablonski, A.; Tilinin, I. S.; Tanuma, S.; Penn, D. R. *J. Electron Spectrosc. Relat. Phenom.* **1999**, *98-99*, 1.

(39) Windawi, H.; Katzer, J. R. *J. Vac. Sci. Technol.* **1979**, *16*, 497.

(40) Chen, J. G.; Crowell, J. E.; Yates, J. T., Jr. *Phys. Rev. B* **1986**, *33*, 1436.

(41) Homeny, J.; Buckley, M. M. *Materials Lett.* **1990**, *9*, 443.

(42) Sondericker, D.; Jona, F.; Moruzzi, V. J.; Marcus, P. M. *Solid State Communications* **1985**, *53*, 175.

(43) Somorjai, G. A. *Introduction of Surface Chemistry and Catalysis*; John Wiley & Sons, Inc.: New York, 1994.

(44) Arabczyk, W.; Müssig, H.-J.; Storbeck, F. *Phys. Status Solidi A* **1979**, *55*, 437.

CHAPTER 6

INTERACTIONS AT THE Al_2O_3-S-Ni_3Al(111) INTERFACE AT ELEVATED TEMPERATURES: ORDERING OF Al_2O_3 ON A SULFUR-MODIFIED SUBSTRATE

6.1. Introduction

Aluminides and other ternary alloys containing aluminum are frequently used in aggressive, corrosive environments, due their ability to form high-temperature corrosion-resistant aluminum oxide scales (1). The presence of impurities, especially sulfur, at oxide-substrate interfaces, has been associated with oxide spallation from various substrates at elevated temperatures (2,3), and can critically impact technological applications such as aerospace, power plant operation, the fabrication of composite materials, catalysis and microelectronics. Studies on single-crystal alumina/Ni(poly) (4) and polycrystalline alloy/alumina (2,3,5,6) substrates have demonstrated that sulfur segregates to the oxide-substrate interface at elevated temperatures and weakens the metal-oxide bond. The deleterious effects of sulfur have also been observed in chromia- (6) and iron oxide- (7-9) forming systems. Due to its implications for the performance of various alloys and steels, sulfur interface chemistry is a topic of technological as well as scientific interest. The exact mechanism of sulfur-induced oxide spallation, however, is still unclear, and has been the subject of long-standing debate (6,10,11).

In an effort to elucidate sulfur interactions with metal-oxide bonds, studies have been carried out on corresponding model interfaces prepared on iron (7-9) under ultra-high vacuum (UHV) conditions. These studies have demonstrated that chemical

reactions which are highly endothermic based on bulk bond dissociation enthalpies, nevertheless occur at surfaces or interfaces, due to two reasons: [1] interfacial Fe-S bonds have electronic structures and reactivities quite different from those found in corresponding bulk phases (12), and [2] the migration of reaction products into the bulk, with subsequent alloying, may provide a powerful driving force for the reaction (Chapter 3). In order to ascertain a microscopic mechanism for the destabilization of alumina scales on aluminides and other aluminum-containing alloys, we prepared alumina films on clean and sulfur-modified $Ni_3Al(111)$ substrates in UHV. $Ni_3Al(111)$ and other single-crystal aluminides (Ni-Al alloys) can form highly ordered, ultrathin (< 10 Å) γ'-Al_2O_3 films upon oxidation at 700-1200 K in UHV (13,14). This property makes them excellent candidates for high-temperature corrosion studies.

A (2×2)-S modified $Ni_3Al(111)$ surface with a sulfur coverage ≤ 25% of a monolayer (on a S/Ni atomic ratio basis) was prepared by reaction with H_2S and post-annealing, as described in Chapter 5. In this chapter, we discuss the LEED, AES and STM results of the growth, morphology and thermal stability of the oxide on the (2×2)-S covered $Ni_3Al(111)$ surface. The results demonstrate that although sulfur significantly alters the oxidation rate and the oxide morphology at room temperature, it does not hinder the formation of an ordered γ'-Al_2O_3 overlayer on the $Ni_3Al(111)$ substrate at elevated temperatures. The oxide formed on the sulfur-covered $Ni_3Al(111)$ surface is stable up to at least 1100 K. Annealing from ~ 300 K to ~ 1100 K results in the segregation of aluminum from the bulk, as evidenced by an increase in the $Al_{(1396)}/Ni_{(848)}$ atomic ratio, and the appearance of the metallic aluminum transition in the Auger spectra. In contrast to previously observed cases (7-9,15,16) of sulfur-induced instability of

oxides, the AES data indicate the removal of sulfur from the Al_2O_3-$Ni_3Al(111)$ interface upon annealing.

6.2. Experimental

Experiments were carried out in an Omicron ultrahigh vacuum chamber (17) (base pressure < 5×10^{-11} Torr) equipped with an STM/AFM stage, a four-grid LEED system, and a single-pass cylindrical mirror analyzer (CMA) for AES measurements. The excitation source for AES was an electron gun mounted coaxially with the analyzer, and operated at a beam voltage of 3 keV. STM topographies were recorded at room temperature by applying a positive bias voltage (U_{gap} = + 0.1 V to +1.5 V) to the sample, while maintaining a constant feedback current, typically in the range of 0.1 – 1.5 nA. In addition, I/V spectroscopy was obtained to distinguish between metallic and oxidized surfaces. STM tips were prepared by electrochemically etching a polycrystalline tungsten wire (diameter 0.01 in.). The STM images presented in this paper have been processed to reduce linear background along the *x*- and *y*- directions of the scan and high frequency noise.

The $Ni_3Al(111)$ sample described in Chapters 4 and 5 was cleaned by repeated cycles of Ar^+ sputtering and subsequent annealing at ~ 1100 K, until no impurities were observed in the Auger spectrum. The clean, well-ordered $Ni_3Al(111)$ surface is characterized by a sharp (2×2) LEED pattern, with an Al-Al nearest-neighbor distance of 4.9 ± 0.1 Å (Chapter 4). A (2×2)-S adlayer ($\theta_S \leq 0.25$) was prepared by reacting the clean $Ni_3Al(111)$ surface with ~ 20 L H_2S (99.5% pure, purchased from Matheson) at ~

300 K, followed by annealing at ~ 1100 K for 20 minutes (Chapter 5). Sulfur coverage (θ_S) was calculated from Eq. (6-1):

$$\frac{\theta_S\{1-\exp[-a_S/\lambda_S(E_S)]\}}{(1-\theta_S)\{1-\exp[-a_S/\lambda_S(E_{Ni})]\}} = \left(\frac{I_S}{I_S^\infty}\right) \Big/ \left(\frac{I_{Ni}}{I_{Ni}^\infty}\right) \qquad (6\text{-}1)$$

where λ_S and λ_{Ni} correspond to the mean free paths of the $S_{(152)}$ and $Ni_{(848)}$ Auger transitions, respectively [λ_S = 6.75 Å, λ_{Ni} = 18.55 Å (18)]. E_A represents the Auger electron energy for element A, and a_S is the covalent diameter of the sulfur atom (≅ 2.04 Å). I_A and I_A^∞ indicate, respectively, the Auger peak-to-peak height intensity and the atomic sensitivity factor for element A. The sulfur-modified surface was oxidized at room temperature by admitting O_2 (99.997% pure, purchased from Matheson) into the chamber by a manual leak valve (P_{O_2} = 1×10^{-7} - 1×10^{-6} Torr). Oxidation experiments were also performed on the sulfur-free $Ni_3Al(111)$ surface (control) for comparison. Pressure was measured with a nude ion gauge mounted out of line-of-sight to the sample to minimize gauge-induced decomposition of the gases. Exposures are expressed in Langmuir (1 L = 10^{-6} Torr-sec), and have not been corrected for ion-gauge sensitivity, differences in flux to the sample or effects of directional dosing.

The percentage attenuation of the intensities of the various Auger peaks following oxidation was calculated according to:

$$\%\ \text{Attenuation} = \left[\frac{I_0 - I}{I_0}\right]\times 100 \qquad (6\text{-}2)$$

In Eq. (6-2), I_0 is the initial intensity of the Auger peak before oxidation, and I is the intensity following the oxidation experiment.

6.3. Results

6.3.1. Oxidation and oxide morphologies at ~ 300 K

The oxygen uptake curves ($O_{(510)}/Ni_{(848)}$ atomic ratio vs. O_2 exposure) of the room-temperature oxidation of the sulfur-free ($\theta_S = 0$) and (2×2)-S covered ($\theta_S \cong 0.175$) $Ni_3Al(111)$ surfaces are displayed in Fig. 6.1. The lineshapes of the Auger peaks near 60 eV as a function of O_2 exposure were compared for the initially clean and sulfur-covered $Ni_3Al(111)$ surfaces. These results are presented in Fig. 6.2. Saturation is attained after longer O_2 exposures (~ 2048 L) for the sulfur-covered surface, relative to the clean $Ni_3Al(111)$ surface (~ 256 L). The oxidation of the sulfur-free $Ni_3Al(111)$ surface (Fig. 6.2a) commences at exposures as low as ~ 2 L, as evidenced by the appearance of the Al^{3+} shoulder at 38 eV (19,20), while in case of the sulfur-covered Ni_3Al surface (Fig. 6.2b), at least ~ 32 L O_2 exposure is required before the onset of the Al^{3+} shoulder (38 eV) is observed. These results (Figs. 6.1 and 6.2) demonstrate that oxidation of the $Ni_3Al(111)$ surface at ~ 300 K is retarded in the presence of sulfur. Similar results have been published for the oxidation of Fe(111) (7,21), $Ni_{60}Fe_{40}(100)$ (22) and Ni(111) (23) surfaces precovered with sulfur. Although the rate of oxidation is much lower for the sulfur-covered $Ni_3Al(111)$ surface as evidenced by saturation at longer oxygen exposures (Fig. 6.1), the $O_{(510)}/Ni_{(848)}$ atomic ratio observed at saturation exposure to O_2 at 300 K is 0.69 ± 0.1, regardless of the presence or absence of sulfur on the surface. Thus, the final average thickness of the oxide film formed at room temperature does not change due to preadsorbed sulfur.

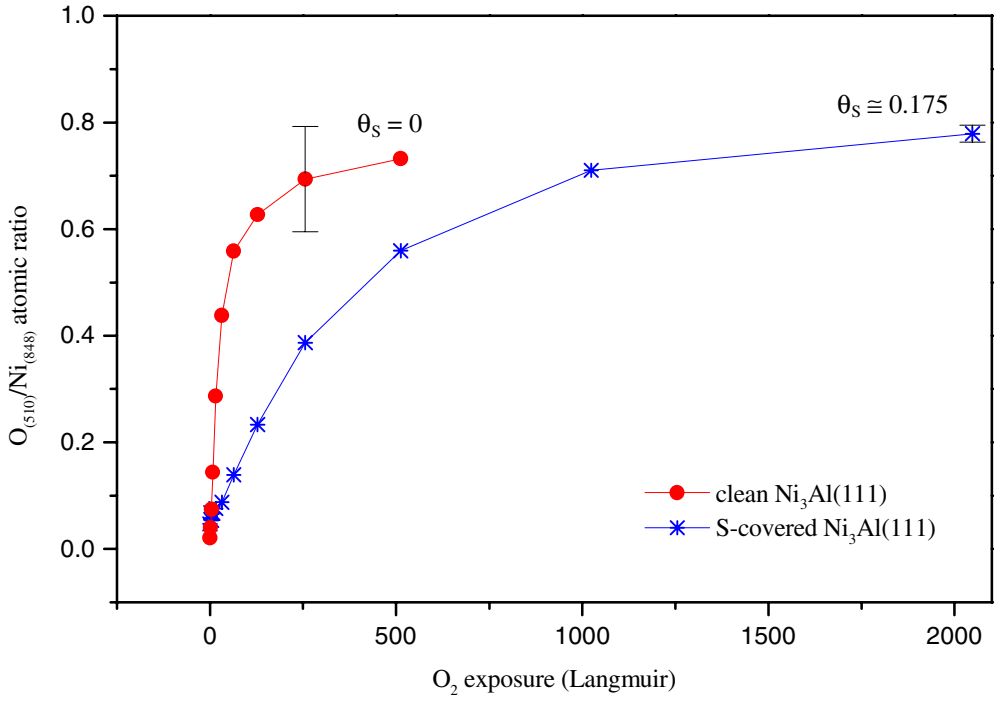

Fig. 6.1. Oxygen uptake curves ($O_{(510)}/Ni_{(848)}$ atomic ratio vs. O_2 exposure) for clean and (2×2)-S covered $Ni_3Al(111)$ surfaces at 300 K.

The variation in the $S_{(152)}/Ni_{(848)}$ atomic ratio with increasing O_2 exposure at 300 K is depicted in Fig. 6.3. An exponential decay in the $S_{(152)}/Ni_{(848)}$ atomic ratio with increasing oxygen exposure is accompanied by ~ 70% attenuation in the intensity of the $S_{(152)}$ peak. A plot of the $S_{(152)}/O_{(510)}$ atomic ratio vs. oxygen exposure (not shown) also reveals an exponential decrease, demonstrating oxide overgrowth. No prominent changes (24) were observed in the lineshape of the sulfur transition (not shown) during O_2 exposure.

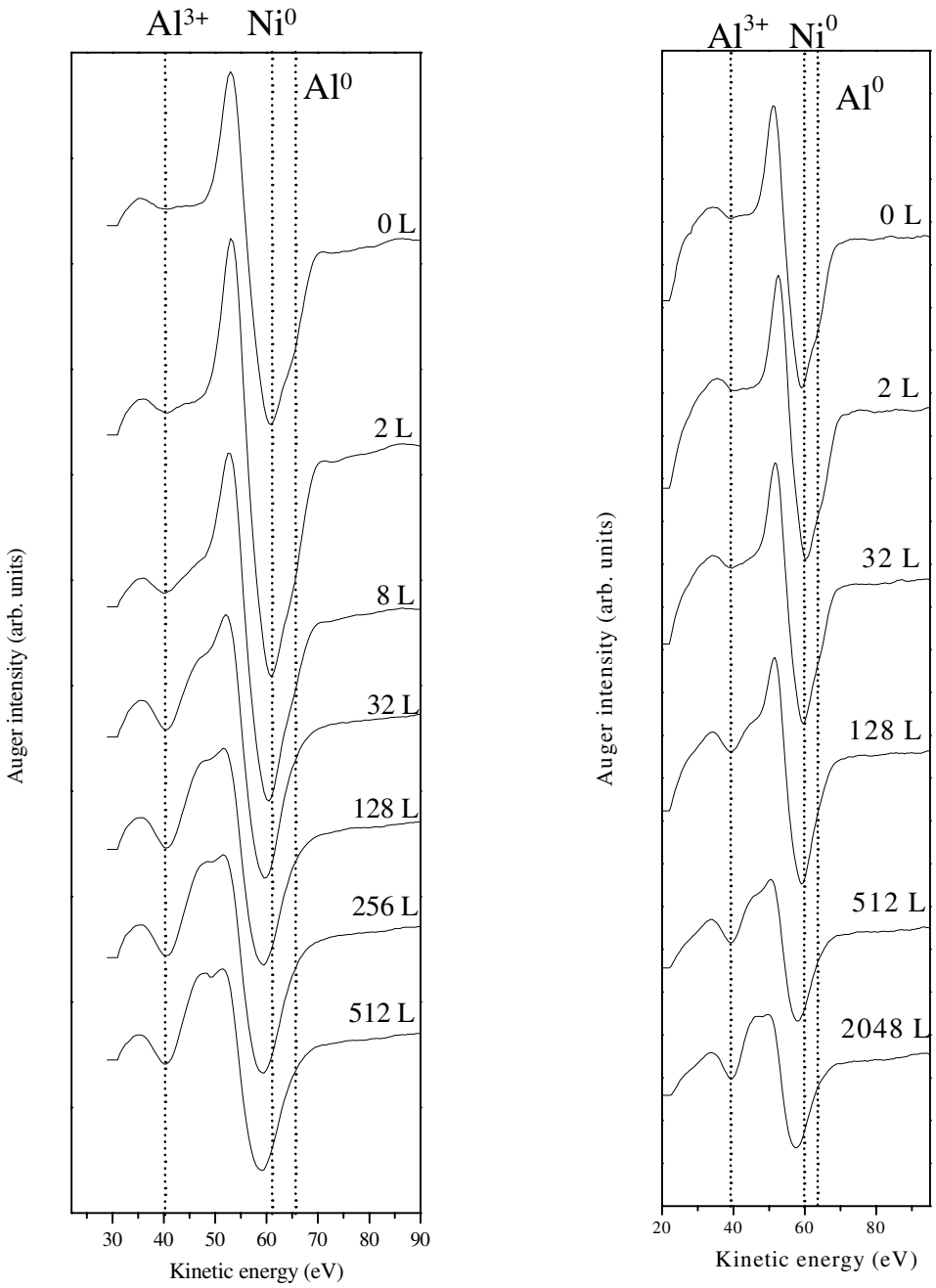

Fig. 6.2. Evolution of the Auger lineshapes for the oxidation of the (a) clean, and (b) sulfur-covered $Ni_3Al(111)$ surfaces.

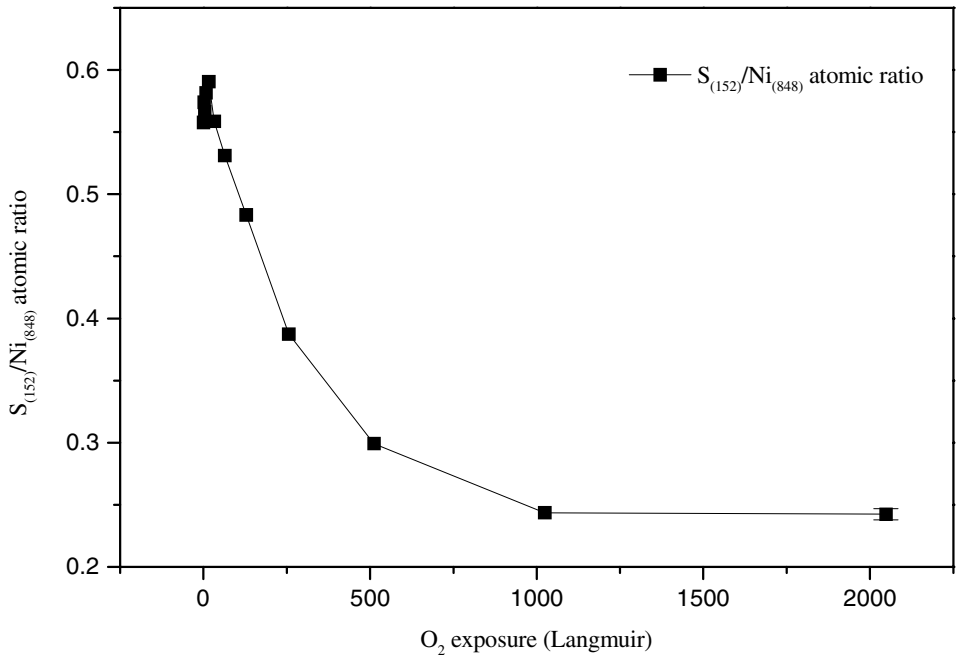

Fig. 6.3. Changes in the $S_{(152)}/Ni_{(848)}$ atomic ratio with increasing oxygen exposure.

The oxides formed by saturation exposure of the clean and sulfur-covered $Ni_3Al(111)$ surfaces to O_2 at 300 K did not exhibit any LEED pattern, demonstrating the lack of long-range order. This is indicative of the formation of a disordered oxide film. Low-resolution STM images (200 nm × 200 nm, Fig. 6.4) were recorded after the sulfur-free and (2×2)-S modified $Ni_3Al(111)$ surfaces were exposed, respectively, to ~ 256 L and ~ 2048 L O_2 at 300 K. These images and their corresponding line profiles (Fig. 6.4) clearly reveal the difference in the morphologies of the oxides formed on the sulfur-free and sulfur-covered $Ni_3Al(111)$ surfaces. The STM image for the oxide formed on the sulfur-free $Ni_3Al(111)$ surface (Fig. 6.4a) shows the absence of large three-dimensional oxide islands, in contrast to the STM image for the oxide formed on the sulfur-covered surface (Fig. 6.4b), which reveals three-dimensional structures that are approximately 10-20 Å

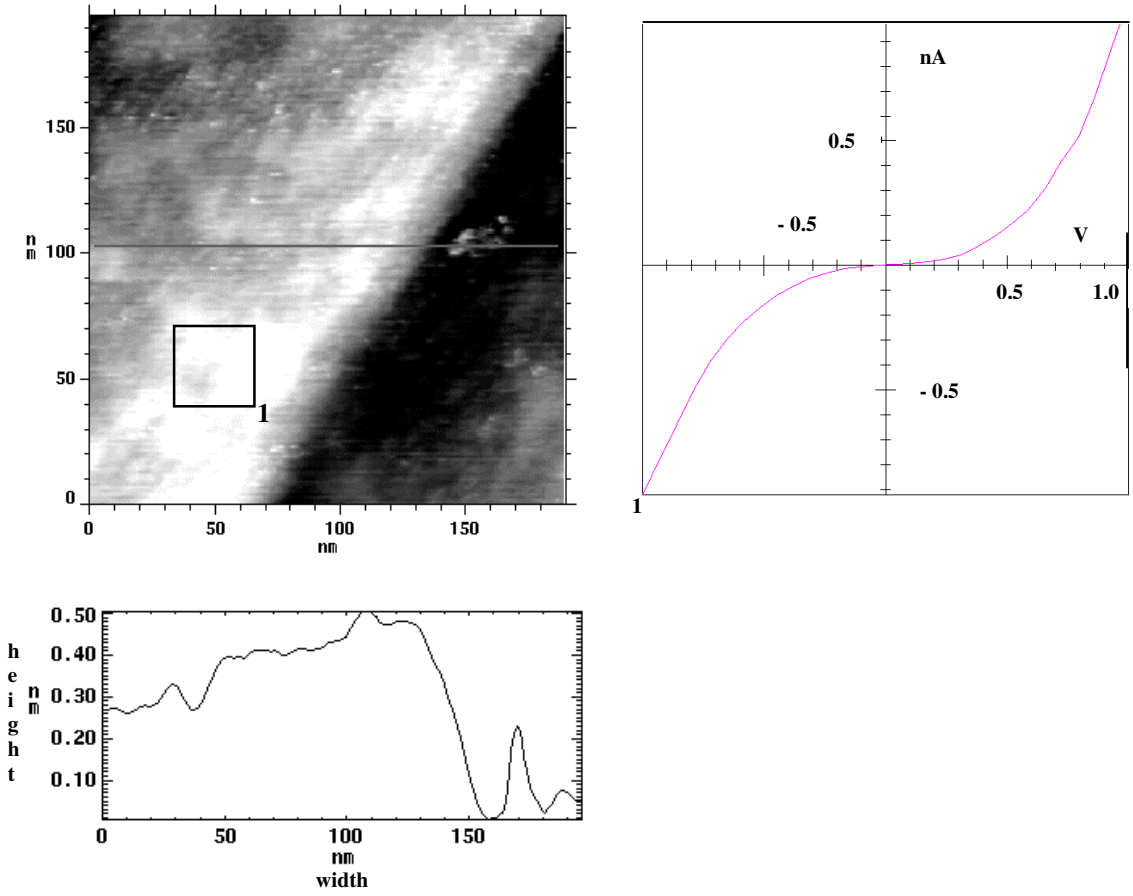

Fig. 6.4 (a). STM image (200 nm × 200 nm), line profile, and I/V curve after exposure of the sulfur-free $Ni_3Al(111)$ surface to saturation coverage (256 L) of O_2 at room temperature (U_{gap} = + 1.0 V, I = 1 nA).

high and 10-80 Å wide. This result is consistent with the findings of earlier studies of the oxidation of clean and sulfur-covered Fe(111) (7) and Fe(110) (25) surfaces. A wide distribution of oxide island sizes was observed in case of the sulfur-covered surfaces, while in case of the sulfur-free surfaces, the oxides showed lesser variation in the island dimensions (7,25). Figure 6.4 also shows the absence and the presence of steps for the topographical images of the oxides formed on the sulfur-covered and sulfur-free $Ni_3Al(111)$ surface, respectively. I/V spectroscopy curves (Fig. 6.4) reveal insulating

behavior characteristic of oxide formation. It should be noted that these band gaps are much narrower than the band gaps of bulk Al_2O_3 (~ 8.7 eV) (26) and bulk NiO (~ 4.3 eV) (27). This has been explained by density functional theory calculations (28), which indicate that although the intrinsic gap of the ultrathin oxide is still equal to that of the bulk oxide, the measured gap is much lower due to the overlap with substrate wavefunctions.

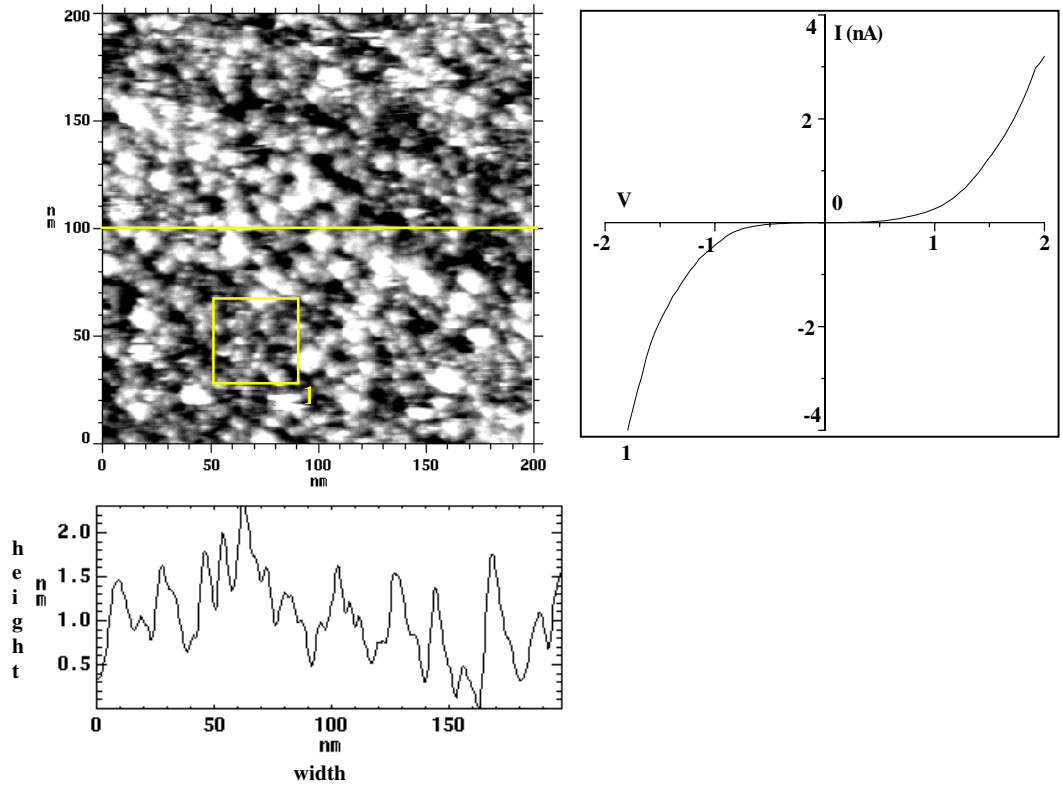

Fig. 6.4 (b). STM image (200 nm × 200 nm), line profile, and I/V curve after exposure of the (2×2)-S covered $Ni_3Al(111)$ surface to saturation coverage (2048 L) of O_2 at room temperature (U_{gap} = + 1.5 V, I = 1 nA).

6.3.2. Effect of temperature on oxide stability

In order to study the effects of sulfur on oxide thermal stability, the disordered oxide/S/$Ni_3Al(111)$ (Fig. 6.4b) was annealed step-wise to ~ 1100 K (15 minutes at each temperature). The changes in the $O_{(510)}/Ni_{(848)}$ and $S_{(152)}/Ni_{(848)}$ atomic ratios during annealing are displayed in Fig. 6.5a. The $O_{(510)}/Ni_{(848)}$ atomic ratio (Fig. 6.5a) increases from 300 K to 1000 K. A similar increase in the $O_{(510)}/Ni_{(848)}$ atomic ratio was observed in the same temperature range for the annealing of an oxide prepared on a sulfur-free $Ni_3Al(111)$ surface (Chapter 4), and attributed to the spreading of the oxide across the surface (Chapter 4). The $S_{(152)}/Ni_{(848)}$ atomic ratio slightly increases up to ~ 500 K, then

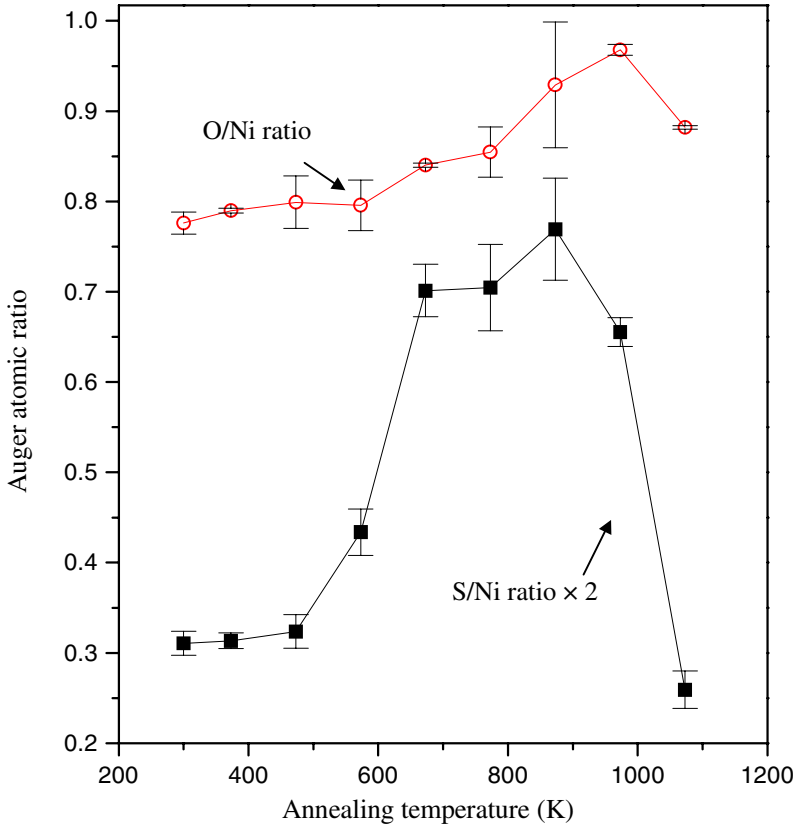

Fig. 6.5. (a) Effect of step-wise annealing of the oxide [shown in Fig. 6.4(b)] from 300 K to 1100 K, for 15 minutes at each temperature: variations in the $O_{(510)}/Ni_{(848)}$ and $S_{(152)}/Ni_{(848)}$ atomic ratios with temperature.

increases steeply up to 700 K. It reaches its maximum value in the temperature range of 700-900 K, then sharply declines after ~ 900 K (Fig. 6.5a). A plot of $Al_{(1396)}/Ni_{(848)}$ atomic ratio vs. temperature (Fig. 6.5b) shows an increase in the ratio at T ≥ 600 K. In addition, the Auger spectra (Fig. 6.5c) reveal the appearance of a shoulder characteristic of metallic aluminum at 68 eV (19,20). The $Al_{(1396)}/Ni_{(848)}$ atomic ratio after annealing to ~ 1100 K (Fig. 6.5b) corresponds to an aluminum surface concentration of ~ 40% (topmost layer).

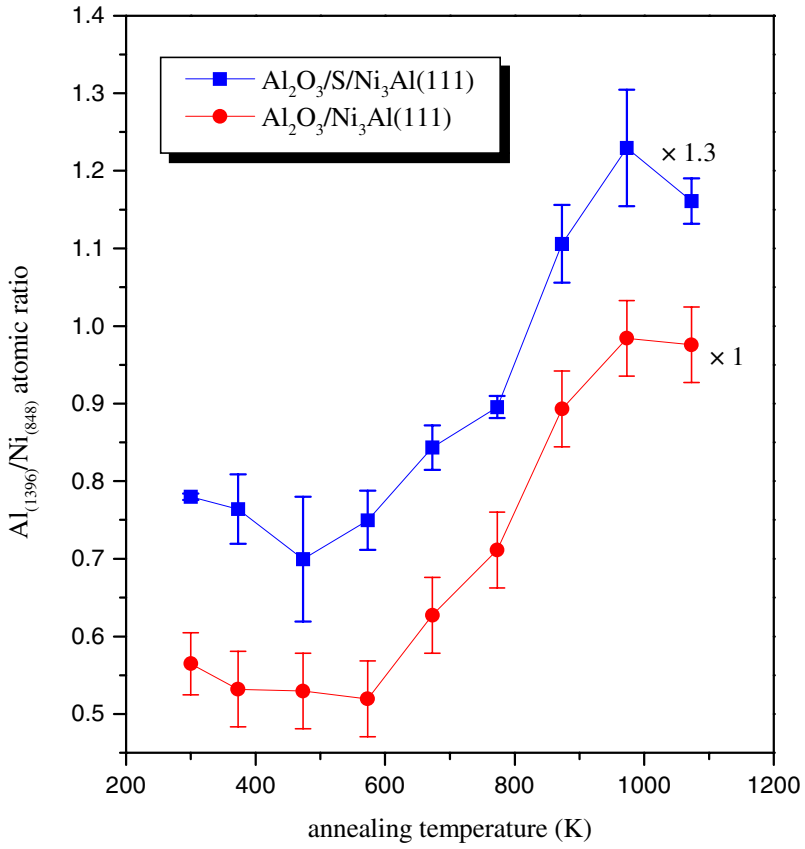

Fig. 6.5 (b). Effect of step-wise annealing of the oxide [shown in Fig. 6.4(b)] from 300 K to 1100 K, for 15 minutes at each temperature: $Al_{(1396)}/Ni_{(848)}$ atomic ratio vs. temperature reveals aluminum segregation. The results for the annealing of the oxide formed on the sulfur-free surface [shown in Fig. 6.4(a)] are also shown for comparison.

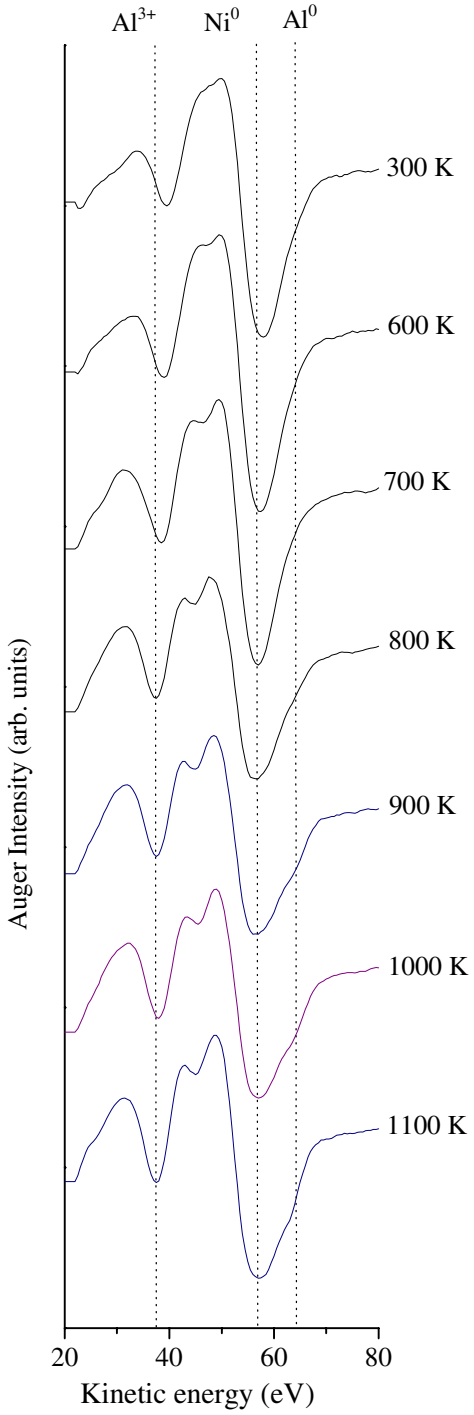

Fig. 6.5 (c). Effect of step-wise annealing of the oxide [shown in Fig. 6.4(b)] from 300 K to 1100 K, for 15 minutes at each temperature: Auger low-energy lineshape reveals a metallic aluminum shoulder at 68 eV at T > 800 K.

Given that the equilibrium concentration of aluminum atoms in a clean, well-ordered $Ni_3Al(111)(2\times2)$ surface is ~ 25% (29), this represents a ~ 60% increment in the aluminum surface concentration due to annealing. This observation has also been reported (Chapter 4) for the oxidation and post-annealing of a sulfur-free $Ni_3Al(111)$ surface (shown in Fig. 6.5b for comparison). The increase in the $Al_{(1396)}/Ni_{(848)}$ atomic ratio at $T \geq 600$ K was attributed to the formation of an aluminum-enriched layer at the γ'-Al_2O_3-$Ni_3Al(111)$ interface (Chapter 4), as a result of segregation of aluminum from the bulk to the interface. From the attenuation in the intensity of the $Ni_{(848)}$ peak [λ = 18.55 Å (18)], the thickness of the γ'-$Al_2O_3/S/Ni_3Al(111)$* is estimated to be 6.06 ± 1.7 Å. The results described [Figs. 6.5, and 6.6 (*vide infra*)] were also obtained when the sulfur coverage (θ_S) prior to oxidation was increased from 0.17 ML to 0.23 ML (data not shown).

After annealing at 1000-1100 K for 15 minutes, a complex LEED pattern with considerable multiple scattering, similar to those reported for $TiO_2/Pt(111)$ (30), $Al_2O_3/Re(0001)$ (31,32) and $Al_2O_3/Ru(0001)$ (31) was observed for the ordered γ'-$Al_2O_3/S/Ni_3Al(111)$ (Fig. 6.6a). The LEED pattern in Fig. 6.6a indicates that the γ'-$Al_2O_3/S/Ni_3Al(111)$ film possesses a hexagonal symmetry. This pattern (Fig. 6.6a) is comprised of six sets of diffraction spots. Each set consists of six pairs of satellite spots surrounding the $Ni_3Al(111)(2\times2)$ substrate diffraction spots. The LEED pattern (Fig.

* The notation γ'-$Al_2O_3/S/Ni_3Al(111)$ is merely used for convenience, to distinguish between the ordered oxides formed on the sulfur-covered, and sulfur-free $Ni_3Al(111)$ surfaces. It does not imply that the sulfur remains at the Al_2O_3-$Ni_3Al(111)$ interface after the ordered γ'-oxide is formed; see Section 6.4.2.

6.6a) indicates the existence of two equivalent domains of the oxide that are rotated at angles of 20° and 43° from the $Ni_3Al(111)$ substrate. The unit cells for the two domains of the ordered oxide overlayer are outlined in the schematic in Fig. 6.6b. The dimensions of each unit cell (~ 12.8 Å × 12.8 Å) of the ordered oxide film correspond to a $\left(\frac{5}{2}\times\frac{5}{2}\right)$ with respect to the $Ni_3Al(111)(2\times2)$ substrate. In real space (Fig. 6.6c), this $\left(\frac{5}{2}\times\frac{5}{2}\right)$ lattice consists of four O^{2-}-O^{2-} lattice spacings superimposed onto five interatomic spacings of the $Ni_3Al(111)$ surface. From the nearest-neighbor distance of the $Ni_3Al(111)$ substrate ($a/\sqrt{2}$ = 2.52 Å), an O^{2-}-O^{2-} lattice spacing of 3.2 Å is derived for the ordered oxide film. This O^{2-}-O^{2-} distance is in excellent agreement with the average lattice spacing (3.0 ± 0.1 Å) obtained for the γ-$Al_2O_3/Ni_3Al(111)$ using LEED (13) and STM (Chapter 4) measurements.

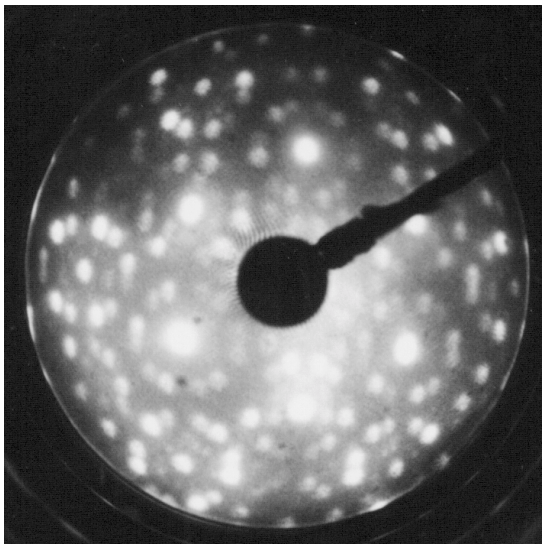

Fig. 6.6 (a). LEED pattern (E = 60 eV) observed after annealing the disordered oxide formed on the S-covered $Ni_3Al(111)$ [Fig. 6.4(b)] to 1100 K.

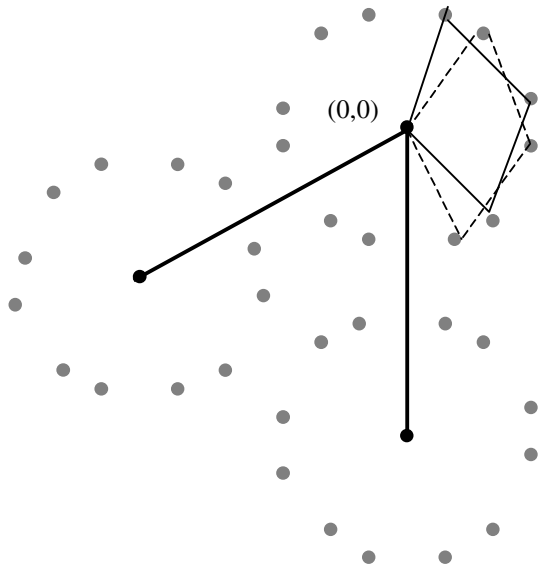

Fig. 6.6 (b). Schematic representation of the LEED pattern showing two rotational domains of the primitive unit-cell of the γ-Al_2O_3/S/Ni_3Al(111).

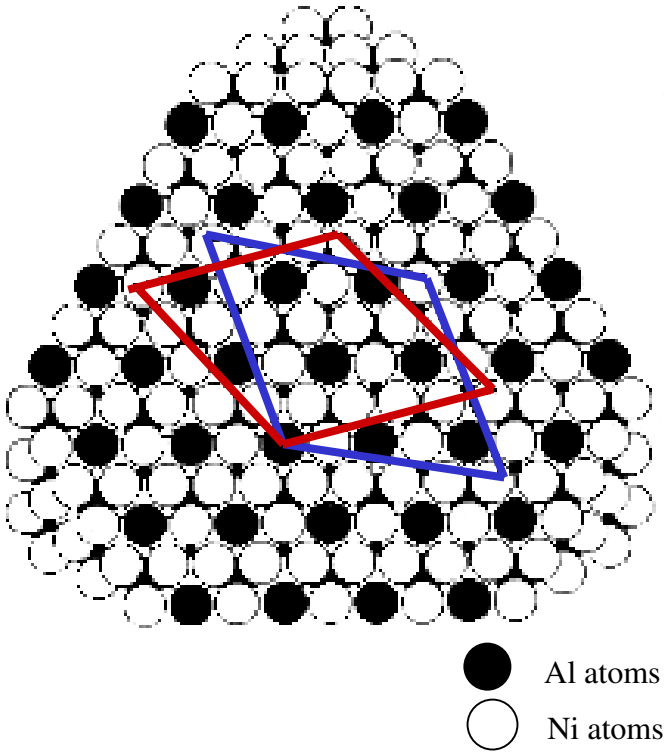

Fig. 6.6 (c). Real space representation of the γ-Al_2O_3 unit-cell superimposed on the Ni_3Al(111) substrate at the interface. The Al(111) interfacial layer, which provides chemisorption sites for the first oxygen layer, is not shown in the diagram.

A typical low-resolution STM image (100 nm ×100 nm) of the ordered γ′-Al_2O_3/S/Ni_3Al(111), and its corresponding line profile are displayed in Fig. 6.7a. The three-dimensional islands observed after oxidation of the (2×2)-S covered Ni_3Al(111) surface at 300 K (Fig. 6.4b) are no longer apparent in the STM images of the ordered γ′-Al_2O_3/S/Ni_3Al(111) (Fig. 6.7a). Well-defined steps with heights of 1-3 nm are clearly differentiated in the topographical image of the ordered oxide (Fig. 6.7a), in contrast to the lack of such resolution in the image of the disordered oxide (Fig. 6.4b). In case of the γ′-Al_2O_3/Ni_3Al(111) (Fig. 6.7b), step heights of 0.4 nm are observed. One striking contrast between the two ordered oxides is that the depressions or pits scattered on step terraces of the γ′-Al_2O_3/S/Ni_3Al(111) (Fig. 6.7a) are considerably larger (4-10 Å deep, 80-400 Å wide) than those in the γ′-Al_2O_3/Ni_3Al(111) (Fig. 6.7b) (0.5 Å deep, 10-20 Å wide) surface. The formation of pits (Fig. 6.7) could be explained by considering the islands (Fig. 6.4) formed by oxidation at 300 K. Although annealing from 300 K to 1100 K may cause the oxide islands to spread out, as evidenced by the increase in the $O_{(510)}/Ni_{(848)}$ atomic ratio (Fig. 6.5a) (Chapter 4), the islands might not spread uniformly across the entire surface. The resulting variations in thickness and uniformity of the oxide could give rise to the multiple scattering effects observed in the ordered LEED pattern of the oxide (Fig. 6.6a). Madey and coworkers (31,32), using LEED and LEIS, have demonstrated that multiple scattering effects are more pronounced in the case of oxide films that grow in clusters, while relatively more uniform oxide films exhibit simpler LEED patterns.

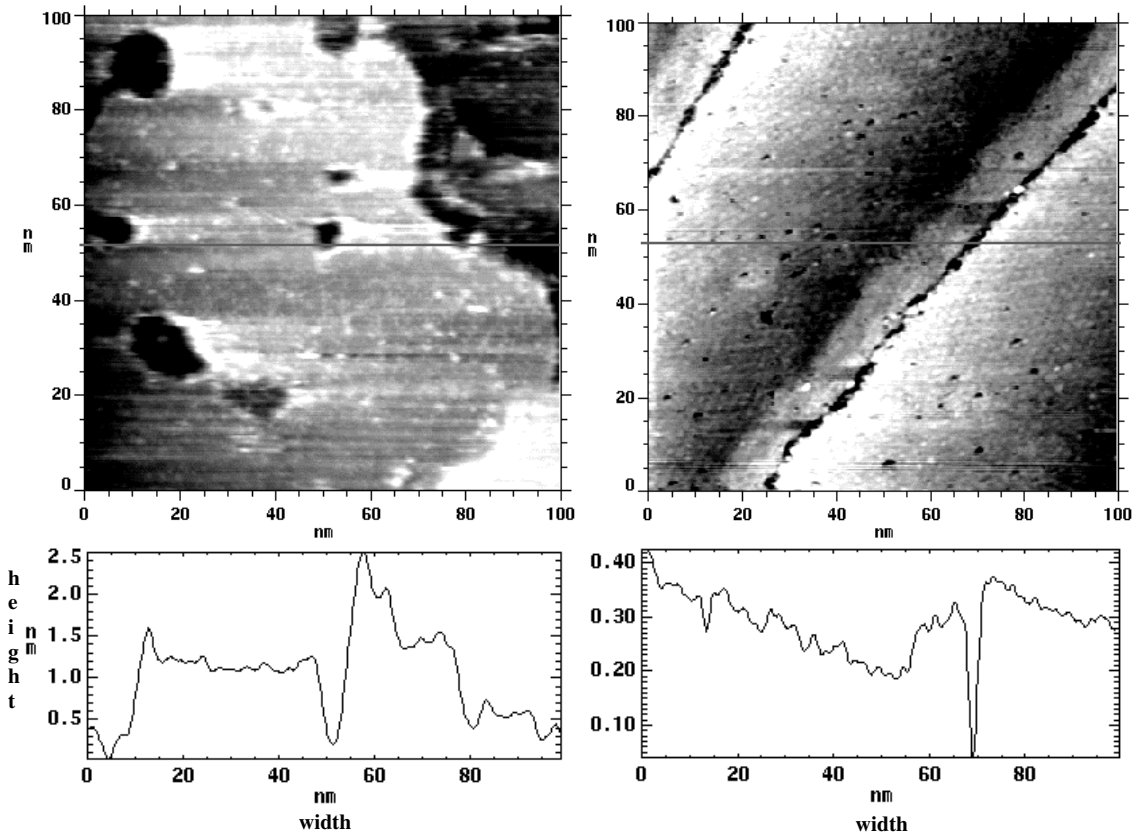

(a) (b)

Fig. 6.7. STM images (100 nm × 100 nm), and corresponding line profiles of the ordered oxide films: (a) γ′-Al_2O_3/S/Ni_3Al(111) (U_{gap} = + 1.0 V, I = 1.5 nA), (b) γ′-Al_2O_3/Ni_3Al(111) (U_{gap} = + 1.0 V, I = 0.1 nA).

6.4. Discussion

6.4.1. Oxidation and oxide morphologies at 300 K

The oxygen uptake curves shown in Fig. 6.1 demonstrate that the presence of sulfur retards the oxidation of the Ni_3Al(111) surface. O_2 exposures as high as ~ 2048 L are required to attain a saturation $O_{(510)}/Ni_{(848)}$ atomic ratio of 0.69 ± 0.1 on the sulfur-covered Ni_3Al(111) surface. In contrast, this ratio is attained at ~ 256 L for the sulfur-

free surface. Similar results have been reported for the oxidation of Fe(111) (7,21), $Ni_{60}Fe_{40}$(100) (22), and Ni(111) (23) surfaces precovered with sulfur.

Earlier studies (13) have demonstrated using HREELS that oxidation of the sulfur-free Ni_3Al(111) surface at room temperature yields a mixture of nickel oxide and amorphous *a*-Al_2O_3. Since sulfur does not alter the chemical composition of the oxide (7), the oxide formed after exposure of the sulfur-covered Ni_3Al(111) surface to ~ 2048 L O_2 is also expected to be a mixture of nickel oxide and amorphous *a*-Al_2O_3, although this distinction cannot be made using AES (Chapter 4). Since the thickness of the oxide (~ 6.5 Å) formed at room temperature (calculated from the attenuation of the $Ni_{(848)}$ signal†), or its composition is not affected by the presence of sulfur on the surface (Fig. 6.1), the results (Figs. 6.1 and 6.2) indicate a lower sticking coefficient for oxygen on the sulfur-covered Ni_3Al(111) substrate, as reported previously for oxidation of sulfur-covered Fe(111) (7,21). We have calculated that at 300 K, the initial sticking coefficient for oxygen on Ni_3Al(111) decreases by an order of magnitude due to preadsorbed sulfur, i.e., from ~ 0.02 on the clean Ni_3Al(111) surface to ~ 0.002 in the presence of sulfur. A similar reduction in the initial sticking coefficient has also been reported for the oxidation of clean and sulfur-covered Fe(111) surfaces (21).

The exponential decrease observed in the $S_{(152)}/Ni_{(848)}$ (Fig. 6.3) and $S_{(152)}/O_{(510)}$ (not shown) atomic ratios with increasing O_2 exposure indicates that the sulfur atoms are overgrown by the oxide during oxidation at ~ 300 K. Since the thickness *d* of the oxide formed at room temperature on the clean and sulfur-covered Ni_3Al(111) surfaces is ~ 6.5

Å, the percent attenuation in the intensity of the sulfur signal can be calculated using Eqs. (6-2) and (6-3), for sulfur atoms located at the oxide-substrate interface:

$$I = I_0 e^{-d/\lambda} \tag{6-3}$$

Substituting the mean free path of sulfur (λ) to be 6.75 Å (18), the attenuation in the intensity of the sulfur signal would be ~ 62%. If the sulfur atoms are distributed within the oxide itself, the percent attenuation in the sulfur signal would be substantially lower than ~ 62%, as calculated previously for oxidation of a sulfur-covered Ni(111) surface (23). The ~ 70% decrease in the sulfur intensity at saturation exposure therefore demonstrates that the sulfur atoms remain at the oxide-$Ni_3Al(111)$ interface during oxide nucleation and growth. Similar results have been reported for the oxidation of various sulfur-covered metal substrates (7,22,23,33).

Apart from the varying oxidation rates, the oxides formed on the sulfur-free and sulfur-covered $Ni_3Al(111)$ surfaces at room temperature exhibit different morphologies in their respective STM images (Fig. 6.4). The oxide formed at 300 K on the sulfur-covered $Ni_3Al(111)$ surface (Fig. 6.4b) reveals the presence of three-dimensional oxide islands with a broad distribution of island sizes, while such large islands are not observed in the STM image of the oxide formed on the $Ni_3Al(111)$ surface (Fig. 6.4a). Previous studies of the oxidation of the clean $Ni_3Al(111)$ surface reported that exposure to O_2 at 300 K results in the formation of small oxidic nuclei (34). Moreover, studies of the oxidation of clean and sulfur-covered Fe(111) (7), and Fe(110) (25) surfaces reported oxide island formation both in the presence and absence of sulfur, although in the presence of sulfur,

---

† Due to the long mean free path of the $Ni_{(848)}$ signal [= 18.55 Å (18)], and also, since the oxide film is ultrathin (< 10 Å), the actual contribution from Ni^{2+} in the intensity of the

the oxide islands were considerably larger, with a broader distribution of island dimensions. The exact cause for the formation of larger three-dimensional oxide islands (Fig. 6.4b) in case of the sulfur-covered $Ni_3Al(111)$ surface is unknown. It is known (23), however, that sulfur atoms block some of the O_2 chemisorption sites at the initial stages of oxidation, reducing the density of oxide nuclei. A lower density of nucleation sites is consistent with the coarser nuclei observed for the sulfur-covered $Ni_3Al(111)$ surface (Fig. 6.4b). Due to the presence of sulfur atoms on the surface, it is likely that the impinging oxygen molecules initially adsorb in sulfur-free regions where they dissociate, and react with the substrate. A combined LEED-AES study of the oxidation of (2×2)-S covered $Ni_{60}Fe_{40}(100)$ (22) observed that at 100°C, the thickness of the oxide at saturation coverage was the same for both clean and sulfur-covered surfaces, and the sulfur signal exhibited an exponential decrease with increasing oxygen exposure. The exponential attenuation of the sulfur signal, and formation of an oxide of the same thickness on both clean and sulfur-covered $Ni_{60}Fe_{40}(100)$ surfaces indicated that the oxide grew over the sulfur atoms in case of the sulfur-covered $Ni_{60}Fe_{40}(100)$ (22) surface, at a slower rate compared to the sulfur-free surface. On the other hand, at 500°C, the intensity of the sulfur signal remained constant throughout the oxidation experiment, demonstrating that oxide nucleation and growth occurred in sulfur-free regions only (22). The behavior observed for the oxygen and sulfur intensities for the room-temperature oxidation of (2×2)-S/$Ni_3Al(111)$ is consistent with the behavior observed by Lad et al. for the oxidation of sulfur-covered $Ni_{60}Fe_{40}(100)$ at 100°C (22). It is therefore possible that the coalesced oxide model proposed by these authors to describe the oxide nucleation and

---

$Ni_{(848)}$ peak is < 7%, and can be assumed to be negligible.

growth at the sulfur-covered $Ni_{60}Fe_{40}(100)$ surface could account for the attenuation of the sulfur signal during the room-temperature oxidation of the sulfur-covered $Ni_3Al(111)$. Based on this model, the oxide grows vertically as the $Ni_3Al(111)$ sample is exposed to oxygen, resulting in the formation of three-dimensional oxide islands (Fig. 6.4b). This is followed by the lateral growth that eventually leads to oxide growth over the sulfur adlayer. It is not possible to discern, however, from the data available, whether sulfur and oxygen were randomly mixed, or segregated into separate domains when the (2×2)-S covered $Ni_3Al(111)$ surface was exposed to submonolayer coverages of O_2. The $S_{(152)}$ Auger peak did not exhibit any distinct lineshape changes (24) indicative of variations in sulfur-substrate bond properties upon oxidation. Therefore, without the aid of detailed I/V calculations using LEED, it is not possible to rule out either mechanism in this case.

6.4.2. Effect of temperature on oxide stability

A progressive anneal of the *a*-Al_2O_3/S/$Ni_3Al(111)$ from 300 K to 1100 K reveals an increase in the $O_{(510)}/Ni_{(848)}$ atomic ratio (Fig. 6.5a). This is contrary to earlier studies of the oxidation of clean and sulfur-covered iron surfaces in UHV (7-9) that reported a substantial reduction in the intensity of the oxygen signal after annealing. This decrease was attributed to the destabilization and dewetting of the oxide formed on the iron substrate (7-9). The increase in the $O_{(510)}/Ni_{(848)}$ atomic ratio (Fig. 6.5a) in case of the sulfur-covered $Ni_3Al(111)$ surface is in contrast to the anticipated result if the oxide were destroyed upon annealing, and therefore demonstrates that the oxide is stable up to at least 1100 K. This increase in atomic ratio is consistent with the spreading of the oxide across the surface upon annealing. The same effect has been reported for a sulfur-free $Ni_3Al(111)$ surface (Chapter 4). In addition to the observed thermal stability, the LEED

pattern of the ordered γ′-Al_2O_3/S/Ni_3Al(111) (Fig. 6.6a) after annealing at 1000-1100 K is virtually identical to that of the γ′-Al_2O_3/Ni_3Al(111) (13,35) (Chapter 4), indicating that sulfur does not affect the ordering of the γ′-Al_2O_3.

The variations in the $S_{(152)}$/$Ni_{(848)}$ atomic ratio (Fig. 6.5a) were also examined in order to determine the position of sulfur during annealing. We have already shown that after oxidation of the (2×2)-S covered Ni_3Al(111) surface at room temperature (300 K), sulfur remains at the oxide-Ni_3Al(111) interface, as evidenced by the exponential decline and the 70% attenuation in the intensity of the $S_{(152)}$ transition (Fig. 6.3). During annealing, however, the $S_{(152)}$/$Ni_{(848)}$ atomic ratio increases gradually from 300-500 K, attains its maximum value at 700-900 K, then sharply declines after 900 K (Fig. 6.5a). It was also observed that increasing the sulfur coverage from 0.17 ML to 0.23 ML produced identical results to those displayed in Figs. 6.5 and 6.6. If sulfur continued to remain at the oxide-Ni_3Al(111) interface during annealing, the $S_{(152)}$/$Ni_{(848)}$ atomic ratio would be expected to decrease, because the spreading of the oxide across the surface[‡] would further attenuate the $S_{(152)}$ signal. Moreover, the formation of an ordered γ′-Al_2O_3 (Fig. 6.6a) would also not be possible, since the interfacial sulfur is known (7,15,36) to obstruct epitaxial oxide growth on the substrate, especially at elevated temperatures. The results (Figs. 6.5 and 6.6) presented in this chapter therefore demonstrate that sulfur does not remain at the Al_2O_3-Ni_3Al(111) interface during annealing. The increase in the $S_{(152)}$/$Ni_{(848)}$ atomic ratio at 500-700 K (Fig. 6.5a) is indicative of the segregation of sulfur

[‡] Although the $Ni_{(848)}$ signal would also be attenuated by the oxide, the inelastic mean free path of the $S_{(152)}$ peak [= 6.75 Å (18)] is considerably lower than that of the $Ni_{(848)}$ transition [= 18.55 Å (18)]. Hence, the $S_{(152)}$/$Ni_{(848)}$ atomic ratio would still decrease due to the spreading of the oxide across the surface.

on top of the oxide, as represented schematically in Fig. 6.8. After 900 K, the $S_{(152)}/Ni_{(848)}$ atomic ratio decreases sharply up to 1100 K (Fig. 6.5a), and decreases further (data not shown), if the sample is reheated from 300-1100 K. There are two possible explanations to account for the removal of sulfur from the oxide surface above 900 K (Fig. 6.5a): [1] desorption, possibly as S_2 (37,38), or [2] diffusion into the bulk of the Ni_3Al alloy. No evidence is currently available to strongly support either possibility in

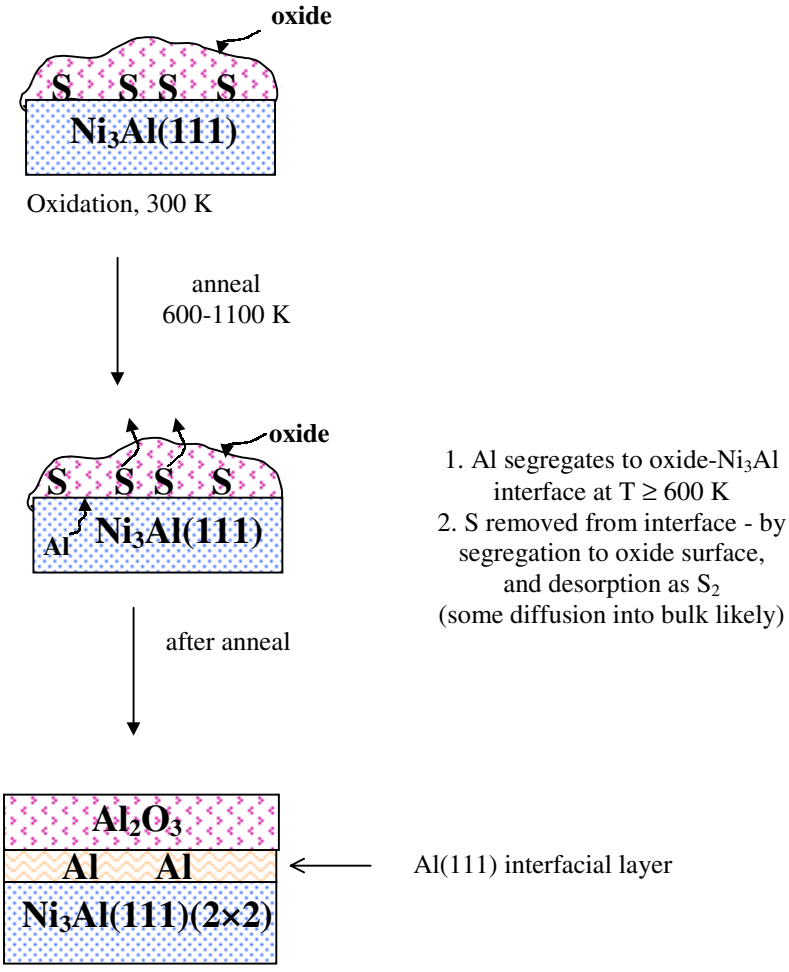

Fig. 6.8. Schematic depicting the segregation of aluminum, and the removal of sulfur from the Al_2O_3-$Ni_3Al(111)$ interface upon annealing from 300 K to 1100 K.

our case. Studies using XPS/TPD (temperature programmed desorption) (37,38), however, have reported that due to poor electron donation, the sticking coefficient of S_2 on Al_2O_3 is very low at 300-700 K, and that sulfur adsorbed on an alumina surface can be desorbed completely as S_2 by annealing to ~ 1200 K. It is very likely, therefore, that after sulfur segregation to the oxide surface at 700-900 K (Fig. 6.5a), further annealing results in the desorption of sulfur as S_2, as reported earlier (37,38).

Another striking observation is that the increase in the $S_{(152)}/Ni_{(848)}$ atomic ratio is coincident with the ~ 60% increase in the surface concentration of aluminum (Figs. 6.5a and 6.5b), and the appearance of the metallic aluminum shoulder at 68 eV (Fig. 6.5c) (19,20) in the Auger spectra. The formation of an Al(111) interfacial layer between the ordered γ'-Al_2O_3 and the $Ni_3Al(111)$ substrate as a result of aluminum segregation upon annealing has been reported in Chapter 4. The aluminum remains at the γ'-Al_2O_3-$Ni_3Al(111)$ interface due to its stabilization by the oxide overlayer (Chapter 4). Whether the segregation of aluminum to the γ'-Al_2O_3-$Ni_3Al(111)$ interface and the removal of sulfur from the interface are correlated cannot be conclusively determined from the present data. Experimental studies (Chapter 2) of the evaporation of aluminum onto a (1×1)-S/Fe(111) surface at 300 K, however, observed a gradual increase in the intensity of the sulfur signal with increasing aluminum deposition time. The results for the deposition of aluminum on the (1×1)-S/Fe(111) surface indicated the preferential insertion of aluminum between the sulfur adlayer and the Fe(111) substrate (Chapter 2), and suggest that the displacement of sulfur by aluminum might have implications for the observed stability of the Al_2O_3/S/$Ni_3Al(111)$ system.

The results for the Al_2O_3/S/Ni_3Al system (Figs. 6.5 and 6.6) demonstrate that the Al_2O_3 formed on an aluminide is stable up to at least 1100 K. These results are in sharp contrast to the findings of UHV studies on Fe-oxide/S/Fe (8,9) and NiO/S/Ni (16,39) systems, which reported that sulfur present at the oxide-substrate interface chemically reacts with metal-oxide bonds producing SO_2, with subsequent oxide spallation (7,15) from the substrate. One might ask if the reason for this anomaly is the high thermodynamic stability of the Al_2O_3 molecule [$\Delta H_f = -1675.7 \pm 1.3$ kJ mol^{-1} (40)] itself. It has been demonstrated, however, that at elevated temperatures ($\geq$ 600 K), interfacial sulfur induces the degradation of ultrathin Al_2O_3 films grown on an Fe(poly) substrate (Chapter 3). Although no SO_2 was detected by TPD measurements, a decrease in the intensity of the $Al^{3+}_{(54)}$ peak, and the formation of Al^0 was observed at T $\geq$ 600 K only when sulfur was present at the Al_2O_3-Fe(poly) interface (Chapter 3). In the absence of sulfur, the Al_2O_3/Fe(poly) interface was stable up to 900 K (Chapter 3). Despite the endothermic nature of the reaction, the ready diffusion of the Al^0 produced into the bulk iron to form an iron-aluminum alloy provides a strong driving force of the reduction of Al_2O_3 to metallic aluminum by interfacial sulfur (Chapter 3). Such diffusion is inhibited in the Al_2O_3/S/Ni_3Al(111) system, due to the presence of bulk aluminum in the Ni_3Al alloy.

6.5. Summary and Conclusions

The oxidation behavior and oxide thermal stability on Ni_3Al(111) in the presence of sulfur have been studied using AES, LEED and STM under ultrahigh vacuum (UHV) conditions. At room temperature, sulfur retards the oxidation and significantly alters the

oxide morphology on the $Ni_3Al(111)$ surface, and remains at the *a*-Al_2O_3-$Ni_3Al(111)$ interface during oxidation. Annealing the *a*-Al_2O_3/S/$Ni_3Al(111)$ from 300 K to 1100 K results in the segregation of aluminum to the γ'-Al_2O_3-$Ni_3Al(111)$ interface. The Al_2O_3 formed on the $Ni_3Al(111)$ substrate is stable up to ~ 1100 K. The results demonstrate that the stability of the Al_2O_3 on the $Ni_3Al(111)$ substrate is connected with the segregation of aluminum, and the removal of sulfur from the oxide-aluminide interface upon annealing.

6.6. Chapter References

(1) Meier, G. H. *Mater. Corros.* **1996**, *47*, 595.

(2) Hou, P. Y.; Wang, Z.; Prüßner, K.; Alexander, K. B.; Brown, I. G. in *3rd International Conference on Microscopy of Oxidation*; Hou, P. Y., Wang, Z., Prüßner, K., Alexander, K. B. and Brown, I. G., Eds.; The Institute of Materials, London: Trinity Hall, Cambridge, UK, 1996, p 1.

(3) Smialek, J. L.; Jayne, D. T.; Schaeffer, J. C.; Murphy, W. H. *Thin Solid Films* **1994**, *253*, 285.

(4) Kiely, J. D.; Yeh, T.; Bonnell, D. A. *Surf. Sci.* **1997**, *393*, L126.

(5) Smialek, J. L. *Metall. Trans. A* **1991**, *22*, 739.

(6) Hou, P. Y.; Stringer, J. *Oxid. Met.* **1992**, *38*, 323.

(7) Lin, J.-S.; Ekstrom, B.; Addepalli, S. G.; Cabibil, H.; Kelber, J. A. *Langmuir* **1998**, *14*, 4843.

(8) Cabibil, H.; Kelber, J. A. *Surf. Sci.* **1995**, *329*, 101.

(9) Cabibil, H.; Kelber, J. A. *Surf. Sci.* **1997**, *373*, 257.

(10) Stott, F. H. *Rep. Prog. Phys.* **1987**, *50*, 861.

(11) Grabke, H. J.; Wiemer, D.; Viefhaus, H. *Appl. Surf. Sci.* **1991**, *47*, 243.

(12) Panzner, G.; Egert, B. *Surf. Sci.* **1984**, *144*, 651.

(13) Becker, C.; Kandler, J.; Raaf, H.; Linke, R.; Pelster, T.; Dräger, M.; Tanemura, M.; Wandelt, K. *J. Vac. Sci. Technol. A* **1998**, *16*, 1000.

(14) Jaeger, R. M.; Kuhlenbeck, H.; Freund, H.-J.; Wuttig, M.; Hoffmann, W.; Franchy, R.; Ibach, H. *Surf. Sci.* **1991**, *259*, 235.

(15) Kelber, J. A.; Addepalli, S. G.; Lin, J.-S.; Cabibil, H. in *High Temperature Corrosion and Materials Chemistry*; Hou, P. Y., McNallan, M. J., Oltra, R., Opila, E. J. and Shores, D. A., Eds.; The Electrochemical Society, Inc.: San Diego, CA, 1998; Vol. 98-99, p 190.

(16) Windawi, H.; Katzer, J. R. *J. Vac. Sci. Technol.* **1979**, *16*, 497.

(17) Lin, J.-S.; Cabibil, H.; Ekstrom, B.; Kelber, J. A. *Surf. Sci.* **1997**, *371*, 337.

(18) Powell, C. J.; Jablonski, A.; Tilinin, I. S.; Tanuma, S.; Penn, D. R. *J. Electron Spectrosc. Relat. Phenom.* **1999**, *98-99*, 1.

(19) Chen, J. G.; Crowell, J. E.; Yates, J. T., Jr. *Phys. Rev. B* **1986**, *33*, 1436.

(20) Homeny, J.; Buckley, M. M. *Materials Lett.* **1990**, *9*, 443.

(21) Arabczyk, W.; Narkiewicz, U.; Kalucki, K.; Friedenberg, E. *Appl. Surf. Sci.* **1993**, *72*, 45.

(22) Lad, R. J.; Schrott, A. G.; Blakely, J. M. *J. Vac. Sci. Technol. A* **1985**, *3*, 1282.

(23) Liu, J.; Lu, J. P.; Chu, P. W.; Blakely, J. M. *J. Vac. Sci. Technol.* **1992**, *10*, 2355.

(24) Arabczyk, W.; Baumann, T.; Müssig, H. J.; Storbeck, F.; Meisel, A. *Vacuum* **1990**, *41*, 79.

(25) Jennings, W. D.; Chottiner, G. S.; Michal, G. M. *Surf. Interface Anal.* **1988**, *11*, 377.

(26) Henrich, V. E.; Cox, P. A. *The Surface Science of Metal Oxides*; Cambridge University Press:, 1996.

(27) Sawatzky, G. A.; Allen, J. W. *Phys. Rev. Lett.* **1984**, *53*, 2339.

(28) Verdozzi, C.; Jennison, D. R.; Sears, M. P. *Phys. Rev. Lett.* **1999**, *82*, 799.

(29) Sondericker, D.; Jona, F.; Marcus, P. M. *Phys. Rev. B* **1986**, *34*, 6770.

(30) Boffa, A. B.; Galloway, H. C.; Jacobs, P. W.; Benítez, J. J.; Batteas, J. D.; Salmeron, M.; Bell, A. T.; Somorjai, G. A. *Surf. Sci.* **1995**, *326*, 80.

(31) Wu, Y.; Garfunkel, E.; Madey, T. E. *J. Vac. Sci. Technol. A* **1996**, *14*, 2554.

(32) Wu, Y.; Garfunkel, E.; Madey, T. E. *Surf. Sci.* **1996**, *365*, 337.

(33) Partridge, A.; Tatlock, G. J.; Leibsle, F. M. *Surf. Sci.* **1997**, *381*, 92.

(34) Rosenhahn, A.; Schneider, J.; Kandler, J.; Becker, C.; Wandelt, K. *Surf. Sci.* **1999**, *433-435*, 705.

(35) Bardi, U.; Atrei, A.; Rovida, G. *Surf. Sci.* **1992**, *268*, 87.

(36) Liu, J.; Blakely, J. M. *Appl. Surf. Sci.* **1994**, *74*, 43.

(37) Rodriguez, J. A.; Kuhn, M.; Hrbek, J. *Surf. Sci.* **1997**, *380*, 397.

(38) Rodriguez, J. A.; Kuhn, K. *J. Phys. Chem. B* **1997**, *101*, 3187.

(39) Holloway, P. H.; Hudson, J. B. *Surf. Sci.* **1972**, *33*, 56.

(40) Lide, D. R. *CRC Handbook of Chemistry and Physics*; 74 ed.; CRC Press: Boca Raton, 1994, p 9/123.

REFERENCES

Arabczyk, W.; Müssig, H.-J.; Storbeck, F. *Phys. Status Solidi A* **1979**, *55*, 437.

Arabczyk, W.; Baumann, T.; Müssig, H. J.; Storbeck, F.; Meisel, A. *Vacuum* **1990**, *41*, 79.

Arabczyk, W.; Narkiewicz, U.; Kalucki, K.; Friedenberg, E. *Appl. Surf. Sci.* **1993**, *72*, 45.

Argile, C.; Rhead, G. E. *Surf. Sci. Rep.* **1989**, 272.

Bardi, U.; Atrei, A.; Rovida, G. *Surf. Sci. Lett.* **1990**, *239*, L511.

Bardi, U.; Atrei, A.; Rovida, G. *Surf. Sci.* **1992**, *268*, 87.

Baxter, D. J.; Natesan, K. *Oxid. Met.* **1989**, *31*, 305.

Becker, C.; Kandler, J.; Raaf, H.; Linke, R.; Pelster, T.; Dräger, M.; Tanemura, M.; Wandelt, K. *J. Vac. Sci. Technol. A* **1998**, *16*, 1000.

Bertrams, T.; Brodde, A.; Hannemann, H.; C. A. Ventrice, J.; Wilhelmi, G.; Neddermeyer, H. *Appl. Surf. Sci.* **1994**, *75*, 125.

Bertrams, T.; Brodde, A.; Neddermeyer, H. *J. Vac. Sci. Technol. B* **1994**, *12*, 2122.

Besenbacher, F. *Rep. Prog. Phys.* **1996**, *59*, 1737.

Birks, N.; Meier, G. H. *Introduction to High Temperature Oxidation of Metals*; 1 ed.; Edward Arnold Publishers Ltd.: London, 1983.

Blum, R.-P.; Niehus, H. *Applied Physics A* **1998**, *66*, S529.

Blum, R.-P.; Ahlbehrendt, D.; Niehus, H. *Surf. Sci.* **1998**, *396*, 176.

Boffa, A. B.; Galloway, H. C.; Jacobs, P. W.; Benítez, J. J.; Batteas, J. D.; Salmeron, M.; Bell, A. T.; Somorjai, G. A. *Surf. Sci.* **1995**, *326*, 80.

Cabibil, H.; Kelber, J. A. *Surf. Sci.* **1995**, *329*, 101.

Cabibil, H.; Lin, J.-S.; Kelber, J. A. *Surf. Sci.* **1997**, *382*, L645.

Cabibil, H.; Kelber, J. A. *Surf. Sci.* **1997**, *373*, 257.

Cabibil, H.; Lin, J.-S.; Kelber, J. A. *J. Vac. Sci. Technol. B* **1998**, *16*, 30.

Chen, J. G.; Crowell, J. E.; Yates, J. T., Jr. *Phys. Rev. B* **1986**, *33*, 1436.

Chen, P. J.; Goodman, D. W. *Surf. Sci.* **1994**, *312*, L767.

Colaianni, M. L.; Chen, P. J.; Yates, J. T., Jr. *Surf. Sci.* **1990**, *238*, 13.

Colaianni, M. L.; Chorkendorff, I. *Phys. Rev. B* **1994**, *50*, 8798.

Cotterill, G. F.; Niehus, H.; O'Connor, D. J. *Surf. Rev. Lett.* **1996**, *3*, 1355.

Davis, L. E.; MacDonald, N. C.; Palmberg, P. W.; Raich, G. E.; Weber, R. E. *Handbook of Auger Electron Spectroscopy*; 2 ed.; Physical Electronics Industries, Inc.: Eden Prairie, 1979.

Dunphy, J. C.; Sautet, P.; Ogletree, D. F.; Salmeron, M. B. *J. Vac. Sci. Technol. A* **1993**, *11*, 1975.

Edmonds, T.; McCarroll, J. J.; Pitkethly, R. C. *J. Vac. Sci. Technol.* **1971**, *8*, 68.

Ertl, G.; Küppers, J. *Low Energy Electrons and Surface Chemistry*; Verlag Chemie: Weinheim, 1974; Vol. 4.

Ertl, G.; Wandelt, K. *Surf. Sci.* **1975**, *50*, 479.

Feldman, L. C.; Mayer, J. W. *Fundamentals of Surface and Thin Film Analysis*; P T R Prentice Hall: Englewood Cliffs, 1986.

Fontana, M. G. *Corrosion Engineering*; 3 ed.; McGraw-Hill, Inc.: New York, 1986.

Fox, P.; Lees, D. G.; Lorimer, G. W. *Oxid. Met.* **1991**, *36*, 491.

Franchy, R.; Wuttig, M.; Ibach, H. *Surf. Sci.* **1987**, *189/190*, 438.

Franchy, R.; Masuch, J.; Gassmann, P. *Appl. Surf. Sci.* **1996**, *93*, 317.

Franchy, R.; So, S. K.; Gaßmann, P. *Surf. Rev. Lett.* **1996**, *3*, 1909.

Fujita, K.; Watanabe, H.; Ichikawa, M. *J. Appl. Phys.* **1998**, *83*, 3638.

Funkenbusch, A. W.; Smeggil, J. G.; Bornstein, N. S. *Metall. Trans. A* **1985**, *16A*, 1164.

Gassmann, P.; Franchy, R.; Ibach, H. *Surf. Sci.* **1994**, *319*, 95.

Grabke, H. J.; Wiemer, D.; Viefhaus, H. *Fresenius J. Anal. Chem.* **1991**, *341*, 402.

Grabke, H. J.; Wiemer, D.; Viefhaus, H. *Appl. Surf. Sci.* **1991**, *47*, 243.

Hardegree, E. L.; Ho, P.; White, J. M. *Surf. Sci.* **1986**, *165*, 488.

Henrich, V. E.; Cox, P. A. *The Surface Science of Metal Oxides*; Cambridge University Press:, 1996.

Holloway, P. H.; Hudson, J. B. *Surf. Sci.* **1972**, *33*, 56.

Homeny, J.; Buckley, M. M. *Materials Lett.* **1990**, *9*, 443.

Hong, S. Y.; Anderson, A. B.; Smialek, J. L. *Surf. Sci.* **1990**, *230*, 175.

Hou, P. Y.; Stringer, J. *Oxid. Met.* **1992**, *38*, 323.

Hou, P. Y.; Stringer, J. *J. Phys. IV* **1993**, *3*, 231.

Hou, P. Y.; Wang, Z.; Prüßner, K.; Alexander, K. B.; Brown, I. G. in *3rd International Conference on Microscopy of Oxidation*; Hou, P. Y.; Wang, Z.; Prüßner, K.; Alexander, K. B.; Brown, I. G., Eds.; The Institute of Materials: Trinity Hall, Cambridge, UK, 1996, p 1.

Isern, H.; Castro, G. R. *Surf. Sci.* **1989**, *211/212*, 865.

Jacobi, K.; Muschwitz, C. V.; Kambe, K. *Surf. Sci.* **1980**, *93*, 310.

Jaeger, R. M.; Kuhlenbeck, H.; Freund, H.-J.; Wuttig, M.; Hoffmann, W.; Franchy, R.; Ibach, H. *Surf. Sci.* **1991**, *259*, 235.

Jennings, W. D.; Chottiner, G. S.; Michal, G. M. *Surf. Interface Anal.* **1988**, *11*, 377.

Jennison, D. R.; Verdozzi, C.; Schultz, P. A.; Sears, M. P. *Phys. Rev. B* **1999**, *59*, R15605.

Jones, D. A. *Principles and Prevention of Corrosion*; Macmillan Publishing Company: New York, 1991.

Kelber, J. A.; Addepalli, S. G.; Lin, J.-S.; Cabibil, H. in *High Temperature Corrosion and Materials Chemistry*; Hou, P. Y., McNallan, M. J., Oltra, R., Opila, E. J.

and Shores, D. A., Eds.; The Electrochemical Society, Inc.: San Diego, CA, 1998; Vol. 98-99, p 190.

Kiely, J. D.; Yeh, T.; Bonnell, D. A. *Surf. Sci.* **1997**, *393*, L126.

Kitajima, Y.; Yagi, S.; Yokoyama, T.; Imanishi, A.; Takenaka, S.; Ohta, T. *Surf. Sci.* **1994**, *320*, L89.

Klimenkov, M.; Nepijko, S.; Kuhlenbeck, H.; Freund, H.-J. *Surf. Sci.* **1997**, *385*, 66.

Lad, R. J.; Schrott, A. G.; Blakely, J. M. *J. Vac. Sci. Technol. A* **1985**, *3*, 1282.

Lees, D. G. *Oxid. Met.* **1987**, *27*, 75.

Libuda, J.; Winkelmann, F.; Baeumer, M.; Freund, H.-J.; Bertrams, T.; Neddermeyer, H.; Mueller, K. *Surf. Sci.* **1994**, *318*, 61.

Lide, D. R. *CRC Handbook of Chemistry and Physics*; 74 ed.; CRC Press: Boca Raton, 1994, p 4/36.

Lide, D. R. *CRC Handbook of Chemistry and Physics*; 74 ed.; CRC Press: Boca Raton, 1994, p 9/123.

Lieber, C. M. in *Chemical and Engineering News*; 1994, p 28.

Lin, J.-S.; Cabibil, H.; Ekstrom, B.; Kelber, J. A. *Surf. Sci.* **1997**, *371*, 337.

Lin, J.-S.; Ekstrom, B.; Addepalli, S. G.; Cabibil, H.; Kelber, J. A. *Langmuir* **1998**, *14*, 4843.

Lin, J.-S.; Cabibil, H.; Kelber, J. A. *Surf. Sci.* **1998**, *395*, 30.

Liu, J.; Lu, J. P.; Chu, P. W.; Blakely, J. M. *J. Vac. Sci. Technol.* **1992**, *10*, 2355.

Liu, J.; Blakely, J. M. *Appl. Surf. Sci.* **1994**, *74*, 43.

Lobnig, R. E.; Grabke, H. J. *Corros. Sci.* **1990**, *30*, 1045.

MacLaren, J. M.; Pendry, J. B.; Rous, P. J.; Saldin, D. K.; Somorjai, G. A.; Van Hove, M. A.; Vvedensky, D. D. *Surface Crystallographic Information Service: A Handbook of Surface Structures*; D. Reidel Publishing Company: Dordrecht, 1987.

Meier, G. H.; Pettit, F. S. *Mater. Sci. Technol.* **1992**, *8*, 331.

Meier, G. H. *Mater. Corros.* **1996**, *47*, 595.

Michael, R.; Gastaldi, J.; Allasia, C.; Jourdan, C.; Derren, J. *Surf. Sci.* **1980**, *95*, 309.

Microcal Software, Inc.: Northampton, MA 01060

Mo, S.-D.; Xu, Y.-N.; Ching, W.-Y. *J. Am. Ceram. Soc.* **1997**, *89*, 1193.

Mrowec, S. *Oxid. Met.* **1995**, *44*, 177.

Mullins, D. R.; Huntley, D. R.; Overbury, S. H. *Surf. Sci. Lett.* **1995**, *323*, L287.

Nien, C.-H.; Abdelrehim, I. M.; Madey, T. E. *Surf. Rev. Lett.* **1999**, *6*, 77.

Nix, R. M. *An Introduction to Surface Chemistry*: http://www.chem.qmw.ac.uk/surfaces/scc/sccinfo.htm, 1997.

O'Hanlon, J. F. *A User's Guide to Vacuum Technology*; 2 ed.; John Wiley & Sons: New York, 1989.

Ohtani, H.; Kao, C.-T.; Hove, M. A. V.; Somorjai, G. A. *Prog. Surf. Sci.* **1986**, *23*, 155.

Oudar, J. *Mater. Sci. Eng.* **1980**, *42*, 101.

Panzner, G.; Egert, B. *Surf. Sci.* **1984**, *144*, 651.

Parker, T. M.; Condon, N. G.; Lindsay, R.; Thornton, G.; Leibsle, F. M. *Surf. Rev. Lett.* **1994**, *1*, 705.

Partridge, A.; Tatlock, G. J.; Leibsle, F. M.; Flipse, C. F. J.; Hörmandinger, G.; Pendry, J. B. *Phys. Rev. B* **1993**, *48*, 8267.

Partridge, A.; Tatlock, G. J.; Leibsle, F. M. *Surf. Sci.* **1997**, *381*, 92.

Pauling, L. *The Nature of the Chemical Bond*; 3 ed.; Cornell University Press: Ithaca, New York, 1960.

Perdereau, M.; Oudar, J. *Surf. Sci.* **1970**, *20*, 80.

Powell, C. J.; Jablonski, A.; Tilinin, I. S.; Tanuma, S.; Penn, D. R. *J. Electron Spectrosc. Relat. Phenom.* **1999**, *98-99*, 1.

RBD Enterprises: Bend, OR 97702.

Riviere, J. C. in *Practical Surface Analysis: Auger and X-ray Photoelectron Spectroscopy*; 2 ed.; Briggs, D. and Seah, M. P., Eds.; Wiley: New York, 1979; Vol. 1, p 19.

Roberts, R. H.; Ramsey, J. A. *J. Electron Spectrosc. Relat. Phenom.* **1990**, *52*, 185.

Rodriguez, J. A.; Kuhn, M.; Hrbek, J. *Surf. Sci.* **1997**, *380*, 397.

Rodriguez, J. A.; Kuhn, K. *J. Phys. Chem. B* **1997**, *101*, 3187.

Rosenhahn, A.; Schneider, J.; Becker, C.; Wandelt, K. *Appl. Surf. Sci.* **1999**, *142*, 169.

Rosenhahn, A.; Schneider, J.; Kandler, J.; Becker, C.; Wandelt, K. *Surf. Sci.* **1999**, *433-435*, 705.

Ruan, L.; Stensgaard, I.; Lægsgaard, E.; Besenbacher, F. *Surf. Sci.* **1993**, *296*, 275.

Sautet, P. *Surf. Sci.* **1997**, *374*, 406.

Sawatzky, G. A.; Allen, J. W. *Phys. Rev. Lett.* **1984**, *53*, 2339.

Schulze, R. K.; Taylor, T. N.; Paffett, M. T. *J. Vac. Sci. Technol.* **1994**, *12*, 3054.

Scully, J. C. *The Fundamentals of Corrosion*; 3 ed.; Pergamon Press: New York, 1990.

Seah, M. P.; Dench, W. A. *Surf. Interface Anal.* **1979**, *1*, 2.

Seah, M. P. in *Practical Surface Analysis: Auger and X-ray Photoelectron Spectroscopy*; 2 ed.; Briggs, D. and Seah, M. P., Eds.; Wiley: New York, 1990; Vol. 1, p 201.

Seah, M. P. in *Practical Surface Analysis: Auger and X-ray Photoelectron Spectroscopy*; 2 ed.; Briggs, D. and Seah, M. P., Eds.; Wiley: New York, 1990; Vol. 1, p 311.

Seo, M.; Lumsden, J. B.; Staehle, R. W. *Surf. Sci.* **1975**, *50*, 541.

Shen, Y.; O'Connor, D. J.; MacDonald, R. J. *Nuclear Instruments and Methods in Physics Research B* **1992**, *67*, 350.

Shores, D. A. *The Electrochemical Society Interface* **1997**, *6*, 42.

Smeggil, J. G.; Funkenbusch, A. W.; Bornstein, N. S. *Metall. Trans. A* **1986**, *17*, 923.

Smentkowski, V. S.; Yates, J. T., Jr. *Surf. Sci.* **1990**, *232*, 113.

Smialek, J. L. *Metall. Trans. A* **1987**, *18*, 164.

Smialek, J. L. *Metall. Trans. A* **1991**, *22*, 739.

Smialek, J. L.; Jayne, D. T.; Schaeffer, J. C.; Murphy, W. H. *Thin Solid Films* **1994**, *253*, 285.

Somorjai, G. A. *Introduction of Surface Chemistry and Catalysis*; John Wiley & Sons, Inc.: New York, 1994.

Somorjai, G. A. *MRS Bull.* **1998**, *23*, 11.

Sondericker, D.; Jona, F.; Moruzzi, V. J.; Marcus, P. M. *Solid State Communications* **1985**, *53*, 175.

Sondericker, D.; Jona, F.; Marcus, P. M. *Phys. Rev. B* **1986**, *34*, 6770.

Stirniman, M. J.; Li, W.; Sibener, S. J. *J. Chem. Phys.* **1995**, *103*, 451.

Stöhr, J.; Johansson, L. I.; Brennan, S.; Hecht, M.; Miller, J. N. *Phys. Rev. B* **1980**, *22*, 4052.

Stott, F. H. *Rep. Prog. Phys.* **1987**, *50*, 861.

Street, S. C.; Xu, C.; Goodman, D. W. *Ann. Rev. Phys. Chem.* **1997**, *48*, 43.

Tersoff, J.; Lang, N. D. in *Scanning Tunneling Microscopy*; Stroscio, J. A. and Kaiser, W. J., Eds.; Academic Press, Inc.: New York, 1993; Vol. 27, p 1.

Tilinin, I. S.; Rose, M. K.; Dunphy, J. C.; Salmeron, M.; Van Hove, M. A. *Surf. Sci.* **1998**, *418*, 511.

Van Hove, M. A. *Heterogeneous Chemistry Reviews* **1995**, *21*, 81.

Venezia, A. M.; Loxton, C. M. *Surf. Sci.* **1988**, *194*, 136.

Venezia, A. M.; Loxton, C. M. *Surf. Interface Anal.* **1988**, *11*, 287.

Verdozzi, C.; Jennison, D. R.; Sears, M. P. *Phys. Rev. Lett.* **1999**, *82*, 799.

Viefhaus, H.; Roux, J. P.; Grabke, H. J. *Fresenius J. Anal. Chem.* **1993**, *346*, 69.

Walker, C. G.; El Gomati, M. M. *Appl. Surf. Sci.* **1988-89**, *35*, 164.

Whittle, D. P.; Stringer, J. *Phil. Trans. Roy. Soc. Lond. A* **1980**, *295*, 309.

Wiederholt, T.; Brune, H.; Wintterlin, J.; Behm, R. J.; Ertl, G. *Surf. Sci.* **1995**, *324*, 91.

Wiesendanger, R. *Scanning Probe Microscopy and Spectroscopy: Methods and Applications*; Cambridge University Press: Cambridge, 1994.

Windawi, H.; Katzer, J. R. *J. Vac. Sci. Technol.* **1979**, *16*, 497.

Wu, Y.; Garfunkel, E.; Madey, T. E. *Surf. Sci.* **1996**, *365*, 337.

Wu, Y.; Garfunkel, E.; Madey, T. E. *J. Vac. Sci. Technol. A* **1996**, *14*, 2554.

Yoon, H. A.; Salmeron, M.; Somorjai, G. A. *Surf. Sci.* **1998**, *395*, 269.